The Dissertation Committee for Alexander Slepko Certifies that this is the approved version of the following dissertation:

Theory of biomineral Hydroxyapatite

Committee:

Alexander A. Demkov, Supervisor

James R. Chelikowsky

Allan H. MacDonald

Dmitrii E. Makarov

Ernst-Ludwig Florin

Theory of biomineral Hydroxyapatite

by

Alexander Slepko, M.A.

Dissertation

Presented to the Faculty of the Graduate School of

The University of Texas at Austin

in Partial Fulfillment

of the Requirements

for the Degree of

Doctor of Philosophy

The University of Texas at Austin

May 2013

Dedication

for everyone

Acknowledgements

First of all, I want to express my sincere thanks to my advisor Prof. Alex Demkov. Through his professional manner he had great influence on my work. His continuous guidance and patience were invaluable.

I would also like to express my thanks to Sadasivan Shankar for giving me the opportunity to do an internship at Intel during summer 2012.

I am grateful to my group members for discussion and companionship over the years. The numerous people I lived with throughout the last five years, who made my stay in Austin a great life experience.

Most importantly, I am thankful to my family for their moral support and guidance over the last years.

Alexander Slepko

The University of Texas at Austin
May 2013

Theory of biomineral Hydroxyapatite

Alexander Slepko, Ph.D.

The University of Texas at Austin, 2013

Supervisor: Alexander A. Demkov

Hydroxyapatite [HA, $Ca_{10}(PO_4)_6(OH)_2$] is one of the most abundant materials in mammal bone. It crystallizes in an aqueous environment within spaces between tropocollagen protein chains. However, despite its abundance and possible usefulness in the medical field this complex physical system remains poorly understood to date. We present a theoretical study of the energetics of hydroxyapatite, its electronic, mechanical and thermodynamic properties. Our mechanical and thermodynamic properties from first principles are in excellent agreement with the rare available experimental data. The monoclinic and hexagonal phases are lowest in energy. A comparison of the phonon dispersions of these two phases reveals that a phase transition occurs due to a difference in vibrational free energy. The transition is of order-disorder type. Our calculated phase transition temperature is 680 K, in decent agreement with the experimentally determined 470 K. An alternative theoretical model yields 882 K. The phase transition is mediated by OH libration modes. We also report for the first time on a peculiarity in the phonon spectrum of hexagonal and monoclinic HA. When studying the Lyddane-Sachs-Teller shifts in the spectrum close to the Γ-point we identify two vibration modes showing a systematically increasing Lyddane-Sachs-Teller shift in frequency with decreasing dielectric constant. In experiment, the dielectric constant varies between 5 and 20 depending on the Ca/P ratio in the sample. The frequency shifts in the affected modes are

as large as 20 cm^{-1} as one spans the range of the dielectric constant. Thus, a simple spectroscopic analysis of a sample of bone may determine the quality of the sample in a physiological sense. We also identify the chemically stable low energy surface configurations as function of the OH, PO_4 and Ca concentration. In the experimentally relevant OH-rich regime we find only two surfaces competing for lowest energy. The surface most stable over almost the entire OH-rich regime is OH-terminated, and is currently being investigated in the presence of water and atomic substitutions on the HA surface.

Table of Contents

List of Tables xi

List of Figures xii

1. Introduction 1
   - 1.1 hydroxyapatite in nature and technology 1
   - 1.2 Existing literature on hydroxyapatite 3
   - 1.3 Our work on hydroxyapatite 6
   - 1.4 Other projects worked on 7

2. Theory and methodology 9
   - 2.1 Density Functional Theory (DFT) 9
     - 2.1.1 Schrödinger Equation in a plane wave basis representation 9
     - 2.1.2 Kohn-Sham-Equation 11
     - 2.1.3 Local Density Approximation (LDA) and Generalized Gradient Approximations (GGA) 13
     - 2.1.4 Pseudopotentials 13
     - 2.1.5 Self-consistency cycle 15
     - 2.1.6 VASP 16
   - 2.2 Theory of phase transitions 16
     - 2.2.1 Landau theory of phase transitions 18
     - 2.2.2 Displacive and order-disorder phase transition 20
     - 2.2.3 Minimum energy transition path 23
   - 2.3 Dielectric properties of ionic crystals 24
   - 2.4 Lattice vibrations and thermodynamic quantities in the harmonic approximation 26
   - 2.5 Surface and interface energetics from first principles 28
   - 2.6 Work functions and band alignment at interfaces from first principles 31
   - 2.7 Van der Waals interactions in DFT 33

3. First principles study of the biomineral hydroxyapatite 36
   - 3.1 Introduction 36

3.2 Computational details 40
3.3 Results 41
3.3.1 Ground state crystal structure 41
3.3.2 Activation energy for the hexagonal to monoclinic transition 46
3.3.3 Electronic structure 51
3.3.4 Phonon eigenmodes at the Γ-point 56
3.3.5 Elastic constants of HA 63
3.4 Conclusions 65
3.5 Appendix 66

4. First principles study of hydroxyapatite surface 67
4.1 Introduction 67
4.2 Computational details and surface models 69
4.3 Surface energy 73
4.4 OH-rich conditions 78
4.5 Work function 85
4.6 Conclusions 87

5. Hydroxyapatite: Vibrational spectra and phase transition 89
5.1 Introduction 89
5.2 Computational details 91
5.3 Results 92
5.3.1 Simulation cells and notations 92
5.3.2 Phonon dispersion 94
5.3.3 Lyddane-Sachs-Teller shift 100
5.3.4 Vibrational free energy and phase transition 108
5.3.5 Heat capacity C_V 115
5.4 Conclusions 117

6. TiO_2/HA and HA/H_2O interface 118
6.1 Introduction 118
6.2 TiO_2/HA interface: Wetting and electronic structure 119

6.3 Wetting at the HA/H_2O interface 124
6.4 Summary 128

References 130

Vita 139

List of Tables

Table 3.1: Comparison of fully relaxed theoretical bond lengths and bond angles in HA with experimental values.....45

Table 3.2: Born effective charge tensors for the different atomic sites. 60

Table 3.3: Calculated elastic constants and bulk modulus compared to other theoretical calculations and corresponding experimental values. The bulk modulus is related to the elastic constants by the formula $B = \frac{2}{9}\left(C_{11} + C_{12} + 2C_{13} + C_{33}/2\right)$. 64

Table 4.1: Chemical composition, ionic charge, the surface energy averaged over the entire chemical range and work function in our models. The 'extra' molecules indicate the deviation from HA bulk stoichiometry measured in numbers of OH, PO_4 or Ca. The net ionic charge is simply the sum of the extra elements multiplied by -3*e*, -1*e* and +2*e* for PO_4, OH and Ca, respectively. 72

Table 5.1 104

a) Fitting coefficients of the power law decay in Lyddane-Sachs-Teller frequency shift in hexagonal HA for increasing ε_∞.....104

Table 6.1: Energy calculated in the right hand side of equation (6.7). Negative energy means that H_2O wets the (doped) HA substrate, positive energy indicates that the substrate repels water. We find both ionically charged surfaces to repel water while the neutral ones are hydrophilic. 127

List of Figures

Fig. 1.1: Top-view on the hexagonal primitive cell. The z-axis is out of plane. We shifted the original primitive cell in the *x* and *y* directions such that the OH are in the center of the cell. The darker colored Ca_{II} atoms and PO_4 molecules are at z=0.25c, the lighter ones are at z=0.75c. The OHs in the center are also surrounded by six PO_4 molecules. The Ca_I atoms are now in the corners of the cell. 2

Fig. 1.2: The artificial hip implant on the left can be regarded as a multi-layer interface where a Ti substrate surface is oxidized, and then covered with a HA layer before it is immerged in the biological environment. 2

Fig. 2.1: Flow-chart for the self-consistent DFT calculations. 15

Fig. 2.2: Simple microscopic model describing the coupling between particles residing in a particular configuration of either the first or second of the two minima in each well. The interaction between nearest neighbor wells is mediated via a spring with spring constant *C*. 21

Fig. 2.3: Schematic of the NEBM method. The transition path from the initial position to the final position is guessed at first (dashed line). Relaxing the forces perpendicular to the transition path alters the path such that a lowest energy transition barrier is ensured when going from the initial to the final state. 24

Fig. 2.4: Schematic of a band alignment at the insulator/metal interface. χ is the semiconductor's electron affinity, E_{gap} its energy gap between the top of the valence band and the bottom of the conduction band, and Φ_m is the metal's work function. The p-type Schottky barrier φ_p is the energy difference between the Fermi level of the combined system and the top of the valence band. 32

Fig. 2.5: "Stairway to heaven" describing the step by step improvement in correcting functionals for dispersion interactions. 35

Fig. 3.1: Schematic of the HA crystallization during bone formation. Experiments suggest that the c-axes of both the tropocollagen and HA platelets are aligned [30]. The formation of bone tissue happens in several steps. After the tropocollagen helices are aligned, constituents of the HA crystal accumulate in the spaces between the tropocollagen and crystallize in the (001) orientation. The final HA mineral within the spaces consists of many separate HA platelets. 37

Fig. 3.2: HA primitive cells as described in references 5 and 6. The cell dimensions are a=b=9.432Å, c=6.881Å. The main difference between the two structures is the location of the oxygen atoms from the OH pairs as indicated in the figure. Following our notation (see text) we call the shown orientation of the OH pairs the (↓↓) orientation. 38

Fig. 3.3: Top-view on the hexagonal primitive cell. In the figure we shifted the original primitive cell in the x and y directions so that the OH column is in the center of the depicted cell. The darker colored Ca_{II} atoms and PO_4 molecules are centered at z=0.25c and the lighter ones are centered at z=0.75c. The OH column is surrounded by six Ca_{II} atoms and six PO_4 molecules. The Ca_I atoms are now in the corners of the cell. Below both of the two visible Ca_I atoms there is a second Ca_I atom at the distance 0.5c. Here, the lighter Ca_I atom is close to the top face and the darker Ca_I atom is at ~0.5c. 43

Fig. 3.4: The calculated structures are listed in ascending order according to the binding energy per single cell and the minimum energy is shifted to zero. We find the lowest binding energy for the monoclinic (↓↓)(↑↑) configuration followed by the hexagonal (↓↓) structure. The energy difference these two is ~22meV/cell. The binding energies of structures 2-4 are identical. Structures with flipped OH pairs within the same column generally yield higher binding energy. 45

Fig. 3.5: a) OH positions with respect to the surrounding Ca_{II}-triangles. b) Two transition paths for the hydrogen atoms to flip from (↓↓) to (↑↑). 47

Fig. 3.6: Top-view along the OH column surrounded by Ca_{II} and PO_4. The dark Ca atoms are at z=1/4 and the light ones at z=3/4c. The OH pairs are in the center. There are three equivalent trajectories to flip the top OH-pair rotationally. One of them is indicated by projection 1. Once path 1 is selected there are 2 inequivalent ways to flip the bottom OH-pair as indicated by the dashed lines. 48

Fig. 3.7*:* The energy barriers corresponding to the translational (1) and rotational (2 and 3) hydrogen trajectories. The energy barrier for a translational displacement of the hydrogen atoms along the z-axis is approximately 3 times higher than that of the rotational transition. 49

Fig. 3.8: The total DOS (a) and site-projected DOS in the near-gap region (b) of hexagonal and monoclinic HA. The DOS is normalized to a hexagonal cell. The Fermi level is at zero energy. The band gap is 5.23 eV…..52

Fig. 3.9: The electronic band structure of hexagonal HA in the near gap region. The energy range in the gap region and is not shown for clarity. The band structure suggests that HA is an indirect band material. The lowest energy optical excitations are indicated. The dashed lines between M and K indicate nearly constant energy optical excitations.…….54

Fig. 3.10: The electronic band structure of hexagonal HA.…….55

Fig. 3.11: The theoretical phonon density of states at the Γ-point compared with the experimental IR and Raman active modes. Our Ca and PO_4 peaks are underestimated by ~10 %, while the OH modes are overestimated by ~10 %. 58

Fig. 3.12 a): The phonon frequencies at the Γ-point with and without the long-range correction. When applying the long-range correction we consider approaching the Γ-point from the M-point, the K-point and the A-point, corresponding to the directions (100), (110) and (001). We use the experimental values from Fowler and Markovic [21,22]. The direction of approach has little influence on the eigenmodes. The deviation from the experimental values is about 10%.....61

Fig. 3.12 b): The change in the phonon frequency when applying the long-range correction. We find almost identical changes when approaching along the (100) and the (110) direction (M to Γ and K to Γ, respectively). The largest change occurs for the mode at 318 cm^{-1} which corresponds to a pure OH libration mode. In the (001) direction (A→Γ) this mode is nearly unaffected by the long-range correction. 62

Fig. 4.1: a)-c) From these three prototypes we create all of other model surfaces by continuously removing the numbered particles. In total, we construct 29 surface models from the ones depicted. 71

Fig. 4.2: Surface energy averaged over the entire chemical range plotted as function of the surface net ionic charge. Models 2 and 19 are the stoichiometric (001) and (100) surfaces. Models 3 and 24 are the models with lowest surface energy under OH-rich conditions. 74

Fig. 4.3: Lowest surface energy ternary phase diagram. Only six of the surface models notably contribute to the energetic ground state. Thin lines indicate the phase boundaries between surfaces competing in energy. A thick dividing line indicates conditions under which the β-TCP formation is energetically possible. 76

Fig. 4.4: Surface energy under OH-rich conditions. Main contributors are structures 3 and 24. 79

Fig. 4.5: Side view of relaxed model 3. The surface is one of the low energy surfaces under OH-rich conditions. 79

Fig. 4.6: The side (a) and top (b) views of relaxed model 24. This surface has the lowest energy over most of the chemical range under OH-rich conditions. It is terminated just above the hydroxyl layer and allows for major reconstruction in order to bind OH to the surface. For pictorial purpose we show a periodically extended cell. c) OH-relaxation: Dark large balls are Ca 'deeper' in-plane than the light large Ca balls. In model 24 one of the Ca is missing, allowing OH to rotate. 80

Fig. 4.7: a) P-O-P angle distribution in model 3. On the surface we find large deviation from the bulk P-O-P angles. Below 4.6 Å from the surface, however, the bulk distribution is restored. b) Layer decomposed density of states of model 3. We show the top of the valence band only. The Fermi level is at 0 eV. 82

Fig. 4.8: a) P-O-P angle distribution in model 24. Below 4.5 Å from the surface bulk angle distribution is restored. The largest deviation from the bulk angles is 9° in one of the surface PO_4 molecules. b) Layer decomposed density of states of model 24. We show the top of the valence band only. The Fermi level is at 0 eV. 84

Fig. 4.9: Work function as a function of the net ionic surface charge. Surfaces with unbalanced PO_4^{3-} and OH^{1-} molecules have negative net charge; surfaces with unbalanced Ca^{2+} atoms have positive net ionic charge. The work function strongly depends on the surface chemistry, ranging from 3 eV to 9.5 eV. The range of experimental work function is indicated by the shaded bar. 86

Fig. 5.1: Top-view on the hexagonal primitive cell. We shifted the original primitive cell in the x and y directions so that the OH column is in the center of the depicted cell. The darker colored Ca_{II} atoms and PO_4 molecules are centered at z=0.25c and the lighter ones are centered at z=0.75c. The OH column is surrounded by six Ca_{II} atoms and six PO_4 molecules. The Ca_I atoms are now in the corners of the cell. Below both of the two visible Ca_I atoms there is a second Ca_I atom at the distance 0.5c. Here, the lighter Ca_I atom is close to the top face and the darker Ca_I atom is at ~0.5c.....93

Fig. 5.2: The plots show the restoring forces acting on displaced atoms in the force constant calculation. The forces decay quickly with distance from the displaced atom in both the hexagonal and monoclinic phase, and are well contained within our simulation cells. 96

Fig. 5.3 a): Phonon dispersion of the hexagonal phase of HA. The main molecular contributors to the vibrations are indicated in the plots.....97

Fig. 5.3 b): Phonon dispersion of the monoclinic phase of HA. The main molecular contributors to the vibrations are indicated in the plots.....98

Fig. 5.3 c): In the figure we highlight modes that deviate by at least 5 cm^{-1} between the hexagonal and monoclinic phonon dispersion. Indicated in the background is he hexagonal phonon dispersion for reference. The deviations mainly occur in the low frequency Ca and PO_4 modes, and the OH stretch and libration modes. 99

Fig. 5.4: Lyddane-Sachs-Teller frequency shift in hexagonal HA when approaching Γ along the (100) A→Γ and the (010) Y→Γ direction, shown in (a) and (b) respectively. For $\varepsilon_\infty = 5$ the phonon density of states is indicated for reference. Two frequency shifts are highlighted at 619 cm^{-1} and at 1034 cm^{-1}. Those two shifts follow a power law decay with increasing ε_∞.102

Fig. 5.5: Lyddane-Sachs-Teller frequency shift in monoclinic HA when approaching Γ along the (100) A→Γ and the (010) Y→Γ direction, shown in (a) and (b) respectively. For $\varepsilon_\infty = 5$ the phonon density of states is indicated for reference. Similarly to the hexagonal phase, two frequency shifts are highlighted at 607 cm^{-1} and at 1034 cm^{-1}. Those two shifts follow a power law decay with increasing ε_∞. 103

Fig. 5.6: Lyddane-Sachs-Teller shift in frequency of the low-frequency vibration mode at 619 cm^{-1} (a) and the high-frequency mode at 1034 cm^{-1} (b) in hexagonal HA. The value of the shift when approaching Γ from a particular direction is just the length of the vector from the origin in the plot to a point on the mesh in that direction.....106

Fig. 5.7: Lyddane-Sachs-Teller shift in frequency of the low-frequency vibration mode at 607 cm^{-1} (a) and the high-frequency mode at 1034 cm^{-1} (b) in monoclinic HA. The value of the shift when approaching Γ from a particular direction is just the length of the vector from the origin in the plot to a point on the mesh in that direction.....107

Fig. 5.8: Phonon density of states for the hexagonal and monoclinic phase. The differences are subtle, and due to the deviations in the phonon dispersion as indicated in Figs. 5.3 a)-c). 108

Fig. 5.9: Plotted is the difference in vibrational free energy *dF* between monoclinic and hexagonal HA. The transition temperature is 680 K.....110

Fig. 5.10: Initial displacement pattern during the phase transition monoclinic→hexagonal, obtained in Chapter 3 using the nudged elastic band method. Mainly hydrogen atoms are moving. 112

Fig. 5.11: Shown are the projection coefficients of the monoclinic (a) and hexagonal (b) Γ-point modes. The linear expansion using the Γ modes as basis leads to the closest overlap with the structural transition path from monoclinic to hexagonal (a) phase and vice versa (b).....114

Fig. 5.13: Difference in heat capacity $C_{hex} - C_{mon}$. (a), and heat capacity of hexagonal and monoclinic HA (b). The agreement between theory and experiment is excellent, only at higher temperature we find slight deviation. The difference between hexagonal and monoclinic phase heat capacity is very subtle.....116

Fig. 6.1: Schematic of the band alignment between rutile TiO_2 substrate and HA. The energy values are given with respect to the vacuum energy. HA's valence band top varies strongly in energy depending on the surface chemistry (Chapter 4). Some of the compositions can lead to unphysical charging of TiO_2's GGA conduction band. This charging occurs due to GGA's inability to reproduce the correct energy gap between conduction and valence band. Instead, we use the GGA+U approach with $U = 9$ eV to increase TiO_2's band gap up to 3 eV (exp.: 3.06 eV), preventing unphysical charging of the TiO_2 layer. 120

Fig. 6.2: a) Charge neutral interface model between the TiO_2 substrate and the HA layer. We find this interface to be non-wetting. However, when removing the oxygen and calcium (indicated by the arrows) at the interface we satisfy the wetting condition (b). The interface in (b) remains charge neutral. In c) we show our relaxed (110)TiO_2/(100)HA interface model. We apply -6.8 % × -5.9 % compressive strain on HA's in-plane lattice constants. The TiO_2 substrate is 15.7 Å thick, and the HA layer is 20.6 Å thick. We find the distance 0.8 Å between the two layers to minimize the energy.....121

Fig. 6.3: Shown are HA's surface energy σ_{HA} for OH-rich conditions as a function of the chemical potential μ_{Ca}, and - ($\sigma_i - \sigma_{TiO2}$) calculated in equation (6.4). HA surface terminations with σ_{HA} smaller than - ($\sigma_i - \sigma_{TiO2}$) wet the TiO_2 substrate. We find that over almost the entire chemical range a multitude of HA surface terminations satisfy the wetting condition!123

Fig. 6.4: Layer projected electronic density of states in the TiO_2/HA interface model. The Fermi level is pinned by HA's valence band top, mainly contributed to by oxygen p-states. In the bulk regions the band offset between TiO_2's top of the valence band and HA's top of the valence band is ~0.5 eV.124

Fig. 6.5: HA/H_2O interface model. We substitute the indicated atoms by Si, Na or Mg to simulate the doped HA surface's interaction with water. The HA layer is ~20 Å thick. The HA surface is covered with a12 Å thick water layer, followed by vacuum.....126

1. Introduction

1.1 HYDROXYAPATITE IN NATURE AND TECHNOLOGY

A carbonated form of hydroxyapatite (HA, Fig. 1.1) [$Ca_{10}(PO_4)_6(OH)_2$] is one of the most abundant materials in human bone [1]. The bone matrix is a hierarchical structure composed of collagen fibers (large protein molecules) and HA crystallites. The HA crystallizes within small spaces between these proteins. While HA is brittle and the proteins soft, their combination gives bone its strength. However, with age this strength decreases as the mineral content in human bone decreases after reaching a maximum value, which leads to diseases such as osteomalacia (loss of bone mineral) [2]. Therefore, the obvious application of HA as a biomaterial is in the field of bone repair and bone replacement in form of orthopedic implants. HA's biocompatibility makes it very attractive in the orthopedic field, as state of the art bone implants are made of Ti(O_2) substrates which are coated with a thin HA layer on the surface [3]. While the metal offers excellent mechanical properties, the HA layer improves adhesion to the surrounding bone and provides a scaffold for bone growth. However, such implants have a serious short-coming as their life span typically only ranges from 5-10 years [3]. While attempts are made to increase the life span, the existing body of work on HA is mainly experimental and macroscopic in nature. However, to improve implants, such as the one displayed in Fig. 1.2, a thorough theoretical understanding on the microscopic level is needed as well. From the materials science point of view, the problems are associated with the molecular level interactions that govern the physics and chemistry of HA, HA/water, HA/metal and HA/organic interfaces (Fig. 1.2). And while HA has been studied previously (see next section), many of even its bulk properties – which should be the starting point before reaching out for the HA/metal or HA/water interfaces – remain poorly understood. In the following sections 1.2 and 1.3 I review the bulk of existing

literature on HA, and summarize the contribution of this dissertation to the understanding of HA.

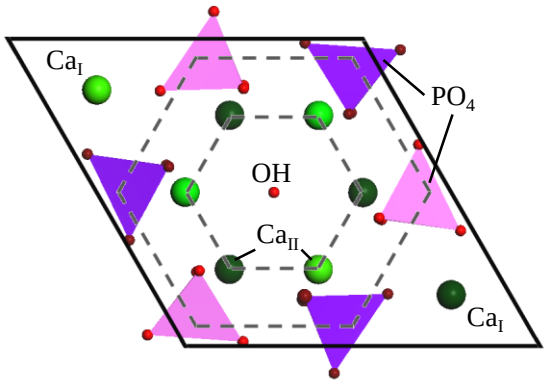

Fig. 1.1: Top-view on the hexagonal primitive cell. The z-axis is out of plane. We shifted the original primitive cell in the *x* and *y* directions such that the OH are in the center of the cell. The darker colored Ca_{II} atoms and PO_4 molecules are at z=0.25c, the lighter ones are at z=0.75c. The OHs in the center are also surrounded by six PO_4 molecules. The Ca_I atoms are now in the corners of the cell.

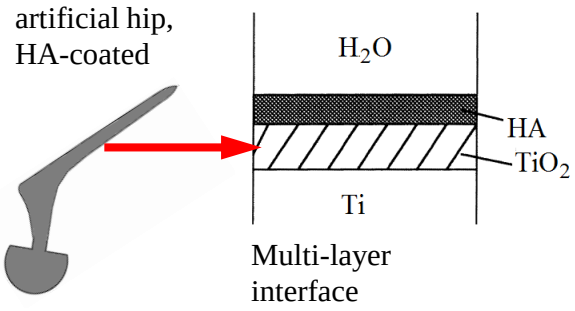

Fig. 1.2: The artificial hip implant on the left can be regarded as a multi-layer interface where a Ti substrate surface is oxidized, and then covered with a HA layer before it is immerged in the biological environment.

1.2 EXISTING LITERATURE ON HYDROXYAPATITE

The earliest reported experimental work on HA dates back to 1936 [4]. In his work on dental enamel, Schmidt demonstrated that the crystallographic *c*-axes of the HA platelets within the collagen framework are well aligned with collagen fibrils indicating a preferred orientation in the crystal growth. The actual crystal structure and atomic positions of HA were only determined somewhat later by Posner *et al.* in 1958 using the X-ray diffraction [5], and refined by Kay and co-workers in 1964 [6]. At that time, HA was believed to only crystallize in the hexagonal $P6_3/m$ structure until Young suggested a monoclinic variant of HA in 1967 [7], which was later described in more detail by Elliott and co-workers [8]. Young inferred that a HA crystal sufficiently free of impurities and vacancies could crystallize in the monoclinic phase analogous to the then already known monoclinic chlorapatite. The monoclinic variant of HA attracted some recent interest as the competition between two phases is not desirable in bone formation [*e.g.* 9-12]. In the 1980s Weiner *et al.* did further experimental investigation on HA crystallites which they disaggregated from natural bone. They found that the crystallites possessed a rather uniform thickness, however, varied strongly in their widths and lengths [13]. Some experimental work on the dielectric [14-18], thermodynamic [19,20] and vibrational properties [21,22] of HA has also been reported sporadically throughout the years.

Due to HA's complexity, only recently computational investigation of HA became feasible. Using density functional theory (DFT), de Leeuw analyzed the HA crystal structure and specifically the position and orientation of hydroxyl molecules [23]. She suggested that the experimentally found average OH orientational disorder in the crystal is due to locally ordered domains with differently oriented OH molecules. In the simplest static case, this is achieved in a monoclinic cell in agreement with experiment. Monoclinic and hexagonal HA are found to be very close in energy indicating no

particular preference for crystallization in a specific structure [24]. The phase transformation itself was subject to several publications which, however, typically only focus on the transition path and energy barrier height, leaving out the mechanisms inducing the transition [11,25,26]. The bulk electronic structure was subject to several theoretical studies [23,24,27,28]. Using a classical shell-model Calderin *et al*. investigated the lattice dynamics, calculated thermal factors and simulated the infrared spectra of HA finding only good agreement with experiment for the low-frequency and high-frequency vibrational modes at the Γ-point [29].

With increasing use of HA in in the medical field, focus was also put on growth kinetics measurements and surface studies of HA. In [30] and [31] Kanzaki *et al.* and Kazuo *et al.* measured the growth rate of the HA (001) surface using Moire phase shift interferometry. Chappell *et al.* used NMR to probe the (100) HA surface [32]. Comparison between the calculated and measured chemical shifts of ^{31}P can help modeling the surface observed in experiment. The ^{31}P chemical shifts in the surface phosphorous are found to be different from the bulk caused by relaxation of the surface phosphate molecules. More recently, classical and quantum-mechanical molecular dynamics simulations have been used to study energetically preferred surface orientations and terminations [27,32-34,]. So far these studies have been limited to only few surface terminations due to the complexity of the crystal. These studies also include work that takes the effect of surface impurities on electronic and chemical properties into account. They are important when trying to understand and modulate bioactivity of HA with surface impurities. For example, in a recent work Bertinetti *et al.* studied the effect of Mg surface enrichment on the apatitic morphology, surface hydration and cationic environment [35]. Using the near-infrared and medium-infrared spectroscopy Bertinetti found that Mg-enriched HA surfaces adsorb more H_2O molecules than the pure surfaces. Other ionic substitutions were also tried. For

example, de Leeuw analyzed the segregation of fluoride ions at the hydrated HA (001) surface using a combination of DFT methods for electronic structure calculations, shell models for larger systems and classical MD to simulate the uptake of fluoride and the interaction with water molecules [34,36,37]. She found that replacing surface OH by fluoride prevents the dissolution of the HA surface when facing water. Furthermore, Chappell and Bristowe have studied the influence of substituting phosphorus with silicon on the HA crystal and electronic structure [38]. The idea relates to experimental results dating back to 1970 when Carlisle found increased bioactivity in HA when it contains small amounts of silicon. However, while reporting on the energetic preference of Si doping, they did not answer the original question of why or how silicon affects HA's bioactivity. The reasons for the increase in bioactivity remain not understood to date. Other recent theoretical studies of doping the HA surface include the introduction of carbonate ions (CO_3^{2-}) to study physiologically found carbonated form of HA, and calcium substitution by titanium and strontium to induce structural modifications [34,39,40].

Even more sophisticated studies on the adsorption of small molecules such as amino acids on the HA surfaces covered with water also became tractable recently [27,34,37,41-48]. That work can yield valuable information when trying to identify the growth kinetics of HA crystallites in the physiological environment. Kandori *et al.* for example studied the adsorption of proteins onto HA through ionic concentration measurements [42-44]. In another work de Leeuw *et al.* used an interatomic potential based MD simulation to analyze the adsorption of citric acid with the HA surfaces (001) and (010) in aqueous environment [45]. They found that citric acid prefers to adsorb to the (010) surface thus reducing the growth of this face and indicating that HA should grow faster in the (001) direction in the presence of citric acids. More extensive simulations were performed by

Almora-Barrios *et al.* who used DFT methods to analyze the interaction between Glycine, Proline and Hydroxyproline to the same (001) and (010) surfaces as used by de Leeuw [37,46].

While the existing body of both experimental and theoretical work demonstrates an increasing level of sophistication throughout the years, important questions even on HA bulk are typically left out. In this dissertation I will address some of them with the goal to create a more complete picture of HA.

1.3 OUR WORK ON HYDROXYAPATITE

In this dissertation I report our work on the HA bulk properties, the phase transformation between the two known hexagonal and monoclinic phases, and a study on the surface energetics of HA. I also present a preliminary discussion on the HA/water and the TiO_2/HA interface that is relevant in orthopedic applications. The inter-atomic forces in HA span the entire range from strong metallic, covalent and ionic to weaker dispersive, hydrogen type bonds. This requires a theory that can accurately treat a wide range of inter-atomic forces and accurately predict materials properties. Thus, our method of choice in this work is DFT which has been used successfully throughout the years in materials studies. The rest of this dissertation is structured as follows. In Chapter 2 I establish a theoretical background of the methods used. In Chapter 3 I present our work on bulk HA. We identify the lowest energy bulk structures and compare their structural, electronic, and mechanical properties. We study the phase transition between the two lowest energy bulk structures. In Chapter 4 I summarize our work on the HA surface. We identify the surfaces most stable under given chemical conditions, putting particular focus on the energetically most stable surface under OH-rich conditions which closest mimics

the physiological environment. Our results are later used in Chapter 6. Chapter 5 summarizes our work on the vibrational properties of HA's hexagonal and monoclinic phase. We calculate the theoretical transition temperature, and identify the mechanisms responsible for the phase transition from monoclinic to hexagonal phase. We also identify and discuss a peculiarity in HA's Lyddane-Sachs-Teller frequency shift in the phonon dispersion that might be of use in either preventive medical screenings to identify the condition of a bone sample, or in the quality control field of medical implants. From the vibrational data we deduce important thermodynamic properties of HA. In Chapter 6 I present a preliminary study of the TiO_2/HA and the HA/H_2O interface.

1.4 OTHER PROJECTS WORKED ON

Of my work during my studies at UT Austin only the part on HA is presented in this dissertation. However, I had been involved in several other projects besides the work on HA. Other projects I had been involved in:

- *Electrical resistivity in metals and metallic alloys from first principles,* **A. Slepko**, J. Weber, A. A. Demkov, S. Shankar, in preparation.

- *Epitaxial Zintl aluminide $SrAl_4$ on $LaAlO_3$ substrate*, L. Schlipf, **A. Slepko**, A. Posadas, H. Seinige, A. Dhamdhere, M. Tsoi, D. Smith and A. A. Demkov, submitted to Phys. Rev. B.

- *Theoretical investigation of zb AlN/metal interfaces*, **A. Slepko**, A. A. Demkov, in J. Appl. Phys. **113**, 013707 (2013).

- *First principles study of $SrAl_2$*, **A. Slepko**, A. A. Demkov, Phys. Rev. B **85**, 195462 (2012).

- *Band engineering in silicide alloys*, **A. Slepko**, A. A. Demkov, Phys. Rev. B **85**, 035311 (2012).

- *Work function engineering in silicides: chlorine doping in NiSi*, **A. Slepko**, A. A. Demkov, W.-Y. Loh, P. Majhi and G. Bersuker, J. Appl. Phys. **109**, 083703 (2011).

- *Formation of single-orientation epitaxial island of $TiSi_2$ on Si(001) using Sr passivation*, A. Posadas, R. Dargis, M. R. Choi, **A. Slepko**, A. A. Demkov, J. J. Kim and D. J. Smith, J. Vac. Sci. Technol. B **29**, 03C131 (2011).

2. Theory and methodology

2.1 Density Functional Theory (DFT)

DFT uses the key observation that for an interacting N-electron system in a general external potential $V(\vec{r})$ the total energy E of the ground state is a unique functional of the electronic density $n(\vec{r})$. Hohenberg and Kohn showed that this total energy functional $E[n]$ is minimized by the true ground state density $n(\vec{r})$ [49]. However, the energy functional is not known exactly and must be approximated in practice. Kohn and Sham suggested an ansatz for the case of a slowly varying density [50]. That leads to the local density approximation (LDA) and the generalized gradient approximation (GGA) and Kohn-Sham equations and is discussed in more detail in Chapter 2.1.3. In this work we use the VASP code where the Kohn-Sham equations are solved by using a set of plane waves, the LDA or the GGA in combination with pseudopotentials [51-55]. Thus, we briefly discuss the Schrödinger equation in a plane wave basis representation before we derive the Kohn-Sham equations and give an overview of the LDA/GGA and the concept of pseudopotentials.

2.1.1 Schrödinger Equation in a plane wave basis representation

In the single electron picture with a lattice periodic potential $U(\vec{r})$ the Schrödinger equation is given by:

$$\left[-\frac{\hbar^2}{2m}\Delta + U(\vec{r})\right]\psi_i(\vec{r}) = E_i\psi_i(\vec{r}). \tag{2.1}$$

This equation can be solved using the Bloch's theorem

$$\psi_{n\vec{k}}(\vec{r}+\vec{R}) = e^{i\vec{k}\vec{R}}\psi_{n\vec{k}}(\vec{r}), \tag{2.2}$$

where $\vec{R}$ is a translational vector of the Bravais lattice. That implies the property

$$\psi_{n\vec{k}}(\vec{r}) = e^{i\vec{k}\vec{r}} u_{n\vec{k}}(\vec{r}), \tag{2.3}$$

where $u_{n\vec{k}}(\vec{r})$ is a periodic function with the same periodicity as the potential $U(\vec{r})$. As $u_{n\vec{k}}(\vec{r})$ is a lattice periodic function it can be expanded into a lattice Fourier sum:

$$u_{n\vec{k}}(\vec{r}) = \sum_{\vec{G}} c_{n,\vec{k}+\vec{G}} e^{i\vec{G}\vec{r}}. \tag{2.4}$$

To maintain the periodicity of the $u_{n\vec{k}}(\vec{r})$ the $\vec{G}$-vectors in the expansion are chosen to be the reciprocal lattice vectors.

Substituting equation (2.2) with the expansion (2.4) into equation (2.1), multiplying both sides by $e^{-i(\vec{k}+\vec{G}')\vec{r}}$ and integrating over a primitive cell of the lattice yields:

$$\int d^3\vec{r} \cdot \sum_{\vec{G}} \left[\frac{\hbar^2}{2m}\left(\vec{k}+\vec{G}\right)^2 + U(\vec{r})\right] \cdot e^{i(\vec{G}-\vec{G}')\vec{r}} \cdot c_{n,\vec{k}+\vec{G}} = E_{n\vec{k}} \cdot V_{Cell} \cdot c_{n,\vec{k}+\vec{G}'}. \tag{2.5}$$

Or equivalently:

$$\sum_{\vec{G}} \left[\frac{\hbar^2}{2m}\left(\vec{k}+\vec{G}\right)^2 \cdot \delta_{\vec{G},\vec{G}'} + u_{\vec{G}-\vec{G}'}\right] \cdot c_{n,\vec{k}+\vec{G}} = E_{n\vec{k}} \cdot c_{n,\vec{k}+\vec{G}'}. \tag{2.6}$$

Where the $u_{\vec{G}-\vec{G}'}$ are the Fourier coefficients of the potential $U(\vec{r})$. In practical calculations the sum on the left side has to be limited by imposing a cutoff energy given by

$$\frac{\hbar^2}{2m}\left(\vec{k}+\vec{G}\right)^2 \leq E_{cut}. \tag{2.7}$$

In a total energy calculation equation (2.6) is solved at a finite set of k-points which are usually chosen to be uniformly distributed over the Brillouin Zone. Alternatively when the electronic spectrum is sought equation (2.6) can be solved only for k-points lying in a certain direction, *e.g.* a high symmetry direction of the system under consideration. The calculated eigenvalue spectrum then gives the band structure of the system along that particular direction.

2.1.2 Kohn-Sham-Equation

Starting with the many-body Schrödinger equation the total ground state energy of a system can be written as

$$E = \langle \Psi | (T + U_{ee} + V) | \Psi \rangle. \tag{2.8}$$

where T is the kinetic energy operator, U_{ee} the interaction energy operator of the N electrons, V the external potential operator and Ψ a many electron wave function.
We can rewrite equation (2.8) to

$$E_{V(\vec{r})}[n] = \int V(\vec{r}) n(\vec{r}) d\vec{r} + F[n(\vec{r})], \tag{2.9}$$

where

$$F[n] \equiv \langle \Psi[\mathrm{n}] | (T + U_{ee}) | \Psi[\mathrm{n}] \rangle \tag{2.10}$$

is a functional of $n(\vec{r})$ and represents the kinetic and interaction energies. We rewrite (2.10) to

$$F[n] \equiv T_S[n] + \frac{e^2}{2} \int \frac{n(\vec{r}) n(\vec{r}')}{|\vec{r} - \vec{r}'|} d\vec{r} d\vec{r}' + E_{xc}[n]. \tag{2.11}$$

In (2.11) $T_S[n]$ is the kinetic energy of non-interacting electrons of density $n(\vec{r})$. The second part contains the electron-electron interaction energy of the system. $E_{xc}[n]$ is the so-called exchange correlation energy and contains all the remaining energy not considered in the first two summands. Minimization of equation (2.9) with respect to the density $n(\vec{r})$ using the variation principle yields the self-consistent Kohn-Sham equations:

$$\left[-\frac{\hbar^2}{2m}\Delta + V(\vec{r}) + \int \frac{e^2 \cdot n(\vec{r}')}{|\vec{r}-\vec{r}'|} d\vec{r}' + V_{XC}(\vec{r})\right] \psi_j(\vec{r}) = E_j \psi_j(\vec{r}), \tag{2.12}$$

with

$$V_{XC}(\vec{r}) \equiv \frac{\delta E_{xc}[n(\vec{r})]}{\delta n(\vec{r})} \tag{2.13}$$

and

$$n(\vec{r}) = \sum_{j=1}^{N} \left|\psi_j(\vec{r})\right|^2. \tag{2.14}$$

The total energy functional is then given by

$$E = T_S[n] + \int V(\vec{r}) n(\vec{r}) d\vec{r} + \frac{e^2}{2} \int \frac{n(\vec{r}) n(\vec{r}')}{|\vec{r}-\vec{r}'|} d\vec{r} d\vec{r}' + E_{xc}[n]. \tag{2.15}$$

It is worth noting that there are no simplifications done so far and equation (2.15) would in principle yield the correct energy if we knew the correct form of the exchange correlation energy term $E_{xc}[n]$!

2.1.3 Local Density Approximation (LDA) and Generalized Gradient Approximations (GGA)

Unfortunately, the exact exchange correlation energy $E_{xc}[n]$ in equations (2.12) and (2.15) is not known and has to be approximated in practice. The simplest approximation is the so called local density approximation (LDA) given by:

$$E_{XC}^{LDA}[n] \equiv \int \epsilon_{XC}[n(\vec{r})]n(\vec{r})d\vec{r}. \tag{2.16}$$

In equation (2.16) ϵ_{XC} is the exchange-correlation energy per electron of a uniform electron gas of density n. ϵ_{XC} is very well known from independent studies of the uniform electron gas including e.g. Quantum Monte Carlo methods [56]. Within that approximation the Kohn-Sham equation is local both in the sense that it acts only on the wave function at $\vec{r}$ and also in the sense that it depends only on the density at $\vec{r}$. However, this choice for $E_{xc}[n]$ is formally only justified for the case of small density gradients. Naturally, an improvement can be made by considering further gradient corrections to the $E_{XC}^{LDA}[n]$ which is called the Generalized Gradient Approximation (GGA) [57]. Frequently used forms for the GGA approximation are introduced by Perdew and Wang and Perdew, Burke and Ernzerhof [58,59]. The GGA sometimes corrects and sometimes overcorrects the LDA approximation.

2.1.4 Pseudopotentials

As already mentioned before, the concept of pseudopotentials was first introduced by Phillips and Kleinman [60]. Their construction is based on the use of a pseudo wave function for the valence states given by

$$|\varphi_v^{PS}\rangle = |\varphi_v\rangle + \sum_c \langle\varphi_c|\varphi_v^{PS}\rangle|\varphi_c\rangle. \tag{2.17}$$

In (2.17) the φ_v denotes the true valence wave function and the φ_c's the true core wave functions which are not known in practice and must be approximated. The sum runs over the core states. Applying the Hamiltonian of the system to $|\varphi_v\rangle$ leads to

$$\widehat{H}|\varphi_v\rangle = E|\varphi_v\rangle = \widehat{H}|\varphi_v^{PS}\rangle - \sum_c E_c|\varphi_c\rangle\langle\varphi_c|\varphi_v^{PS}\rangle \tag{2.18}$$

which can be rewritten into a Schrödinger-like equation

$$\left[T + V + \sum_c (E - E_c)|\varphi_c\rangle\langle\varphi_c|\right]|\varphi_v^{PS}\rangle = E|\varphi_v^{PS}\rangle \tag{2.19}$$

where the original potential term V is replaced by the Phillips-Kleinman pseudopotential

$$V^{PK} = V + \sum_c (E - E_c)|\varphi_c\rangle\langle\varphi_c| = V + V^R. \tag{2.20}$$

In (2.20) the term V is still the original potential and V^R an additional contribution. V^R is repulsive as the core energies E_c are lower than the valence energies E. Moreover, as V^R depends on the core wave functions it vanishes outside a certain core region so that the Phillips-Kleinman pseudopotential becomes equal to the original potential. Inside that core region the contribution of V^R makes the original potential much weaker so that e.g. plane wave expansions of the pseudo wave functions show a reasonable convergence.

In later work norm conserving pseudopotentials were introduced [61]. Those norm conserving pseudopotentials are constructed to be equal to the actual potential outside a core radius r_c and differ from it inside r_c. The pseudo wave functions are constrained to give the same norm as the correct wave functions inside r_c, e.g.

$$\int_0^{r_c} dr\, r^2\, \psi_{PS}^*\, \psi_{PS} = \int_0^{r_c} dr\, r^2\, \psi^*\, \psi, \tag{2.21}$$

where the ψ is the correct wave function. Then an approach was suggested by Vanderbilt and co-workers where the concept of norm conservation was waived to give rise to the concept of ultrasoft pseudopotentials [62,63,64]. In ultrasoft pseudopotentials the pseudo

wave functions are equal to the correct all-electron wave functions outside r_c but are allowed to be as soft as possible inside r_c which conflicts with the concept of the norm conservation. The term "as soft as possible" means that the concept allows plane wave expansions for the pseudo-wave function using as few plane waves as possible. That concept can reduce the needed plane wave cutoff in calculations.

2.1.5 Self-consistency cycle

Together with the concept of pseudopotentials and the LDA/GGA approximations for the exchange correlation energy the Schrödinger-like Kohn-Sham equations can be solved self consistently using a plane wave set as a basis as described in Chapter 2.1.1. Fig. 2.1 gives a schematic overview of the procedure.

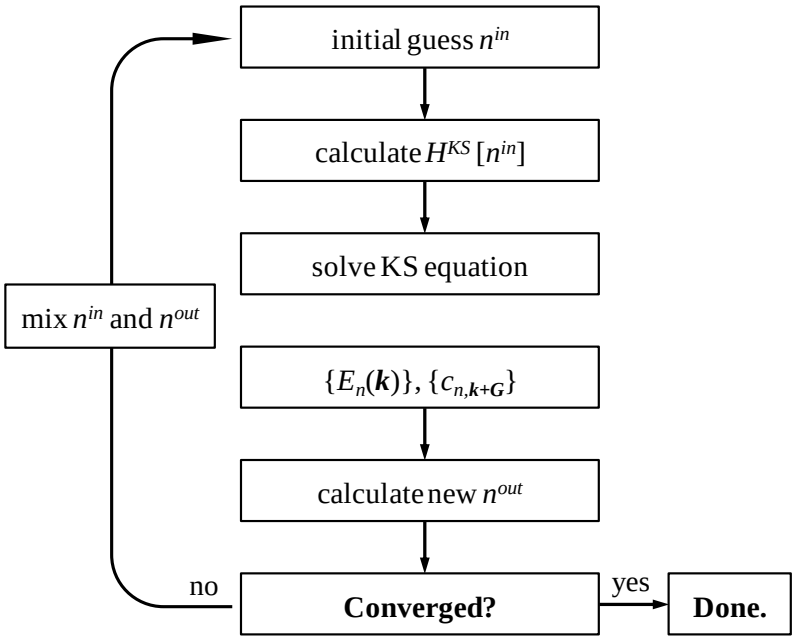

Fig. 2.1: Flow-chart for the self-consistent DFT calculations.

2.1.6 VASP

All calculations in this work are performed using the Vienna Ab-initio Simulation Package (VASP) written by Georg Kresse and Jürgen Furthmüller [51,52,53,54,55]. VASP was developed to calculate the Kohn-Sham ground states of metallic system. However, it also has been used very successfully in systems of liquid and amorphous semiconductors, liquid simple and transition metals, metallic and semiconducting surfaces, phonons in simple metals, transition metals and semiconductors. VASP uses pseudopotentials and plane waves as a basis as well as an efficient mixing scheme for the computed charge densities based on Pulay's scheme [65].

2.2 THEORY OF PHASE TRANSITIONS

Phase transitions are commonly observed phenomena in nature including for example liquid-solid, gas-liquid, metal-insulator, ferromagnetic, or structural phase transitions just to name a few. Phase transitions occur in both solids and liquids, in real space (structural transition) and momentum space (superconductivity), and they can span a large temperature range (ferro-/paramagnetism transition at 10s of Kelvin compared to superfluidity transition at very low temperature). In our work on HA we are concerned with the structural phase transition leading HA from the monoclinic to hexagonal phase. We will establish the type of transition occurring and calculate the transition temperature. In what follows I quickly summarize the most commonly used classification schemes for phase transitions, and establish a theoretical background for our work.

A very commonly used scheme to classify phase transitions dates back to Ehrenfest who used the order of derivative at which a characteristic thermodynamical potential becomes discontinuous at a certain critical temperature T_c [*e.g.* 66]. In this scheme the most commonly known types of phase transitions are of first and second order, *i.e.* the first and

second order derivatives, respectively, become discontinuous. The first order derivative of a free energy yields physical quantities such as the volume, entropy or magnetic moment. Phase transitions of first order involve latent heat, *i.e.* the system either absorbs or releases a certain amount of energy during the transition. The second order derivative of a free energy gives information about the specific heat of the system, its compressibility or its magnetic susceptibility. The gas-liquid phase transition is of first order for example, and the ferromagnetic transition is an example for a second-order transition. Within this classification scheme variations in the solid phase transitions can occur, meaning that the mechanisms mediating the transition may vary from solid to solid. These variations lead to a difference in the nature of the transition [67, 68]:

1) Displacive transition: Follows from small bond or rotational distortions. A displacive transition can be of first or second order.
2) Reconstructive transitions: These transitions are due to breaking bonds to nearest neighbor or second nearest neighbor atoms.
3) Order-disorder transitions: Typical kinds of the transition are positional or orientational disordering of atoms, and disordering associated with electronic and nuclear spin states. We will be interested in the positional disordering in HA. Those transitions arise either when atoms occupy inappropriate sublattice positions, or when more energetically equivalent atomic positions are available than are necessary.

We will show in our work that the HA monoclinic-hexagonal solid phase transition is of order-disorder type. In the following chapters I will provide the theoretical background

necessary to calculate and interpret the energy landscape of the transition, and to deduce the transition temperature.

2.2.1 Landau theory of phase transitions

The Landau theory is one of the most commonly and universally applied methods when describing the energy landscape of a system undergoing a second order phase transition [69]. The theory uses the fact that as a consequence of a phase transition the system changes macroscopically such that some of the original symmetry elements may vanish. This is referred to as the broken symmetry concept. The transformation from the higher to the lower symmetry phase and *vice versa* is described with help of a physical parameter η. The parameter is chosen such that it is zero in the high symmetry phase, and takes on a nonzero value in the low-symmetry phase. The parameter η is not well defined, it can for example describe an atomic position or bonding angle. It is clear, however, that a change in η must be accompanied by a change in some energy. Landau suggested using the Gibbs free energy G to describe the thermodynamic energy landscape as a function of the pressure p, temperature T, and the order parameter η. The order parameter must thus be a function of p and T. Such a system must allow for energy minima in order to have a stationary solution, therefore, the following conditions must apply:

$$\partial G/\partial \eta = 0 \quad \text{and} \quad \partial^2 G/\partial \eta^2 > 0\,. \tag{2.22}$$

In spite of the continuity in G in a second order phase transition the order parameter η may take on arbitrarily small values. Thus, close to the transition temperature T_c the energy must be expandable in powers of η. For scalar η the Gibbs free energy becomes:

$$G(p,T,\eta) = G_0(p,T) + \frac{1}{2}A\eta^2 + \frac{1}{4}B\eta^4 + \cdots. \tag{2.23}$$

The term first order in η is not present due to the condition $\partial G/\partial \eta = 0$. For a second order transition it suffices to truncate the expansion after the quartic term. Then, B must be larger than zero as G must be an increasing function of η. In thermal equilibrium we find

$$\eta = 0\,, \quad \eta = \pm\sqrt{-\frac{A}{B}}\,. \tag{2.24}$$

For $A>0$ and $B>0$ $\eta = 0$ is the only real solution representing the disordered state above T_c., For $A<0$ and $B>0$, equation (2.24) gives a real solution representing the ordered state below T_c. The theory must allow for both, positive and negative A, depending on whether the system resides in the high or low symmetry phase. Landau suggested to write

$$A = A'\left(T - T_c\right), \quad A' > 0\,. \tag{2.25}$$

The change in sign of A occurs at the transition temperature. From that it becomes clear that the quartic term in equation (2.23) is required since the quadratic term vanishes at T_c; however, the temperature dependence in B is typically ignored. At the critical temperature the entropy is given by:

$$S = -\left(\frac{\partial G}{\partial T}\right)_p = \begin{cases} S_0\left(T_c\right) & , \; T \to T_c^+ \\ S_0\left(T_c\right) + \dfrac{A'^2}{2B}\left(T - T_c\right) & , \; T \to T_c^- \end{cases}, \tag{2.26}$$

which is continuous at $T=T_c$. However, using equations (2.26) we find a jump in the specific heat at the critical temperature

$$C_p = -T\left(\frac{\partial S}{\partial T}\right)_p = \begin{cases} C_0\left(T_c\right) & , \; T \to T_c^+ \\ C_0\left(T\right) - \frac{A'^2}{2B}T_c & , \; T \to T_c^- \end{cases}, \tag{2.27}$$

The S_0 and C_0 arise from G_0 in equation (2.23). This jump in specific heat is characteristic for the second order phase transition.

The Landau theory can be modified to also describe first order phase transitions by adding the cubic and secant expansion term into account in equation (2.23). This ultimately leads to other equilibrium positions which, however, are derived equivalently to the case of the second order transition. I leave out the discussion on the first order modifications to the Landau theory as it is of no relevance to our work on HA.

2.2.2 Displacive and order-disorder phase transition

An often used model Hamiltonian to differentiate between and describe displacive and order-disorder type phase transitions is given by [70-72]:

$$H = \sum_{l} \frac{p^2(l)}{2m} + \sum_{l} V_s(u(l)) + \frac{C}{2} \sum_{l,l'} (u(l) - u(l'))^2 , \tag{2.28}$$

where the u and p describe displacements and momenta of the displaced particle. In analogy to Landau's approach these particles reside in a double-well single particle potential V_s given by

$$V_s(u) = -\frac{A}{2}u^2 + \frac{B}{4}u^4 . \tag{2.29}$$

The coupling constant C in equation (2.28) takes into account whether two particles in neighboring wells prefer to be located on the symmetrically equivalent side of the potential well or rather prefer to align anti-parallel or in a more complicated mixed fashion as indicated in Fig. 2.2.

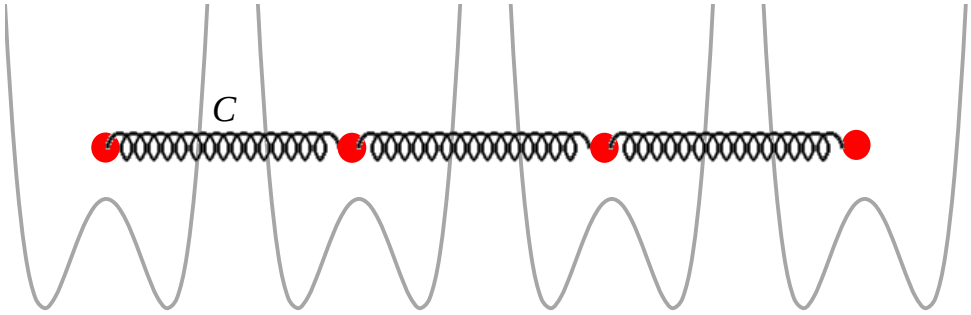

Fig. 2.2: Simple microscopic model describing the coupling between particles residing in a particular configuration of either the first or second of the two minima in each well. The interaction between nearest neighbor wells is mediated via a spring with spring constant C.

The model (2.28) provides two important quantities, the depth of the potential V_s

$$V_0 = \frac{A^2}{4B}, \tag{2.30}$$

and the interaction energy of a pair of particles positioned at the energy minima $\pm u_0$:

$$W = 2C\frac{A}{B}, \tag{2.31}$$

where A and B are the expansion coefficients of the single particle potential well in (2.29). The parameter V_0 is the barrier height for a particle to overcome when moving between the two minima of V_s, whereas the parameter W is the difference in energy when two neighboring particles reside on the symmetrically equivalent well-side or align anti-parallel. The ratio $s = \frac{V_0}{W}$ between both is an indicator whether the transition is of order-disorder type (s>>1) or displacive (s<<1) in nature. The model Hamiltonian in (2.28) allows for a phase transition, which is plausible from the following considerations. When neglecting the inter-well correlations at high temperature the average position of an atom

in a double well $<u(l)>$ must be zero. However, at zero temperature the atoms should arrange statically in only one of the two potential wells in an energetically preferred pattern. The only necessary condition is that the expansion coefficient A in (2.29) is larger than zero, *i.e.* V_s is indeed a double well potential. Sarbach has shown that this condition is also a sufficient condition for the existence of a phase transition in systems with dimension higher than 2 [73]. In the order-disorder limit the dominant energy barrier to overcome for an individual particle ensures that all particles reside close to the bottom of one of the two potential wells. In that case the critical temperature is given by [71,74]

$$T_c = 4dk(d)C\frac{A}{Bk_B} = 2k(d)\frac{W}{k_B}, \tag{2.32}$$

where d is the dimensionality of the system. W can be calculated easily using first-principles methods. The numerical factor $k(d)$ has been tabulated in the work by Fischer [74]. For the displacive limit it can be shown that the transition temperature is given by [75].

$$T_c = \frac{4}{d\,q(d)}C\frac{A}{Bk_B}. \tag{2.33}$$

Again, the numerical factor $q(d)$ has been tabulated [75]. We will show later in this dissertation that the phase transition in HA is of order-disorder type, thus we will use equation (2.32) to evaluate the transition temperature. Note, that the temperature in (2.32) does not depend on the barrier height V_0 or the potential expansion coefficients A and B, indicating that the actual transition path does not matter when calculating the transition temperature. Despite that fact, the actual transition path is often of practical importance as we stress in the next paragraph.

2.2.3 Minimum energy transition path

In some studies it is instructional to know the transition path a system will take during its transition from phase A to phase B. It is key to understanding the dynamics of a phase transition. In particular, accurately knowing the energy barrier to overcome can be used to estimate quantities such as reaction rates. In *ab-initio* calculations the method of choice to study such transition problems and identify reaction paths is the Nudged Elastic Band Method (NEBM) [76,77]. In the method the minimum energy path is guessed at first with a finite number of intermediate "images" in which the transiting atom for example changes position from its initial position to its final position. Next, the 3N dimensional force acting on each image is defined:

$$\vec{F}_i^{\,0} = -\vec{\nabla}V\left(\vec{R}_i\right)_{\perp} + \left(\vec{F}_i^{\,s} \cdot \hat{\tau}_{\parallel}\right)\hat{\tau}_{\parallel}, \tag{2.34}$$

with

$$\vec{F}_i^{\,s} = k_{i+1}\left(\vec{R}_{i+1} - \vec{R}_i\right) - k_i\left(\vec{R}_i - \vec{R}_{i-1}\right). \tag{2.35}$$

Equation (2.34) replaces the force acting on the system parallel to the defined transition path by an effective spring force which acts between nearest neighbor images. The spring force only affects the distribution of the images within the transition path, thus the choice of k_i is rather arbitrary. When the spring force is neglected, the interaction between nearest neighbor images leaves forces acting on each image only perpendicular to the transition path. It is this perpendicular component that allows the system to distort around the transition path ensuring that the transition barrier is the lowest in energy (Fig. 2.3 for clarification). Using the force defined by (2.34) to relax the images guarantees at least a local minimum of the transition path and thus the lowest possible energy barrier associated with the guessed transition path.

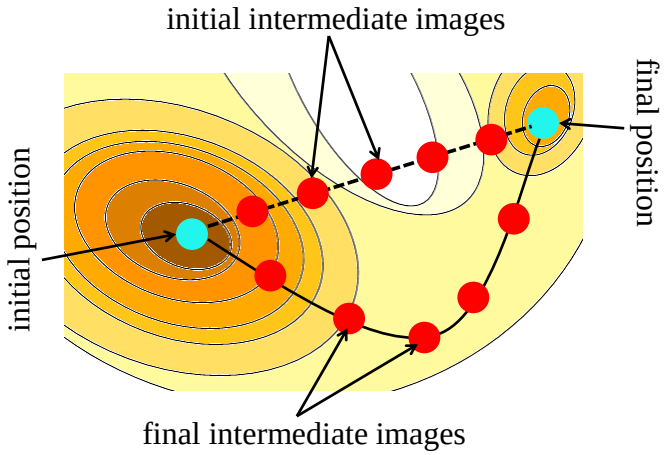

Fig. 2.3: Schematic of the NEBM method. The transition path from the initial position to the final position is guessed at first (dashed line). Relaxing the forces perpendicular to the transition path alters the path such that a lowest energy transition barrier is ensured when going from the initial to the final state.

2.3 DIELECTRIC PROPERTIES OF IONIC CRYSTALS

HA is an ionic crystal, consisting of the building blocks $(PO_4)^{3-}$, Ca^{2+} and OH^-. We will be using the Born effective charge tensors of these building blocks when studying HA's vibration spectra and thus want to first establish the theoretical background. The modern description of the theory of the polarization of crystals was introduced in the 1990s [78]. The definition of polarization is

$$\frac{d\vec{P}}{dt} = \vec{j}(t), \tag{2.36}$$

where $\vec{P}$ is the polarization density of a material, and $\vec{j}$ the macroscopic current density. Integrating (2.36) yields the change in polarization density:

$$\Delta\vec{P} = \int_0^T \vec{j}(t')dt' . \tag{2.37}$$

That means that the polarization of a material at given time T is not obtained from only measuring it at that time but is rather a measurement over a time period [79]. Equation (2.37) can be rewritten when assuming an adiabatic change in time, starting at zero for the initial state of the system and running to one for the final state:

$$\Delta\vec{P} = \int_0^1 d\lambda \frac{d\vec{P}}{d\lambda}. \tag{2.38}$$

Equation (2.38) can be reformulated with the help of the Berry curvature tensor [78]:

$$\Delta\vec{P} = -f \times e \sum_n \int_0^1 d\lambda \int_{BZ} \frac{d\vec{k}}{(2\pi)^3} \Omega^n_{\vec{k},\lambda}, \tag{2.39}$$

where f accounts for opposite spins, and n runs over energy bands. In (2.39) the Berry curvature tensor $\Omega^n_{\vec{k},\lambda}$ is given by

$$\Omega^n_{\vec{k},\lambda} = i\left\langle \frac{\partial}{\partial\vec{k}} u_{\vec{nk}} \middle| \frac{\partial}{\partial\lambda} u_{\vec{nk}} \right\rangle + c.c., \tag{2.40}$$

with $H\left|u_{\vec{nk}}\right\rangle = E_{\vec{nk}}\left|u_{\vec{nk}}\right\rangle$. The $u_{\vec{nk}}$ are lattice-periodic wave functions implicitly dependent on λ, and n the band index. Using (2.40) in (2.39) and integrating, the Berry phase formulation of the polarization is given by [78]:

$$\vec{P}(\lambda) = \frac{i \times f \times e}{(2\pi)^3} \sum_n \int_{BZ} d\vec{k} \left\langle u_{\vec{nk}} \middle| \nabla_{\vec{k}} \middle| u_{\vec{nk}} \right\rangle. \tag{2.41}$$

Knowing the polarization one can calculate the Born effective charge tensor of an atom which we will use in our work when dealing with the vibrational properties of ionic crystals. Its definition is

$$Z^i_{\alpha,\beta} = \frac{\partial P_\beta}{\partial r_{i,\alpha}}, \tag{2.42}$$

i.e. it describes the change in total polarization density of atom i in β-direction when displacing it in α-direction. The second dielectric quantity we use in our work on HA is the high frequency dielectric constant $\varepsilon^\infty_{\alpha\beta}$. However, instead of calculating it, we use the tabulated values found in experiment.

2.4 LATTICE VIBRATIONS AND THERMODYNAMIC QUANTITIES IN THE HARMONIC APPROXIMATION

Part of this dissertation is our work on HA's vibrational spectrum to identify vibrational energy differences favoring the phase transition from monoclinic to hexagonal phase. Thus, I first establish the underlying theory in the following. The understanding of lattice vibrations is of direct use when studying a variety of physical properties of crystals, such as its spectroscopic properties (Raman, infrared), its thermal properties (specific heat, thermal expansion), or the crystal's heat and electronic conduction properties [80-82]. Moreover, the phonon spectrum can reveal dynamical instabilities (soft-modes) that drive a crystal to change its crystal structure. In the harmonic approximation the assumption is that neighboring atoms in the lattice interact *via* springs. Depending on the distance between the atoms the spring constant is softer or stiffer. The energy for such a system can be written as

$$E\left(\left\{\vec{R}_{\kappa}^{\alpha}\right\}\right) = E_0 + \sum_{a,\kappa,\alpha b,\kappa',\beta}\sum \frac{1}{2}\frac{\partial^2 E}{\partial u_{\kappa,\alpha}^{a}\partial u_{\kappa',\beta}^{b}} u_{\kappa,\alpha}^{a} u_{\kappa',\beta}^{b} \tag{2.43}$$

in the harmonic approximation. The first order derivative term drops out as in the equilibrium position the first derivative is zero. The second order energy derivatives are the interatomic force constants

$$C_{\kappa\alpha,\kappa'\beta} = \frac{\partial^2 E}{\partial u_{\kappa,\alpha}^{a}\partial u_{\kappa,\beta}^{b}}, \tag{2.44}$$

Applying the classical equation of motion one obtains

$$M_{\kappa}\frac{\partial^2 u_{\kappa,\alpha}^{a}}{\partial t^2} = -\sum_{b,\kappa',\beta} C_{\kappa\alpha,\kappa'\beta} u_{\kappa',\beta}^{b}\,. \tag{2.45}$$

Equation (2.45) is solved with the ansatz

$$u_{\kappa,\alpha}^{a} = \frac{1}{\sqrt{M_{\kappa}}}\gamma_{\vec{m},\vec{q}}(\kappa\alpha) e^{i\vec{q}\vec{R}_a} e^{-i\omega_{\vec{m},\vec{q}}\vec{t}}. \tag{2.46}$$

Using the ansatz in (2.45) leads to the equation

$$\omega^2_{\vec{m},\vec{q}}\gamma_{\vec{m},\vec{q}}(\kappa\alpha) = u^a_{\kappa,\alpha} = \sum_{b,\kappa',\beta}\frac{C_{\kappa\alpha,\kappa'\beta}}{\sqrt{M_\kappa M_{\kappa'}}}e^{i\vec{q}\vec{R}_b}\gamma_{\vec{m},\vec{q}}(\kappa'\beta) = \sum_{\kappa',\beta}D_{\kappa\alpha,\kappa'\beta}\gamma_{\vec{m},\vec{q}}(\kappa'\beta). \qquad (2.47)$$

The so-called dynamical matrix $D_{\kappa\alpha,\kappa'\beta}$ in (2.47) is just the lattice Fourier transform of the real space force constant matrix $C_{\kappa\alpha,\kappa'\beta}$. In practice the force constant matrix is deduced from the Hellman-Feynman forces acting on displaced atoms in first principles calculations which we obtain from VASP. Solving equation (2.47) on a ***q***-vector grid in the momentum space provides the vibrational spectra of the system. This description is sufficient in the covalently bonded crystal. However, if ionic interactions are present the long-range nature of the Coulomb interaction between distant neighbors must be taken into account. Following the derivation of Maradudin [82] this long-range correction has the form

$$\vec{D}^{\text{long}}_{\alpha\beta}(\vec{k};\mu,\nu) = \frac{e^2}{V\varepsilon_0\varepsilon_\infty}\frac{\left[\vec{k}\vec{\vec{Z}}^*(\mu)\right]_\alpha\left[\vec{k}\vec{\vec{Z}}^*(\nu)\right]_\beta}{\left|\vec{k}\right|^2}\times\exp\left(-\frac{\left|\vec{k}\right|^2}{\rho^2}\right). \qquad (2.48)$$

where the $\vec{\vec{Z}}^*(\nu)$ are Born effective charge tensors of atom ν, V the volume of the primitive cell, and ε_∞ the high frequency dielectric constant. The parameter ρ controls the range of the long-range correction. The long-range contribution only affects phonon modes close to the Γ-point, and the Born effective charge tensors introduce a directional dependency in the phonon modes. The total dynamical matrix is now the sum of (2.47) and (2.48). The long-range correction can lead to Lyddane-Sachs-Teller (LST) shifts in the frequency of optical phonons close to Γ as the symmetry of some of the transversal and longitudinal atomic excitations breaks in the ionic crystal. In the simple cubic structure the LST frequency shifts are given by [82]

$$\frac{\omega^2_{LO}}{\omega^2_{TO}} = \frac{\varepsilon_o}{\varepsilon_\infty}. \qquad (2.49)$$

The vibrational spectrum can further be used to define other thermodynamic properties of materials such as the vibrational free energy [82]:

$$F_{vib} = rk_B T \int_0^\infty g(\omega) \ln\left[2\sinh\left(\frac{\hbar\omega}{2k_B T} \right) \right] d\omega, \tag{2.50}$$

where r is the number of degrees of freedom, and $g(\omega)$ is the phonon density of states. From this the heat capacity is given by:

$$C_v = \frac{1}{4k_B T^2} \int_0^\infty g(\omega) \frac{\hbar^2 \omega^2}{\sinh^2\left(\frac{\hbar\omega}{2k_B T} \right)} d\omega. \tag{2.51}$$

We will use the vibrational free energy as one possible way to calculate the transition temperature of HA, and compare our theoretical heat capacity with experimental data.

2.5 SURFACE AND INTERFACE ENERGETICS FROM FIRST PRINCIPLES

Surface and interface energetics are important, for example when trying to identify structures appearing in experiment, or calculate wetting behavior of one material on another. While it is rather simple to compute both surface and interface energy from first principles when only having one (surface calculation) or two (interface calculation) atomic species in the system, it becomes rather in-transparent when dealing with multicomponent materials. The complication arises from the fact that the surface termination may be such that the bulk beneath the surfaces does not contain an integer number of the material's primitive cell which makes the choice of reference energy complicated. In that case the method of choice to calculate surface energy is to use the Gibbs free energy approach [83]. The surface energy of a substrate is then given by

$$\sigma = \left[E_{slab} - \sum_i N_i \mu_i \right] / 2A. \tag{2.52}$$

E_{slab} is the total energy of the substrate calculated from first principles in slab geometry (*i.e.* the cell configuration is of the form substrate/vacuum), and μ_i and N_i are the chemical potential and number of particles of the *i*-th element in the slab. *A* is the surface area of the slab. The factor 2 in the denominator arises from the fact that due to the periodicity of the system two rather than one surfaces face the vacuum. Thermodynamic equilibrium of the surface with the bulk material imposes the following condition on the chemical potentials:

$$\sum_i N_i \mu_i = \mu_{bulk}. \tag{2.53}$$

The sum runs over the atomic species in the primitive cell from which the slab is built. The N_i are the number of atoms *i* in the primitive cell. μ_{bulk} is the bulk energy of the primitive cell calculated from first principles. When rewriting the chemical potential to $\mu_i = \tilde{\mu}_i + \mu_{i,bulk}$, where $\mu_{i,bulk}$ is the bulk atomic energy of species *i*, equation (2.53) becomes:

$$\sum_i N_i \tilde{\mu}_i = -E_f\,, \tag{2.54}$$

where E_f is the formation energy of the bulk primitive cell with respect to the bulk atomic energies. The range of $\tilde{\mu}_i$ is

$$-E_f < \tilde{\mu}_i < 0\,, \tag{2.55}$$

for the species *i*.

Equation (2.52) can now be rewritten to

$$\sigma = \left[E_{slab} - \sum_i N_i \left(\tilde{\mu}_i + \mu_{i,bulk} \right) \right] / 2A. \tag{2.56}$$

Condition (2.54) can be used to eliminate one of the $\tilde{\mu}_i$ variables in (2.56). Nevertheless, for an increasing number of atomic species in the slab equation (2.56) becomes

increasingly more complicated to display and typically needs to be evaluated in limiting cases (*i.e.* some of the $\tilde{\mu}_i$ are fixed to a specific value).

The approach to calculate interface energy is equivalent, thus the same issues arise. However, when only being concerned whether a layer of another material deposited on the substrate is able to wet the substrate, I propose an alternative approach. Consider the simulation cell in an interface calculation to be of the form vacuum/layer/substrate/layer/vacuum. The interface energy is given by:

$$2A\sigma_i = E_{tot} - E_{sub}^{bulk} - 2E_{layer}^{bulk} - 2A\sigma_{layer}, \tag{2.57}$$

where σ_i is the interface energy, and σ_{layer} the surface energy of the deposited layer. E_{tot} is the total energy of the simulation cell, and E_{sub}^{bulk} and E_{layer}^{bulk} the energy of the substrate and the deposited layer, respectively. The substrate energy in (2.57) can be rewritten as:

$$E_{sub}^{bulk} = E_{sub}^{bulk} + 2A\sigma_{sub} - 2A\sigma_{sub} = E_{sub}^{surf} - 2A\sigma_{sub}, \tag{2.58}$$

where σ_{sub} is the substrate's surface energy. While E_{sub}^{bulk} can be difficult to calculate in case the substrate does not consist of an integer number of the primitive cell (approach would be similar as in the surface energy calculation), the energy E_{sub}^{surf} can be directly extracted as the total energy of the substrate's surface calculation. Restructuring equation (2.57) and using (2.58) we get:

$$\sigma_i + \sigma_{layer} - \sigma_{sub} = \left(E_{tot} - E_{sub}^{surf} - 2E_{layer}^{bulk}\right)/2A. \tag{2.59}$$

Comparing (2.59) with the wetting condition

$$\sigma_i + \sigma_{layer} - \sigma_{sub} < 0 \tag{2.60}$$

shows that equation (2.59) unambiguously determines the wetting behavior of a layer on the substrate. The term E_{layer}^{bulk} still needs to be evaluated with help of chemical potentials;

however, the total number of degrees of freedom is significantly reduced compared to also using chemical potentials to evaluate E_{sub}^{bulk} in equation (2.57). In our studies of the HA surface in Chapter 4 we mainly use equation (2.56). In Chapter 6 we will make use of equation (2.59) when studying the TiO_2/HA and the HA/H_2O interface.

2.6 WORK FUNCTIONS AND BAND ALIGNMENT AT INTERFACES FROM FIRST PRINCIPLES

Another important question from a materials science point of view is the work function of a material. The work function changes with both surface orientation and composition. In a complicated material such as HA the surface composition can vary strongly with cleavage, and thus the work function may span several eV. The work function is an easily accessible quantity in first principles calculations using slab geometry (*i.e.* a substrate/vacuum slab), where the substrate is approximately 15 Å thick, followed by ~10 Å vacuum. The electrostatic potential inside the slab as calculated from VASP saturates to a constant value in the vacuum region. By definition the work function of a material is the energy difference between the highest occupied energy (Fermi level) in the substrate and the vacuum energy, and thus can be directly extracted from the electrostatic potential in a slab calculation.

While it is relatively simple to calculate the band structure of two materials, their band alignment at the interface is somewhat more complicated. Both materials have to be calculated within the same cell in order to guarantee the same point of reference in their energy levels, and to take interface dipole creation into account. This can be achieved in a superlattice structure. The two material layers have to be thick enough to ensure adequate separation between adjacent interfaces (due to periodic boundary conditions). Depending on the materials several scenarios are possible. Here, I limit the discussion to the case

where the substrate has an energy gap between the highest occupied energy level (valence band top) and the lowest unoccupied energy level (conduction band bottom), and the deposited top layer material is metallic (see schematic in Fig. 2.4). The characteristic quantity in the band alignment is the Schottky barrier height (p-type Schottky barrier height φ_p in Fig. 2.4). It is evaluated as follows. Deep inside the substrate the electrostatic potential (and thus the band structure) mimics that of the bulk phase of the substrate bulk. Thus, the top of the valence band and the bottom of the conduction band with respect to the electrostatic potential in the bulk phase calculation can be placed in the supercell calculation with respect to the electrostatic potential deep inside the substrate. The Schottky barrier height is then taken to be the difference between the supercell's Fermi energy and the top of the valence band of the insulator.

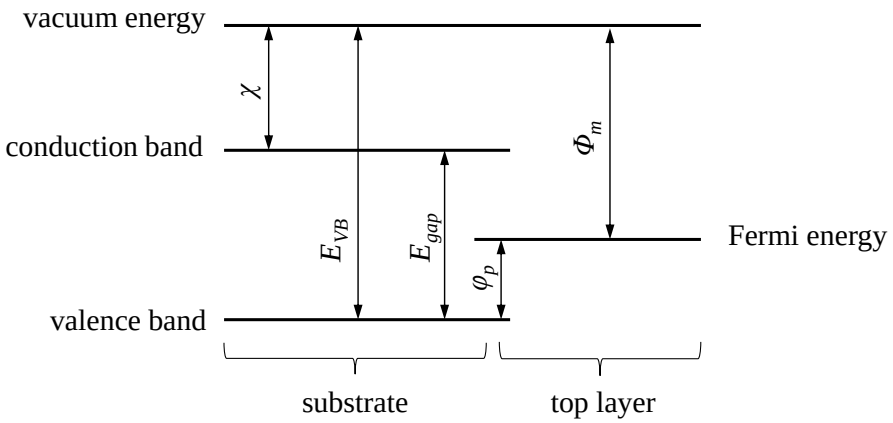

Fig. 2.4: Schematic of a band alignment at the insulator/metal interface. χ is the semiconductor's electron affinity, E_{gap} its energy gap between the top of the valence band and the bottom of the conduction band, and Φ_m is the metal's work function. The p-type Schottky barrier φ_p is the energy difference between the Fermi level of the combined system and the top of the valence band.

2.7 VAN DER WAALS INTERACTIONS IN DFT

Treating the long-range correlations (dispersion forces) adequately is a notorious short-coming of present DFT local and semi-local exchange-correlation functionals [84]. The net attractive interaction of the long-range correlations originates from the response of electrons in one region of a crystal to a sporadic charge density fluctuation in another region. Naturally, the effects of missing the dispersion forces are only noticeable when handling organic hydrogen-bonded molecules and their interactions. HA does include hydrogen bonds in between two neighboring OH pairs, however, their effect is negligible compared to the rest of the interactions in the crystal. Nevertheless, when simulating H_2O on the HA surface one needs to be more careful. For hydrogen-bonded systems it was proposed [*i.e.* by 85] to modify current DFT methods in order to take into account long-range interactions separately as function of the polarizability of the material. Mathematically, that results in adding correction terms ΔE to the total energy in the form of a multipole expansion [86,87]:

$$\Delta E = -\sum_{m=3} \frac{C_{2m}^{AB}}{R^{2m}}, \tag{2.61}$$

with the expansion coefficients

$$C_{2m}^{AB} = \sum_{l=1}^{m-2} \frac{(2m-2)!}{2\pi(2l)!(2m-2l-2)!} \times \int_0^\infty d\omega \; \alpha_l^A(i\omega)\alpha_{m-l-1}^B(i\omega). \tag{2.62}$$

The correction term in (2.61) is per pair of atoms A and B. In (2.62) the α_l^A are dynamic 2^l-pole electric polarizability of atom A. Equation (2.62) reduces the problem of long-range corrections to knowing these polarizabilities accurately. In the long-range the R^6-term dominates the expansion (2.61) describing the characteristic van der Waals interaction at long distance, thus most work only focuses on calculating the C_6 expansion coefficient. The correction terms (2.61) do not only shift the total energy of the system

statically, but take effect on the relaxation of the system through the interatomic distances R, thus leading to a different electronic ground state.

Michaelides *et al.* characterized the *ab-initio* attempts made to date to correct for the missing long-range correlation by their sophistication and in terms of their accuracy in a so-called "stairway to functional heaven" scheme (Fig. 2.5) [88]. An accurate description of all methods goes beyond the scope of this dissertation, and I will mainly focus on their general ideas, and refer the interested reader to Klimes' work [88] and the references made therein and in the following.

The "step one" methods described in Fig. 2.5 consist of simply adding a correction term to the DFT total energy:

$$E_{tot} = E_{DFT} + E_{disp} = E_{DFT} - \sum_{A,B} \frac{C_6^{AB}}{r_{AB}^6}. \tag{2.63}$$

The sum runs over pairs of atoms A and B. The advantage of this method lies in its simplicity. The C_6^{AB} coefficients are typically extracted from atomistic data. However, they are kept constant during a calculation. This short-coming is dealt with in the "step two" methods (DFT-D3, vdW(TS), BJ model, [89,90,91,92,93,94,95]). There, the dispersion coefficient of an atom in a molecule depends on the effective volume of the atom. The electron cloud of a "squeezed" atom is less polarizable, and the C_6^{AB} coefficient decreases. This change is simply interpolated from tabulated atomic polarizabilities as function of volume. A yet higher degree of sophistication can be achieved by also quantifying the XC-hole dipole moment which is dealt with by the work of Becke [91]. On the next level (vdW-DF) no external atomistic data is used anymore but the dispersion interaction is extracted from the electron density which in turn is calculated using non-local correlation functionals [96]. The advantage of this approach is that correlations of all ranges are included in the DFT total energy. Also importantly, the

computational cost is comparable to GGA calculations. However, the vdW-DF tends to overestimate the long range dispersion interactions, the error in the C_6^{AB} coefficients can reach up to 30 % [97]. All these previous methods suffer of a major short-coming by not taking into account the medium separating the interacting atoms or molecules [98]. Several methods have been developed to account for that issue. For example the Many-Body Dispersion (MBD) method where the many-body dispersion interaction is approximated in a model of coupled dipoles [99]. The atom-centered dipoles are represented as quantum harmonic oscillators with characteristic frequency. When turning on the interaction between the dipoles this frequency shifts yielding the dispersion interaction. Another approach receiving recent attention in the context of vdW interaction in DFT is the random phase approximation (RPA) [100-102]. While being successfully used for solids and molecules [103,104] it suffers of high computational cost. Besides the mentioned methods a variety of other approaches have been receiving some attention recently [*e.g.* 105,106]. I would like to refer the interested reader to these references.

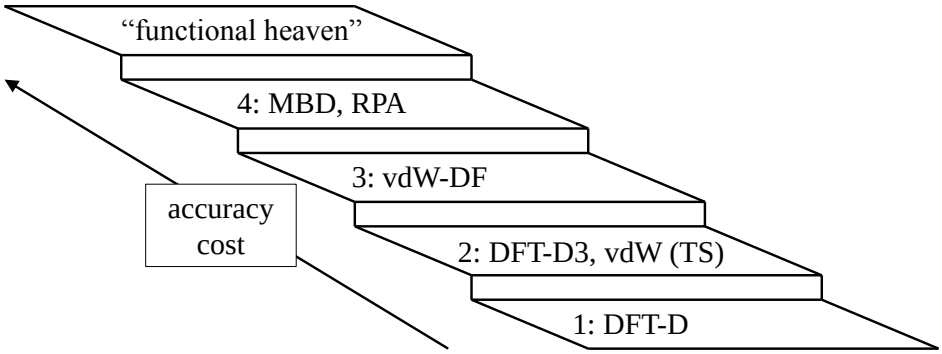

Fig. 2.5: "Stairway to heaven" describing the step by step improvement in correcting functionals for dispersion interactions.

3. First principles study of the biomineral hydroxyapatite

The results of this Chapter have been published in the Physical Review: A. Slepko, A. A. Demkov, Phys. Rev. B **84**, 134108 (2011).

3.1 INTRODUCTION

A carbonated form of hydroxyapatite [$Ca_{10}(PO_4)_6(OH)_2$] is one of the most abundant materials in mammal bone [107]. It crystallizes within the free space between tropocollagen protein chains (Fig. 3.1) and strengthens the bone tissue. The mineral content of a typical human bone increases with age and reaches a maximum value in males and females at different ages [2]. From this peak value the mineral content starts to decrease leading to diseases such as e.g., osteomalacia (softening of the bone caused by the loss of bone mineral). Some of the emergent applications of hydroxyapatite are, therefore, bone repair and replacement, and production of synthetic bone material [108]. Although by itself HA is too brittle to be used as a bone replacement directly, a variety of coating techniques have been developed in recent years to combine the strength of metals (such as titanium) with the natural bio-activity of HA [3]. The key property besides the bio-activity is therefore the HA adhesion to metals. The adhesion is governed by chemical bonding and thus the problem is that of the electronic properties of the interface. Therefore, a thorough understanding of the electronic and mechanical properties of HA, its surface and interfaces to other substrates are of scientific interest.

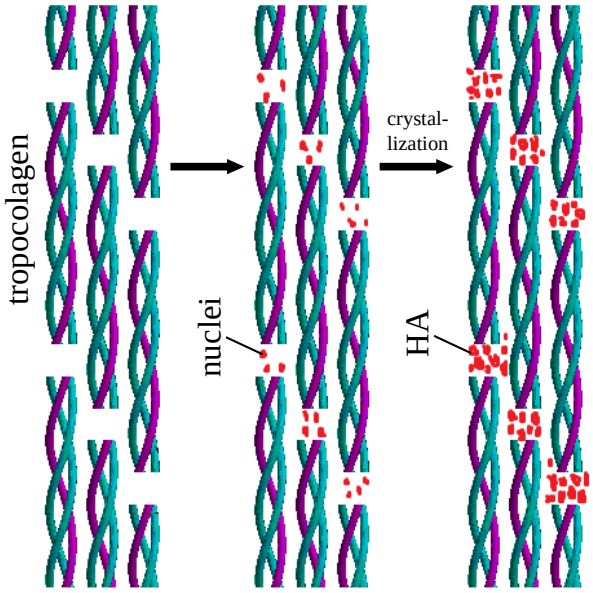

Fig. 3.1: Schematic of the HA crystallization during bone formation. Experiments suggest that the c-axes of both the tropocollagen and HA platelets are aligned [30]. The formation of bone tissue happens in several steps. After the tropocollagen helices are aligned, constituents of the HA crystal accumulate in the spaces between the tropocollagen and crystallize in the (001) orientation. The final HA mineral within the spaces consists of

A significant amount of experimental work on HA has been done, and in particular in the medical implant field, for an excellent review of this work we refer the interested reader to ref. [3]. Some of the first experimental reports of HA date back to 1936 [4]. In his work on dental enamel, Schmidt demonstrated that the crystallographic c-axes of the HA platelets within the collagen framework are well aligned with the collagen fibrils (Fig. 3.1). The hexagonal crystal structure of HA with $P6_3/m$ symmetry (*#176 in the International X-Ray Tables*, Fig. 3.2) and the atomic positions were determined in 1958 by Posner *et al.* using the X-ray diffraction [5]. In 1964 Kay and co-workers refined the positions of the OH molecules using neutron diffraction [6]. Studies of the alignment of

tropocollagen chains in mammal bone and alignment and growth of HA crystals were done by Weiner and co-workers [13]. In the 1970s [48] Carlisle showed that doping (in that study with Si) can play an important role in supporting the bone growth. A monoclinic variant of HA was suggested in 1967 by Young [7]. He inferred that a HA crystal sufficiently free of impurities and vacancies could crystallize in the monoclinic phase analogous to the known monoclinic chlorapatite. Prior to this work it was believed that HA only appeared in a hexagonal structure. Recently, the monoclinic variant of hydroxyapatite attracted significant interest [*e.g.* 9,10].

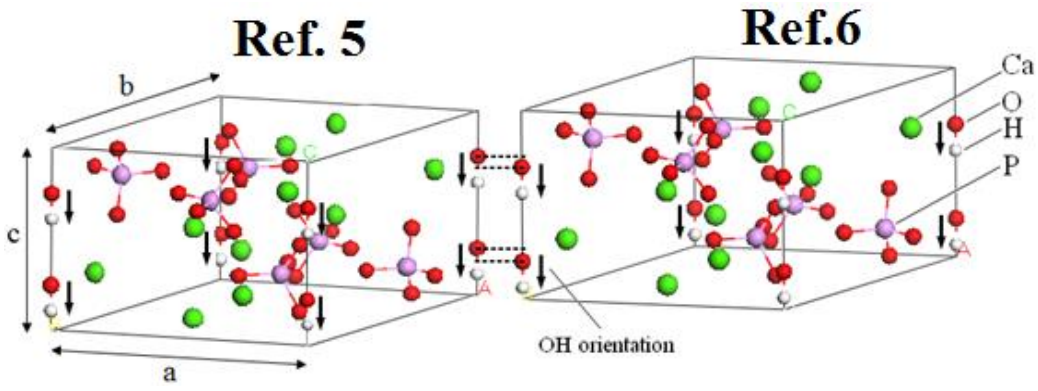

Fig. 3.2: HA primitive cells as described in references 5 and 6. The cell dimensions are a=b=9.432Å, c=6.881Å. The main difference between the two structures is the location of the oxygen atoms from the OH pairs as indicated in the figure. Following our notation (see text) we call the shown orientation of the OH pairs the (↓↓) orientation.

From the theoretical point of view the HA crystal presents an interesting challenge due to its complexity and importance in biological and biophysical systems. Only with the recent increase in computational power a theoretical study on HA became feasible, and of late along with other calcium apatites HA has been subject to a number of first principles calculations. De Leeuw, using density functional theory (DFT), analyzed the HA crystal structure and specifically the position and orientation of hydroxyl molecules [23]. She suggests that the experimentally found OH disorder in the crystal is due to locally ordered domains with differently oriented OH molecules. In the simplest case, this is achieved in a monoclinic cell. Later, using DFT Calderin *et al.* [24] have analyzed the crystal structure and electronic density of states of stoichiometric and OH-deficient HA as well a variety of other calcium apatites. They found that monoclinic and hexagonal HA are very close in energy indicating no particular preference for crystallization in a specific structure. They also found that apatites permit exchanging the OH molecules with other anions. The electronic structure has been confirmed by Rulis and co-workers using the orthogonalized linear combination of atomic orbitals method [28]. More recently, studies have focused on altering the electronic and chemical properties of HA with doping. For example, Chappell and Bristowe have studied the influence of substituting phosphorus with silicon on the HA crystal and electronic structure [38]. Silicon incorporation is found to be energetically most favorable in combination with removing one of the two negatively charged OH pairs in the primitive cell to maintain the overall charge neutrality (the ionic charge of SiO_4 is -4 vs. -3 of a PO_4 unit). Other recent theoretical studies of doping include the substitution of OH by fluorine [34] (making the crystal a mixture of HA and flourapatite (FA)), introduction of carbonate ion (CO_3^{2-}) to study physiologically found carbonated form of HA [34], and calcium substitution by titanium [39] and strontium [40] to induce structural modifications. Using a classical shell-model Calderin

at al. investigated the lattice dynamics, calculated thermal factors and simulated the infrared spectra of HA [29]. They find good agreement with experiment for the low-frequency and high-frequency vibrational modes at the Γ-point, whereas in the intermediate frequency range the reported agreement is poor. More recently, classical and quantum-mechanical molecular dynamics simulations have been used to study preferred surface orientations and terminations of HA [27,32,34] and to study the water and amino acid adsorption on the HA surface [27,34,41,46,47].

Despite the recent progress, many questions remain. Little is known, for example about the transformation mechanisms between the hexagonal and monoclinic phases. The mechanical properties of HA remain virtually unstudied. HA is still a challenging subject for first principles calculations due to a large number of atoms in the unit cells and variation in nature of interatomic bonding. In this paper, using density functional theory we investigate both hexagonal and monoclinic forms of HA. We identify the monoclinic phase as the ground state and analyze possible pathways for the phase transition between the hexagonal and monoclinic phases. We carefully compare the electronic structure of both phases. For the hexagonal phase we calculate the phonon frequencies at the Γ-point and elastic constants. Both are in good agreement with available experiment.

3.2 COMPUTATIONAL DETAILS

All calculations are done using density functional theory as implemented in the VASP code [51-55]. We use the Perdew-Wang [109] (PW91) exchange correlation functional and projected augmented wave (PAW) pseudopotentials [110]. The valence configurations are $1s^1$ for hydrogen, $3s^2 3p^3$ for phosphorus, $4s^2$ for calcium and $2s^2 2p^4$ for oxygen. We use 700eV as the kinetic energy cut-off for bulk calculations. When

calculating the phonon frequencies we increase the energy cut-off to 950eV to obtain highly accurate forces. In all calculations - except for the elastic constant calculations - we allow for full relaxation of the cell including changing the volume, adjusting the atomic positions and cell shape. When calculating the elastic constants we only allow for the relaxation of ionic positions within the strained cells. Symmetry operations are switched off during relaxation. We use a 6×6×8 Monkhorst-Pack [111] k-point mesh for the Brillouin Zone (BZ) integration of hexagonal cells that ensures the convergence to 1.8meV/cell. For the monoclinic primitive cells we use 6×4×6 Monkhorst-Pack k-point meshes. All structures are relaxed until the largest force on atoms in the cell is smaller than 20meV/Å. When calculating the vibrational modes, we relax the atomic positions until the largest force is smaller than 0.2meV/Å.

3.3 RESULTS

3.3.1 Ground state crystal structure

To identify the theoretical ground state of HA we start from the experimental structure reported by Posner *et al.* and Kay and Young (as shown in Fig. 3.2) [5,6]. They report a hexagonal primitive cell of $P6_3/m$ symmetry (*#176 in the International X-Ray Tables*, Fig. 3.2) that contains ten Ca atoms, six phosphate (PO_4) groups and two hydroxyl (OH) molecules. In Fig. 3.3 we present a top view of the crystal. For pictorial purposes we shift the original primitive cell boundaries along the *a* and *b* axes in such a way that the OH column is now in the center of the cell. There are two types of Ca atoms in the cell. Ca atoms of one type are arranged in a hexagon around the OH molecules (Fig. 3.3). The darker and lighter color distinguishes two atomic planes. The darker balls are located at z=0.25c, and the lighter ones are at z=0.75c. The remaining four Ca atoms

are arranged in two columns at the corners of the cell in Fig 3.3. In the upper left column the two Ca_I atoms are located at z=0.999c and z=0.501c. In the lower right column the two remaining Ca_I atoms are located at z=0.499c and z=0.001c. Similarly to first type Ca, six phosphorus atoms of the PO_4 molecules are arranged in two triangles around the OH channel, three are at z=0.25c and three at z=0.75c. Again, the darker and lighter color in Fig. 3.3 distinguishes between the two planes. While most of the atomic coordinates reported in 6 and 7 are almost exactly the same, the two structures differ in the position of the OH molecules. In ref. 6 the exact positions of hydrogen atoms could not be determined and the oxygen atoms are said to be located within the symmetry related planes at 0.25c and 0.75c. The later work [6] specifies the positions of hydrogen atoms and suggests that oxygen of the OH is shifted by ~0.3Å along the c-axis with respect to the previously reported positions as indicated in Fig. 3.2. The OH groups bring a structural ambiguity: two OH molecules do not have an energetic preference whether to point the hydrogen atom ‘upwards’ or ‘downwards’ along the c-axis. This is accounted for by introducing 0.5 occupancies in both possible arrangements. To simplify our discussion we introduce a notation where arrows (↑) and (↓) correspond to the z-coordinate of the hydroxyl group oxygen being smaller and larger than the z-coordinate of hydrogen, respectively. The pair of hydroxyl groups per primitive cell is denoted by a pair of arrows. In the hexagonal primitive cell four different orientations (↑↑),(↑↓),(↓↑),(↓↓) are possible with (↑↑) and (↓↓) cells, and (↑↓) and (↓↑) cells being equivalent.

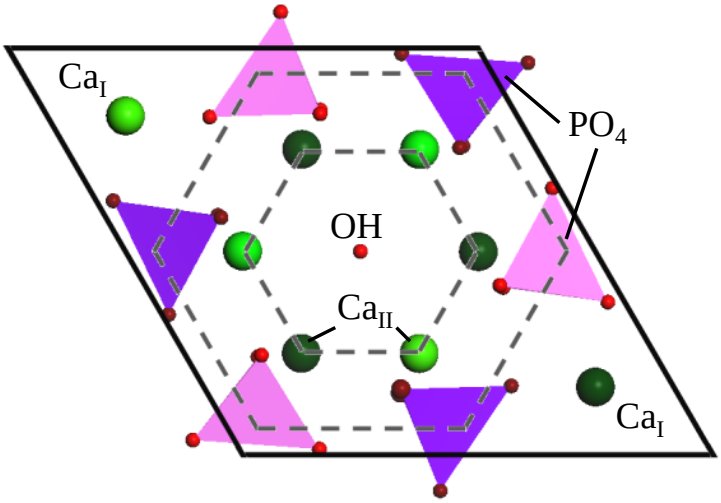

Fig. 3.3: Top-view on the hexagonal primitive cell. In the figure we shifted the original primitive cell in the x and y directions so that the OH column is in the center of the depicted cell. The darker colored Ca_{II} atoms and PO_4 molecules are centered at z=0.25c and the lighter ones are centered at z=0.75c. The OH column is surrounded by six Ca_{II} atoms and six PO_4 molecules. The Ca_I atoms are now in the corners of the cell. Below both of the two visible Ca_I atoms there is a second Ca_I atom at the distance 0.5c. Here, the lighter Ca_I atom is close to the top face and the darker Ca_I atom is at ~0.5c.

To identify the ground state we calculate the energy of both the (↓↓) and (↓↑) configurations. For later use, we also consider cells in which the hydroxyl molecules are slightly tilted away from the c-axis keeping the oxygen atoms on the c-axis and OH bond length fixed. These are indicated by (↘↙) if tilted from a (↓↓) configuration and by (↘↖) if tilted from a (↓↑) configuration. Additionally, we consider monoclinic cells created by doubling the hexagonal unit cell in the *b* direction. Here, each of the two contributing hexagonal cells is described by one pair of arrows for the OH-orientation, for example

(↓↓)(↓↓) or (↓↓)(↑↑) in the simplest cases. The (↓↓)(↓↓) configuration resembles a monoclinic cell which is reducible to a single hexagonal cell with a (↓↓) configuration. On the other hand, the (↓↓)(↑↑) configuration resembles a monoclinic cell that cannot be reduced further due to the alternating OH-orientation in subsequent OH columns.

The binding energies of all models are compared in Fig. 3.4. The top line in the graph indicates which reference the unrelaxed cell is based on and arrows indicate the OH-configuration before relaxation. The results per hexagonal cell are plotted in ascending energy order. The mixed configuration (↓↓)(↑↑) monoclinic structure suggested by Elliott [8], yields the lowest energy (structure 1) and is used as the reference energy. The lattice constants are a=9.53Å, b=2a and c=6.91Å. We find the second lowest energy for the hexagonal cell (structure 2) with the lattice constants a=b=9.53Å and c=6.91Å. The relaxed bond lengths of the hydroxyl and phosphate groups and bonding angles P-O-P of the phosphates in structure 2 are listed in Table 3.1. We find excellent agreement with experiment [5,6]. During the relaxation of structures 3 and 4 we find that the OH pairs realign with the c-axis ending up in structure 2. In structure 6 hydrogen atoms stay at the tilted positions during the relaxation yielding a binding energy which is ~269meV/cell higher than the hexagonal ground state structure 2. The (↓↑) type configurations where OH pairs flip within the same c-column are ~0.4eV higher in energy (per hexagonal cell) than the ground state making them unlikely. The energy difference between the monoclinic (structure 1) and hexagonal (structure 2) cells is only ~22meV per hexagonal cell suggesting that at room temperature HA can crystallize in a mixed phase with randomly distributed (↓↓) and (↑↑) domains. In the rest of the paper we will focus on these two structures.

Table 3.1: Comparison of fully relaxed theoretical bond lengths and bond angles in HA with experimental values.

	theory	**Exp. [ref. 6]**
P-O_I	1.56Å	1.54Å
P-O_{II}	1.57Å	1.55Å
P-O_{III}	1.55Å	1.53Å
O-H	0.977Å	0.957Å
O_I-P-O_{II}	111.1°	111.0 °
O_I-P-O_{III}	111.6°	111.5°
O_{II}-P-O_{III}	107.5°	107.5°

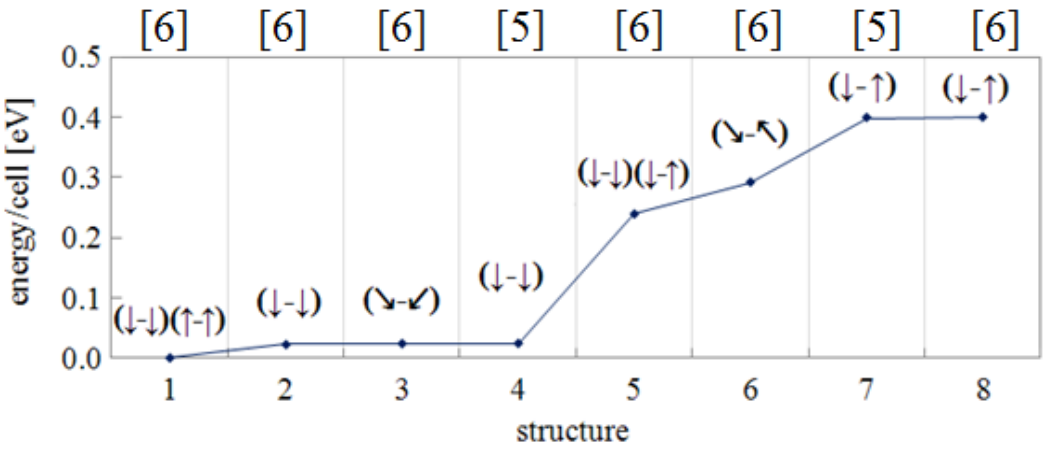

Fig. 3.4: The calculated structures are listed in ascending order according to the binding energy per single cell and the minimum energy is shifted to zero. We find the lowest binding energy for the monoclinic (↓↓)(↑↑) configuration followed by the hexagonal (↓↓) structure. The energy difference these two is ~22meV/cell. The binding energies of structures 2-4 are identical. Structures with flipped OH pairs within the same column generally yield higher binding energy.

3.3.2 Activation energy for the hexagonal to monoclinic transition

The monoclinic phase of HA was first described by Elliott *et al.* [8] who, following the work by Young [7], prepared a sample consisting of ~30% monoclinic HA and 70% hexagonal phases. They concluded that HA grown in a sufficiently clean experimental environment and having little impurities or vacancies can assume monoclinic symmetry under ambient conditions. Later, Hitmi *et al.* [25] found that while at ambient conditions both the hexagonal and monoclinic phases can occur. When heated above 470K HA always assumes the hexagonal structure, and the transformation is reversible. The overall structural similarity of the monoclinic and hexagonal phases and closeness of the calculated binding energy raise a question of the activation barrier and transition mechanism. To investigate theoretically possible pathways of the transition we use transition state theory and more specifically, the nudged elastic band method (NEBM) [76] as implemented in the VASP code.

We start by calculating the energy barrier between two equivalent hexagonal structures (↓↓) and (↑↑), using hexagonal structure 2 described in section A. We assume that changing the OH-configuration from (↓↓) to (↓↑) is unlikely as we have found the latter to be 0.4eV higher in energy than the former. The transformation involves not only the hydrogen displacement but also that of oxygen (Fig. 3.5), because the equilibrium positions of oxygen are shifted from the mirror planes at ¼ and ¾ containing Ca triangles. One possible pathway for the transition is to move the hydrogen atoms of the OH molecules along the z-axis. This requires breaking the OH-bonds and re-bonding hydrogen with the oxygen atom of the adjacent OH molecule (Fig. 3.5). Simultaneously, the oxygen atoms of the OH are moved in the opposite direction to their new equilibrium positions. Another possible mechanism is rotating each hydrogen atom around its bonding oxygen while simultaneously translating the oxygen to its new equilibrium

position. The rotation and translation of the hydrogen atom H_i from configuration (↓) to (↑) is described using spherical coordinates as:

$$\vec{r}_{H_i} = \vec{r}_{O(H_i)} + r_{O-H} \cdot \begin{pmatrix} \sin(\vartheta)\cos(\varphi_i) \\ \sin(\vartheta)\sin(\varphi_i) \\ \cos(\vartheta) \end{pmatrix}, \quad \vartheta = \pi, \ldots 0, \tag{3.1}$$

a)

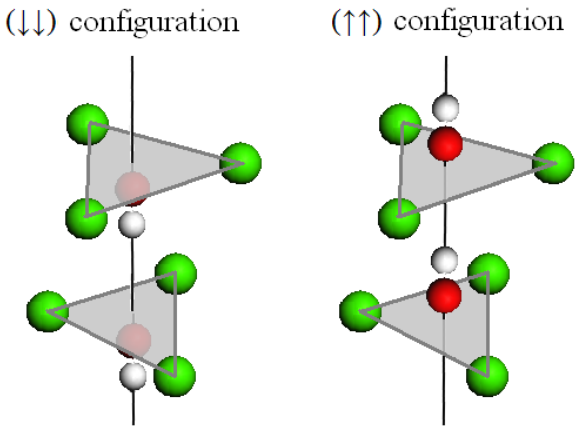

b)

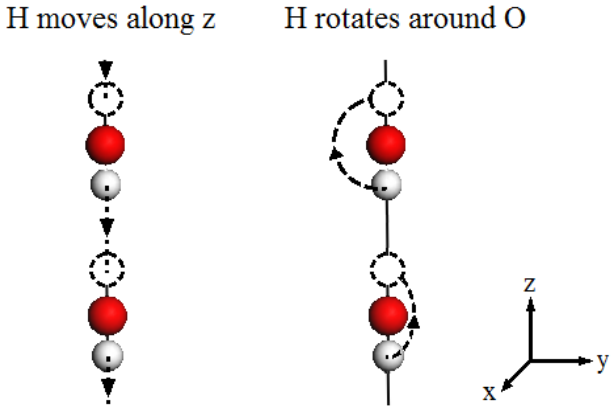

Fig. 3.5: a) OH positions with respect to the surrounding Ca_{II}-triangles.
b) Two transition paths for the hydrogen atoms to flip from (↓↓) to (↑↑).

Note that $\vec{r}_{O(H_i)}$ is not constant throughout the transition as the original oxygen atom has to move along the c-axis to its new equilibrium position. The $\vec{r}_{O(H_i)}$ and the angle ϑ are used to create the images for the NEBM to describe the transition pathway. The angle φ_i is given with respect to the $\vec{a}$ lattice vector and is chosen to move the H atoms in between two Ca atoms (Fig. 3.6). This yields two choices:

(i) Rotate hydrogen atom with angles $\varphi_1 = \pi/3$, $\varphi_2 = 4\pi/3$ and move the oxygen atom

(ii) Rotate hydrogen atom with angles $\varphi_1 = \pi/3$, $\varphi_2 = 2\pi/3$ and move the oxygen atom

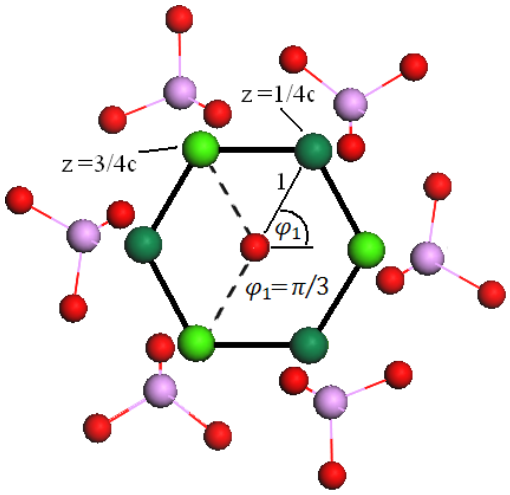

Fig. 3.6: Top-view along the OH column surrounded by Ca_{II} and PO_4. The dark Ca atoms are at z=1/4 and the light ones at z=3/4c. The OH pairs are in the center. There are three equivalent trajectories to flip the top OH-pair rotationally. One of them is indicated by projection 1. Once path 1 is selected there are 2 inequivalent ways to flip the bottom OH-pair as indicated by the dashed lines.

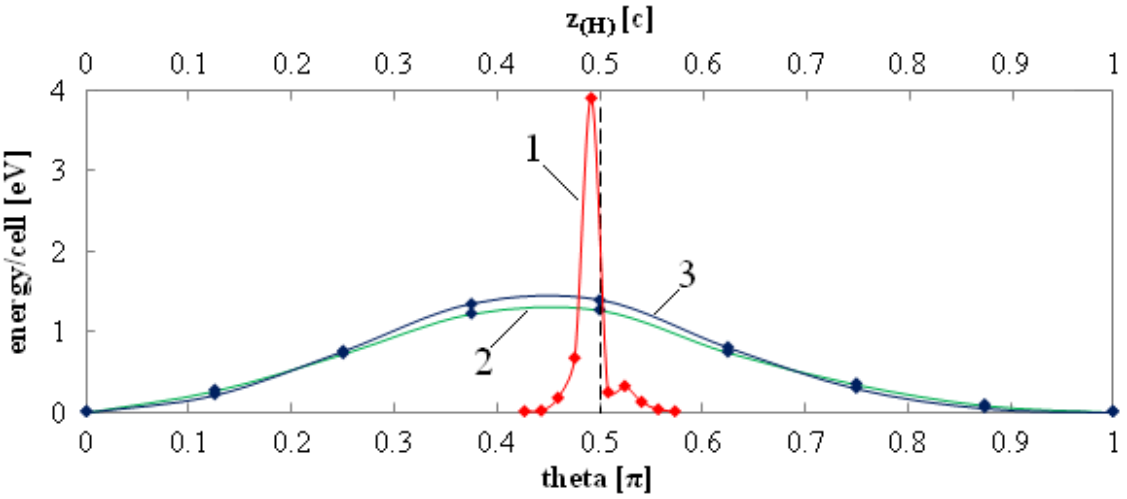

Fig. 3.7*:* The energy barriers corresponding to the translational (1) and rotational (2 and 3) hydrogen trajectories. The energy barrier for a translational displacement of the hydrogen atoms along the z-axis is approximately 3 times higher than that of the rotational transition.

Figure 3.5 illustrates the linear and rotational transformations, and Fig. 3.7 shows the calculated energy along these transition paths. The energy barriers are 3.5eV for the linear transition, and 1.3eV and 1.4eV in the rotational transitions (i) and (ii), respectively. These result in the activation energy per OH of 1.75eV, 0.65eV and 0.7eV for the linear and spherical transitions, respectively. The large difference in energy is not surprising as the first mechanism requires breaking the OH-bonds. On the other hand, in the rotational flip no bonds are broken. The barriers for two rotational transitions are very similar and close in energy. In what follows we only consider the rotational transformation of type (i).

Expanding the potential energy of the rotational transformation to second order around the minimum, we calculate the oscillation frequency of approximately 250cm^{-1}

corresponding to the period of $\tau \approx 134\,fs$. The average time after which a spontaneous flip from (↓↓) to (↑↑) occurs is therefore

$$t_{(\downarrow\downarrow)\to(\uparrow\uparrow)} = \tau \times N = \tau \times \exp\left(E_{B,0} / k_B T\right) \approx 162a, \tag{3.2}$$

at room temperature. In equation (3.2), N is the number of attempts needed to simultaneously flip both OH molecules per unit cell if each attempt has the probability of success of $p = \exp\left(-E_{B,0} / k_B T\right)$. We use $E_{B,0}$=1.3eV for the activation energy. The average transition time between the two equivalent hexagonal structures (↓↓) and (↑↑) is one hundred sixty two years at room temperature.

Now consider the monoclinic cell. Assuming that the OH molecules located along the neighboring columns do not interact, the energy barrier for rotational transitions in the monoclinic cell can be written as

$$\begin{aligned} &(\downarrow\downarrow)(\downarrow\downarrow) \to (\uparrow\uparrow)(\uparrow\uparrow): && E_B = 2E_{B,0} / 4 = E_{B,0} / 2 = 0.65\text{eV}. \\ &(\downarrow\downarrow)(\downarrow\downarrow) \to (\downarrow\downarrow)(\uparrow\uparrow): && E_B = E_{B,0} / 4 = 0.33\text{eV}. \end{aligned} \tag{3.3}$$

In equation (3.3) $E_{B,0}$ is the previously calculated energy barrier of 1.3eV in the hexagonal cell, and E_B is the activation energy per OH pair in the monoclinic cell. Transforming (↓↓)(↓↓) to (↑↑)(↑↑) requires the same energy per OH as flipping (↓↓) to (↑↑). However, the activation energy per OH to transform from (↓↓)(↓↓) to (↓↓)(↑↑) is reduced by a factor of two. The experimentally obtained range for the activation energy to change from hexagonal to monoclinic is 0.016-0.630 eV per OH and 0.84-0.89 eV per OH, reported by Hitmi and Nakamura [11,25], are in qualitative agreement with our results. Hitmi suspected a rotational transition, while Nakamura suspected a linear one explaining why the two ranges are so different. Using classical molecular dynamics Hochrein *et. al.* [26] find 0.52 eV per OH flip in good agreement with our results. Using

our calculated activation energy we write the probability of transformation from (↓↓)(↓↓) to (↓↓)(↑↑) as

$$p = \exp\left(-E_{B,0} / 2k_B T\right). \tag{3.4}$$

Using the same oscillation period as for the hexagonal cell the average time for the spontaneous hexagonal-monoclinic transition is estimated as

$$t_{(\downarrow\downarrow)(\downarrow\downarrow)\rightarrow(\downarrow\downarrow)(\uparrow\uparrow)} = \tau \times N = \tau \times \exp\left(E_{B,0} / 2k_B T\right) \approx 26ms, \tag{3.5}$$

at room temperature. The short transition time suggests that the hexagonal phase would always flip to the monoclinic phase under ambient conditions. Further investigation is needed to explain why the transition from the monoclinic to hexagonal phase occurs at 470K.

3.3.3 Electronic structure

The total electronic density of states (DOS) for both the hexagonal and monoclinic structures is shown in Fig. 3.8 a). For comparison we normalize the DOS to the hexagonal cell. The DOS of both structures are very similar, and the following description applies to both phases. Note that we distinguish between the oxygen atoms from the phosphate molecules ($O_{(P)}$) and oxygen atoms from the OH molecules ($O_{(H)}$). The states between -20eV and -17eV mainly consist of $O_{(P)}$, $O_{(H)}$ and phosphorous 2s and 3s states, respectively. At -17eV the hydrogen 1s states are mixed in. In an ideal PO_4 tetrahedron the phosphorus sp^3 hybridized orbitals form σ and π bonds with the surrounding oxygen. The σ-type electronic states appear in two peaks within the energy window -8eV to -4eV. In an ideal PO_4 tetrahedron these σ-states would be closer to each other in energy. However, in the HA crystal the PO_4 tetrahedron is slightly distorted from

a)

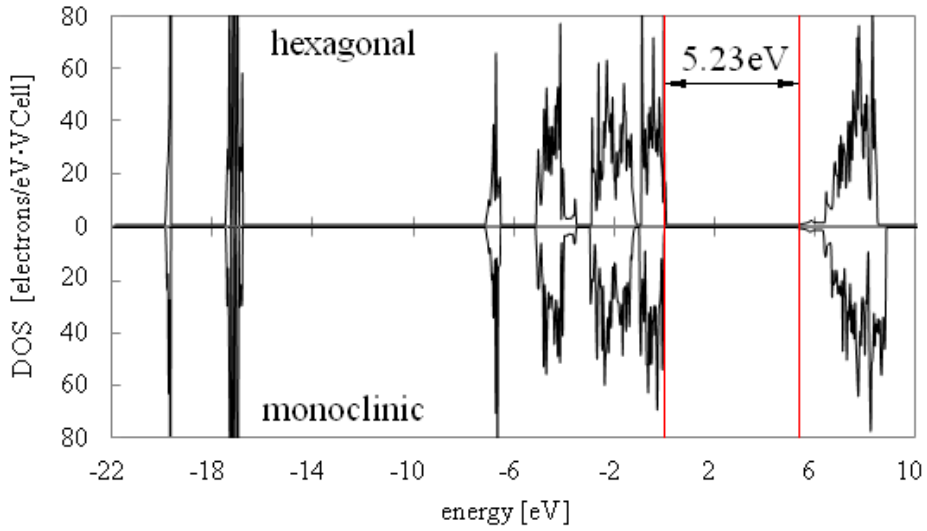

b)

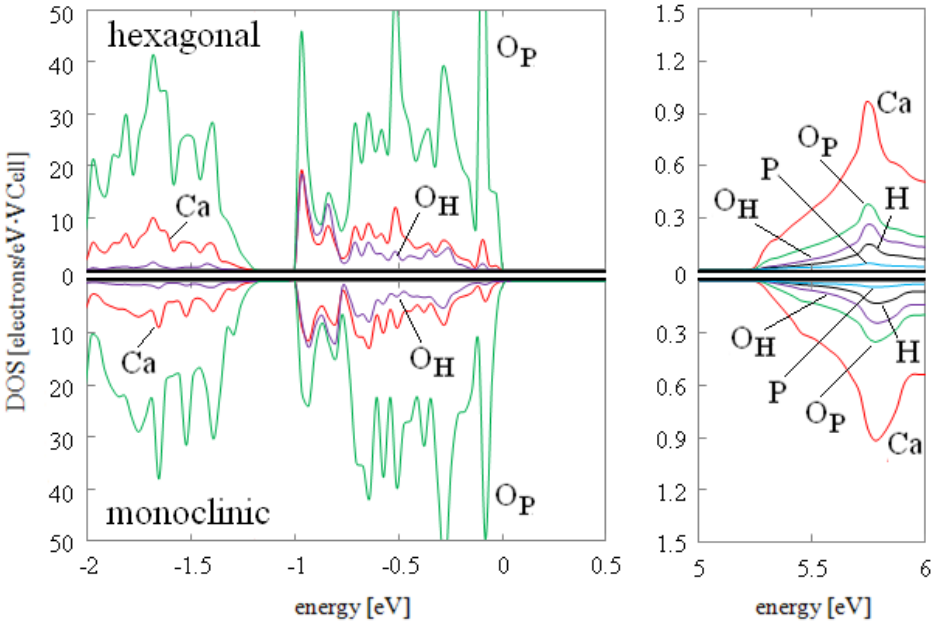

Fig. 3.8: The total DOS (a) and site-projected DOS in the near-gap region (b) of hexagonal and monoclinic HA. The DOS is normalized to a hexagonal cell. The Fermi level is at zero energy. The band gap is 5.23 eV.

the ideal 109.5° bonding angle leading to a split in the energy levels. We find the σ* electronic states in the conduction band between 6eV and 9eV. The remaining $O_{(P)}$ and $O_{(H)}$ p-states are the main contributors to the DOS between -3eV and the top of the valence band. Calcium 4s-states contribute mainly between -3eV and the top of the valence band at zero. In Fig. 3.8 b) we show the partial DOS projected on the different atomic species in the hexagonal and monoclinic cells in the near gap region. At the bottom of the conduction band the main contribution is from the s-like states of Ca atoms. The conduction band between 6eV and 8eV is almost entirely made up by unoccupied Ca states with *l*=2. In both crystals the GGA band gap is 5.23eV in good agreement with the previously reported LDA band gap of 5.40eV [24]. Thr reported experimental values of the band gap range from 3.95eV [112] to more than 6eV [113]. Our calculations suggest a large band gap considering that GGA underestimates the gap. Since the DOS of the hexagonal and monoclinic phase appear very similar, we only calculate the band structure for the smaller hexagonal cell. In Fig. 3.9 we show the calculated band structure along the high-symmetry directions in the Brillouin zone in the near gap region. First, we notice that HA is an indirect gap material. The valence band top shows little dispersion indicating heavy localized holes. We find two energy maxima in the valence band separated by only 8meV. The top of the valence band (shifted to 0eV) occurs along the Γ to K line. The bottom of the conduction band is at the Γ-point, and shows a free electron character with the anisotropic effective mass. Fitting the bottom of the conduction band at Γ to a second order polynomial we calculate the effective electron mass tensor

$$\left(m^*_{\alpha\beta}\right) = \hbar^2 \left[\frac{d^2E}{dk_\alpha dk_\beta}\right]^{-1} = \begin{pmatrix} 0.61 & -0.01 & -0.01 \\ -0.01 & 0.61 & -0.01 \\ -0.01 & -0.01 & 0.48 \end{pmatrix} \times m_e . \qquad (3.6)$$

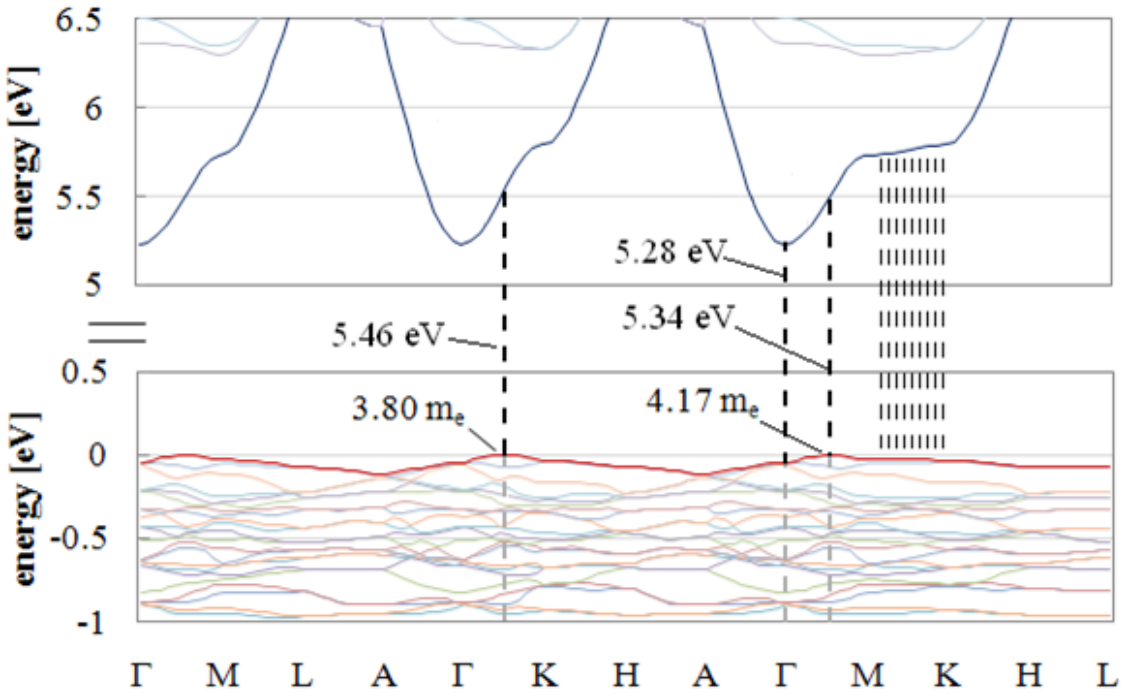

Fig. 3.9: The electronic band structure of hexagonal HA in the near gap region. The energy range in the gap region and is not shown for clarity. The band structure suggests that HA is an indirect band material. The lowest energy optical excitations are indicated. The dashed lines between M and K indicate nearly constant energy optical excitations.

The principal values are 0.48, 0.60 and 0.62 in units of the electron mass. The indirect band gap is 5.23 eV. The direct transitions at the top of the valence band and at the Γ point are at 5.46 eV and 5.28 eV, respectively. Another interesting feature is the flat region in both the valence and conduction bands along the M to K line. With the excitation energy of 5.75 eV this feature should noticeable in optical adsorption. Unfortunately, no experimental data is available. Our band structure is shown in Fig.

3.10. We notice slight differences when comparing it with the band structure calculated by Rulis *et. al.* [28]. The most notable one is the energy gap. Rulis calculates 4.5eV versus our 5.3eV. We attribute the discrepancy to a different basis (Rulis uses the linear combination of atomic orbitals). The overall band structure, and near parabolic dispersion at the bottom of the conduction band agree well with their results.

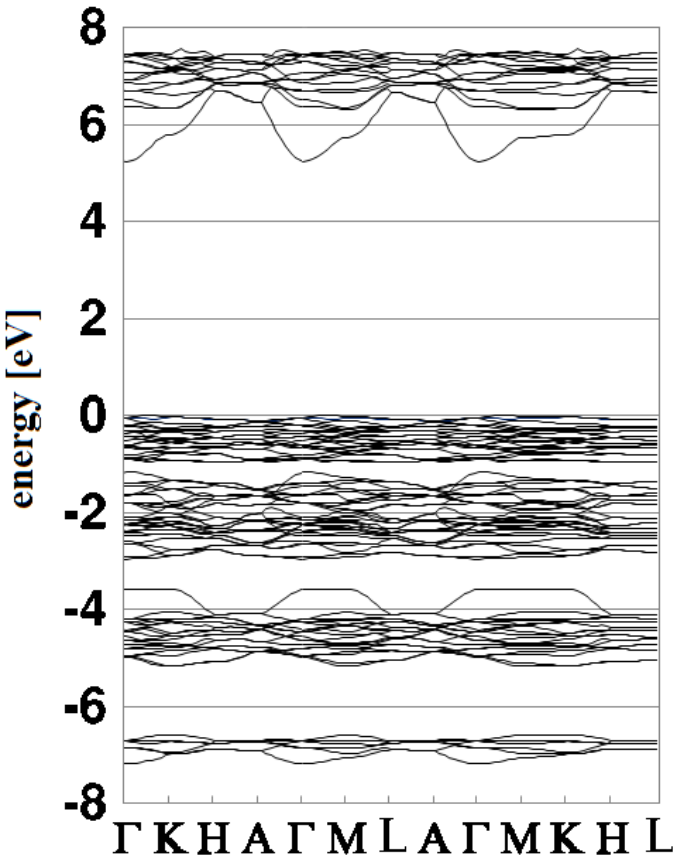

Fig. 3.10: The electronic band structure of hexagonal HA.

3.3.4 Phonon eigenmodes at the Γ-point

Experimental studies of hydroxyapatite vibrational properties remain scarce. The most recent papers are those of Fowler *et al.* [21] and Markovic *et al.* [22] reporting the infrared (IR) and Raman active vibrational modes, respectively. Theoretical studies of the HA vibrational spectra are quite difficult due to the crystal's complexity, and are typically limited to classical shell models [29]. However, the results strongly depend on the model potentials that have to be fitted to match the experimental data (a comparison of different sets of parameters is given by Calderin [29]). Therefore, a more general and transferrable approach of calculating the phonon spectrum is desirable. We use DFT to calculate the vibrational eigenmodes of hexagonal HA at the Γ-point. We analyze the influence of the ionic nature (long range Coulomb interactions) of the crystal on the eigenmodes and identify the vibrational modes mostly affected by the long range effects.

To calculate the short-range force constant matrix we take the numerical derivative of the Hellmann-Feynman forces with respect to small ionic displacements [*e.g.* 80]. The lattice Fourier transform of the force constant matrix yields the dynamical matrix [80,81]:

$$\vec{D}(\vec{k};\mu,\nu)=\frac{1}{\sqrt{M_\mu M_\nu}}\sum_m \vec{B}(0,\mu;m,\nu)\cdot\exp\left\{2\pi i\vec{k}\cdot\left[\vec{R}(0,\mu)-\vec{R}(m,\nu)\right]\right\}. \qquad (3.7)$$

The $\vec{R}(0,\mu)$ is the position of atom μ in the 0-th primitive cell within the supercell. $\vec{R}(m,\nu)$ is the position of atom ν in the m-th unit cell. $\vec{B}(0,\mu;m,\nu)$ are the force constants relating atoms $(0,\mu)$ and (m,ν). M_μ and M_ν are the masses of atoms ν and μ.

In 3-dimensional space the dimension of the dynamical matrix is 3N×3N, where N is the number of atoms in the primitive cell. Since we are interested in phonons at the Γ-point we only calculate the forces in a single hexagonal primitive cell. In covalent systems the range of interaction is assumed to be finite and the dynamical matrix can be directly calculated using the Hellmann-Feynman forces acting on the ions in the supercell when

displacing one atom from its equilibrium position. In the ionic system one has to worry about long-ranged dipole-dipole interactions. This is accomplished by adding a long-range correction to the dynamical matrix given by [80]

$$\vec{D}^{\,\mathrm{long}}_{\alpha\beta}\left(\vec{k};\mu,\nu\right)=\frac{e^2}{V\varepsilon_0\varepsilon_\infty}\frac{\left[\vec{k}\vec{\vec{Z}}^{*}(\mu)\right]_\alpha\left[\vec{k}\vec{\vec{Z}}^{*}(\nu)\right]_\beta}{\left|\vec{k}\right|^2}\times\exp\left(-\frac{\left|\vec{k}\right|^2}{\rho^2}\right), \tag{3.8}$$

here we use SI units. $\vec{\vec{Z}}^{*}(\mu)$ is the Born effective charge tensor of atom μ, and V is the volume of the primitive cell. The long-range contribution only affects the phonon modes close to the Γ–point. The Born effective charge tensors introduce a directional dependence in equation (3.8). The total dynamical matrix is given by a sum of (3.7) and (3.8).

First, we calculate the phonon eigenmodes in HA at the Γ–point without the long-range correction. We use a single primitive hexagonal cell. There are 132 eigenmodes including Raman and IR active vibrations. We use our calculated eigenmodes to approximate the phonon density of states (PDOS) at the Γ–point given by

$$\frac{\#\text{ of Eigenmodes}}{\Delta f}=\sum_i\delta\left(f-f_i\right)\equiv N\left(f\right), \tag{3.9}$$

The DOS is a sum of delta-functions positioned at the calculated eigenmodes at each k-point. We represent these peaks by a Gaussian, and apply a Gauss broadening of σ = 15cm^{-1}. In Fig. 3.11 we compare our results with the DOS constructed using experimental IR and Raman active modes as reported by Fowler [21] and Markovic [22]. The calcium ions contribute predominantly to the low frequency modes. In the ranges from 350cm^{-1} to 650cm^{-1} and from 850cm^{-1} to 1100cm^{-1} mainly the PO_4 molecules contribute to the spectrum. The OH-modes are at 693cm^{-1} and 3660cm^{-1} corresponding to the OH's libration and stretching modes, respectively. Comparing with the experimental work we find good qualitative agreement. The frequencies corresponding to the phosphate

eigenmodes are underestimated by ~5-10 %. This is consistent with the observation that the theoretical PO bond length is 0.02-0.03 Å longer than the experimental value. On the other hand, theoretical eigenmodes of the OH groups at 693 cm^{-1} (libration mode in x and y directions) and 3660 cm^{-1} (OH stretching mode) are overestimated by ~5-10% compared with experiment.

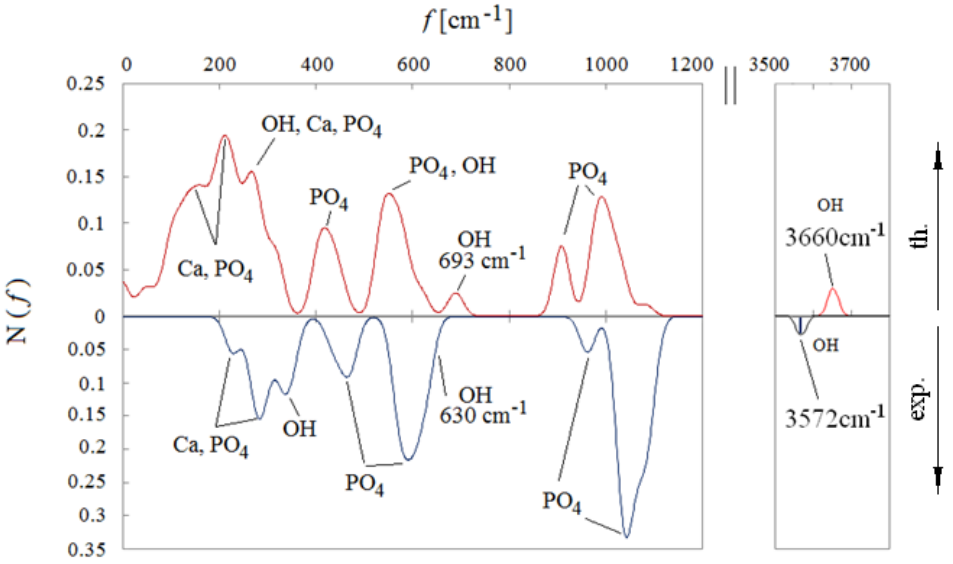

Fig. 3.11: The theoretical phonon density of states at the Γ-point compared with the experimental IR and Raman active modes. Our Ca and PO_4 peaks are underestimated by ~10 %, while the OH modes are overestimated by ~10 %.

Having found reasonable agreement with experiment without considering the long-range interactions, we now include the long-range correction (8). We approach the Γ point along the M to Γ, K to Γ and A to Γ directions. These directions correspond to approaching Γ from the face center, corner and top of the hexagonal Brillouin zone. Experimentally, the high frequency dielectric constant is sensitive to the Ca/P ratio of the

crystal [*e.g.* 14]. The values for ε_∞ in the literature for stoichiometric HA with the Ca/P ratio 1.67 vary between ε_∞=5 and ε_∞=20 [14,15,16,17,18]. This is in part to the variation in porosity, and water content of the samples, and in part to too low a frequency of measurement. In this work we use ε_∞=5 and cross-check with ε_∞=7 to see the qualitative dependency of the eigenmodes on ε_∞. The calculated Born effective charge tensors are summarized in Table 3.2. For the Gaussian smearing in (8) we use ρ=0.02Å^{-2}. We plot our results in Fig. 3.12 a) along with the experimentally measured modes. We find that including the long-range correction has little effect on most of the vibration modes in good agreement with Calderin's work [29] where a shell-model was used to calculate the phonons when approaching the Γ-point from the (100) and the (001) direction. In Fig. 3.12 b) we show the difference between the long-range corrected spectrum and un-corrected spectrum below 1200cm^{-1} at the Γ-point. Positive Δf means the long-range corrected modes are higher in frequency. The frequency shifts are very similar when approaching along the (100) direction and the (110) direction (M to Γ and K to Γ) ranging from 1cm^{-1} to 25cm^{-1}. When approaching along the (001) direction (A to Γ) somewhat different eigenmodes shift compared to approaching along (100) and (110), and the peak at 318cm^{-1} virtually disappears. While in the modes between 97cm^{-1} and 318cm^{-1} all atoms in the cell are vibrating, the 318cm^{-1} mode is a pure OH libration mode in the x-y-plane. The remaining shifted modes close to 600cm^{-1} and around 1000cm^{-1} are pure PO_4 vibration modes. The change in frequency due to the long-range correction is most notable for the OH mode at 318cm^{-1} which moves up to 343cm^{-1} when approaching Γ from the M point. Using ε_∞=7 in the long-range correction, this OH mode moves up to 335cm^{-1}, being the only mode substantially affected by using ε_∞=5. Overall, we find good agreement between our phonon spectra and experimental results.

Table 3.2: Born effective charge tensors for the different atomic sites.

	Born effective charge
H	$\begin{pmatrix} 0.37 & -0.01 & 0 \\ 0.01 & 0.37 & 0 \\ 0 & 0 & 0.28 \end{pmatrix}$
P	$\begin{pmatrix} 3.17 & 0.04 & 0 \\ -0.01 & 3.17 & 0 \\ 0 & 0 & 3.08 \end{pmatrix}$
Ca_I	$\begin{pmatrix} 2.41 & -0.08 & 0 \\ 0.08 & 2.41 & 0 \\ 0 & 0 & 2.51 \end{pmatrix}$
Ca_{II}	$\begin{pmatrix} 2.45 & 0.02 & 0 \\ -0.01 & 2.45 & 0 \\ 0 & 0 & 2.46 \end{pmatrix}$
O_I	$\begin{pmatrix} -1.93 & 0.03 & 0 \\ -0.02 & -1.93 & 0 \\ 0 & 0 & -1.41 \end{pmatrix}$
O_{II}	$\begin{pmatrix} -1.92 & 0 & 0 \\ 0 & -1.91 & 0 \\ 0 & 0 & -1.30 \end{pmatrix}$
O_{III}	$\begin{pmatrix} -1.47 & -0.02 & 0 \\ 0.02 & -1.47 & 0 \\ 0 & 0 & -2.13 \end{pmatrix}$
O_H	$\begin{pmatrix} -1.71 & 0.04 & 0 \\ -0.04 & -1.71 & 0 \\ 0 & 0 & -0.94 \end{pmatrix}$

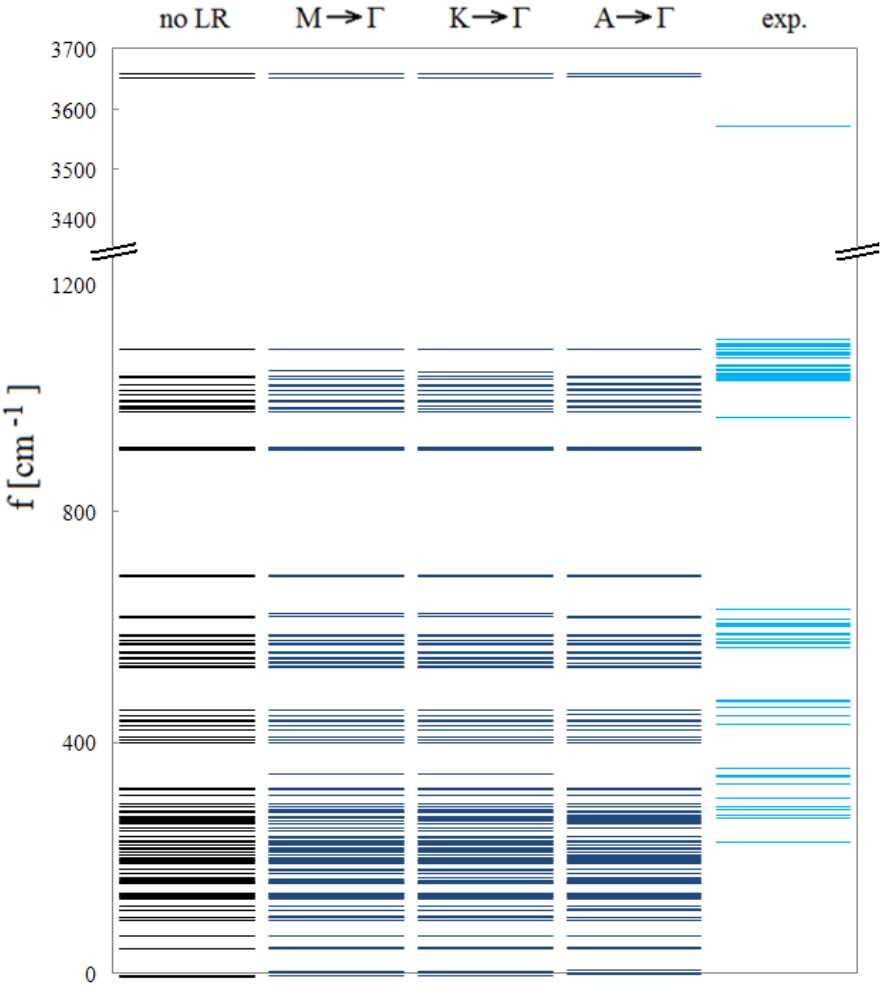

Fig. 3.12 a): The phonon frequencies at the Γ-point with and without the long-range correction. When applying the long-range correction we consider approaching the Γ-point from the M-point, the K-point and the A-point, corresponding to the directions (100), (110) and (001). We use the experimental values from Fowler and Markovic [21,22]. The direction of approach has little influence on the eigenmodes. The deviation from the experimental values is about 10%.

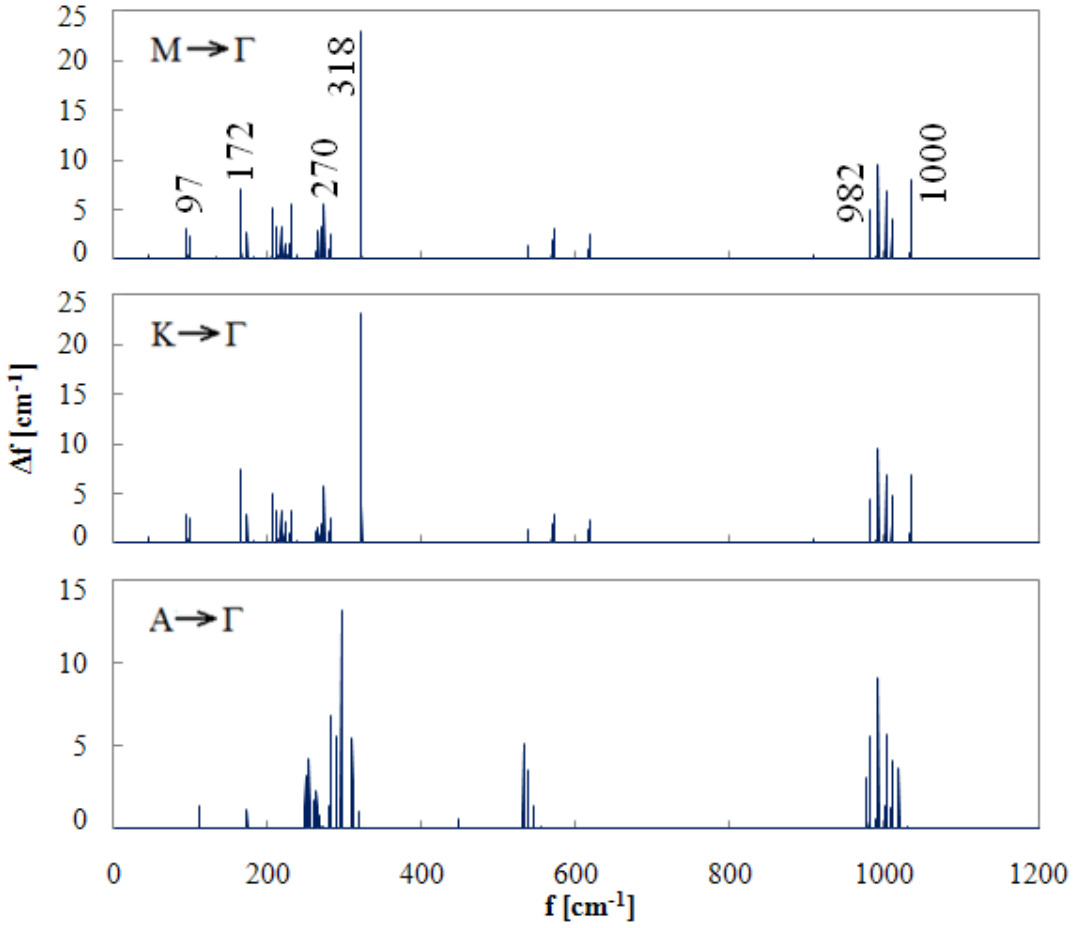

Fig. 3.12 b): The change in the phonon frequency when applying the long-range correction. We find almost identical changes when approaching along the (100) and the (110) direction (M to Γ and K to Γ, respectively). The largest change occurs for the mode at 318 cm^{-1} which corresponds to a pure OH libration mode. In the (001) direction (A→Γ) this mode is nearly unaffected by the long-range correction.

3.3.5 Elastic constants of HA

The anisotropy of the elastic properties of bones is governed by their main constituents, HA, the collagen chains and water. The theoretical determination of the elastic properties of composite materials is often done by averaging the elastic properties of the separate materials. Although, the quality of the results fluctuates depending on the material in question, upper and lower bounds of the effective moduli of composites can be found rigorously [114]. Previously, Katz and Ukraincik [115] calculated a set of pseudo-single crystal elastic constants extracted from the measured elastic constants of fluorapatite. The validity of such a calculation is somewhat justified by a strong similarity of the crystal structures of these two materials. Mustafa *et. al.* use a force field approach to obtain the elastic constants of HA [116]. Here, we calculate the elastic constants of hexagonal HA from first-principles.

Generally, the energy of a strained system can be written as a second order Taylor expansion in the distortion parameters $\alpha_{i,j}$:

$$E(V,\alpha) = E(V_0,0) + \frac{V_0}{2} \sum_{a,b,c,d} C_{abcd}\alpha_{ab}\alpha_{cd} \ . \tag{3.10}$$

The first order term drops out as the expansion is about the ground state. The second order term is described by the adiabatic elastic constants C_{abcd}. However, the C_{abcd} and α_{ab} are not all independent, and using the Voigt notation, equation (3.10) can be written as

$$E(V,\alpha) = E(V_0,0) + \frac{V_0}{2} \sum_{i,j} C_{ij}\alpha_i\xi_i\alpha_j\xi_j \ . \tag{3.11}$$

The introduced factors ξ_i account for the symmetry of the α's, $\alpha_{ab}=\alpha_{ba}$, i.e. for $b \neq a$ both α_{ab} and α_{ba} are labeled with the same Voigt index. Therefore, we get $\xi_i = 1$ if the Voigt index is 1, 2 or 3 and $\xi_i = 2$ if the Voigt index is 4, 5 or 6 [117].

There are five independent elastic constants in a hexagonal crystal: C_{11}, C_{12}, C_{13}, C_{33}, $C_{44}=C_{55}$. In order to determine these constants, five independent stresses must be applied

to the system (see appendix). Distortions (I), (III) and (V) keep hexagonal symmetry in the strained cell. Distortion (II) creates a monoclinic cell and distortion (IV) creates a cell with triclinic symmetry. Equation (2) is valid for small distortions. To have a measure of "small" we compare the volume changes after applying a specific distortion. Distortions (I) and (V) yield the largest change in volume. Thus, for (I) we use the parameters α = -0.01, -0.005, 0.00, 0.005, 0.01 and for (V) we apply α = -0.005, -0.0025, 0.00, 0.0025, 0.005. For distortions (II)-(IV) we use α = -0.02, -0.01, 0.00, 0.01, 0.02. These choices of α ensure that the change in volume relative to the equilibrium volume V_0 is smaller than 15Å^3 or ~2.8% of V_0. For all distortions we use a quadratic fit to extract the elastic constants C_{ij}. Our results are summarized in Table 3.3. For C_{11}, C_{33} and the bulk modulus B we find agreement within ~6% of the values previously reported by Katz and Mostafa [115,116]. Our C_{12}, C_{13} and C_{44} are within ~21% of Katz's and Mostafa's results indicating overall good qualitative agreement.

Table 3.3: Calculated elastic constants and bulk modulus compared to other theoretical calculations and corresponding experimental values. The bulk modulus is related to the elastic constants by the formula $B = \frac{2}{9}\left(C_{11} + C_{12} + 2C_{13} + C_{33}/2\right)$.

constant [10^{11} dyn/cm^2]	**this work**	**Ref. [116]**	**pseudo-exp. [115]**
C_{11}	12.90	15.75	13.70
C_{12}	3.70	5.74	4.25
C_{13}	6.70	5.97	5.49
C_{33}	17.30	14.73	17.20
C_{44}	4.40	4.39	3.96
B	8.60	9.07	8.90

3.4 CONCLUSIONS

Using density functional theory we find that the ground state of hydroxyapatite is monoclinic in agreement with previous calculations [23] and recent experiments [11,25]. The hexagonal phase is only 22 meV higher in energy than the monoclinic ground state. The structural transition path from the monoclinic to the hexagonal crystal phase and vice versa most likely involves the rotation of hydroxyl groups as suggested by Hitmi [25]. The activation energy for such a transition is 0.33eV per OH molecule and the transition time at room temperature is ~26ms. We find close similarity in the electronic structure of both phases suggesting similar chemical properties. For the hexagonal phase in agreement with previous theoretical results we find the indirect band gap 5.23eV. The bottom of the conduction band mainly consists of Ca s-states and shows free electron like behavior with the anisotropic mass at the Γ–point. Our results for the vibrational eigenmodes at the Γ point are within ±10% of available experiment [21,22], and calculated elastic constants agree well with the experimental results reported by Katz [115] and Mostafa [116].

3.5 APPENDIX

Following the approach described by Fast *et. al* [118], we use five independent distortions to obtain the elastic constants of the hexagonal cell. Their action on the crystal structure and symmetry are explained in the section 3.3.5. The small parameter α describes the deviation of the distorted crystal from the original one.

$$
\begin{aligned}
e_I &= \begin{pmatrix} 1+\alpha & 0 & 0 \\ 0 & 1+\alpha & 0 \\ 0 & 0 & 1 \end{pmatrix} \\
e_{II} &= \begin{pmatrix} 1+\alpha & 0 & 0 \\ 0 & 1-\alpha & 0 \\ 0 & 0 & 1 \end{pmatrix} \\
e_{III} &= \begin{pmatrix} 1 & 0 & 0 \\ 0 & 1 & 0 \\ 0 & 0 & 1+\alpha \end{pmatrix} \\
e_{IV} &= \begin{pmatrix} 1 & 0 & \alpha \\ 0 & 1 & 0 \\ \alpha & 0 & 1 \end{pmatrix} \\
e_V &= \begin{pmatrix} 1+\alpha & 0 & 0 \\ 0 & 1+\alpha & 0 \\ 0 & 0 & 1+\alpha \end{pmatrix}
\end{aligned}
\tag{3.12}
$$

4. First principles study of hydroxyapatite surface

The results of this Chapter have been submitted to Chemical Physics Review.

4.1 INTRODUCTION

Mammalian bone owes its remarkable strength and stability to hydroxyapatite $Ca_{10}(PO_4)_6(OH)_2$ (HA), that is its main mineral component [107]. HA crystallizes within the spaces between the tropocollagen chains forming bone's structure. This combination of HA and tropocollagen demonstrates impressive elastic properties [120]. An emergent application of HA is bone repair. Despite being biocompatible, due to its brittleness, HA does not meet the mechanical requirements of a bone replacement [121] and must in practice be reinforced with other materials such as titanium and its alloys [122], thus combining the metals' mechanical strength and HA's bio-compatibility. A promising approach is to deposit thin layers of HA on the implant's surface [123-129]. The compositional similarity of HA to bone tissue, results in bone growth over the implant's surface thus improving implant's adhesion to the bone [3]. Using a HA coating layer, is expected to significantly extend the lifespan of orthopedic and other implants [3]. The key element of this strategy is strong adhesion of HA to Ti surface, which typically involves a thin interlayer of TiO_2 [3]. Thus a better understanding of bonding at the HA/Ti and HA/TiO_2 interface at the microscopic level is necessary. Modeling oxide/oxide and oxide/metal interfaces with density functional theory has been very successful [130-135], therefore a detailed theoretical analysis of HA/Ti and HA/TiO_2 junction will be of significant interest. The salient feature of this problem is the complexity of HA's crystal structure and the lack of detailed materials characterization data. The large number of ways a HA surface can be prepared, presents a major difficulty

for such a study. Therefore, as a starting point, one may consider modeling the surface of HA first. Understanding the thermodynamics stability of the HA surface under the Ca, PO_4, or the OH rich environment, and the knowledge of the surface electronic structure will be useful in modeling and understanding of the complex interfaces involving HA. A similar strategy has been used in the case of the $SrTiO_3/LaAlO_3$ interface, where the surface analysis [136] has helped shedding light on the interface problem [137,138].

Current experimental studies of the HA surface are mostly concerned with analyzing the growth kinetics of the HA surface, ionic substitutions at the surface or the adsorption of water and small molecules on it [30-32,35,42-44,139]. Theoretically, both classical and quantum-mechanical molecular dynamics simulations have been used to calculate the surface energy [33,41], preferred surface orientation for interactions with small molecules [36,37,41,45,46] and ionic substitutions at the surface [36,37]. An excellent overview of the field is given in an article by Corno *et al.* [27]. Despite this effort, however, most theoretical studies investigate only a rather limited range of surface compositions while the complexity of the crystal structure allows for a variety of surface terminations even for the two most common (001) and (100) orientations.

In this paper, we present a comprehensive picture of the surface energetics. Using density functional theory, we investigate theoretically twenty nine surface structures with (001) and (100) orientations. We calculate the ground state surface phase diagram for various chemical environments. For the physiologically relevant OH-rich conditions we identify the most stable surface terminations and study their electronic properties. We calculate the work function of HA and establish its relation to the surface composition. The rest of the paper is organized as follows. First, we briefly summarize the computational methodology and the construction of the atomistic surface models used in this study in section II. Next, in section III we discuss the surface energy of HA under different

chemical conditions. We describe our calculations of the work function and compare theoretical results with the available photoemission data, and in section V we summarize our results.

4.2 COMPUTATIONAL DETAILS AND SURFACE MODELS

All calculations are done using density functional theory, as implemented in the VASP code [51-55]. We use the Perdew-Wang (PW91) [109] exchange correlation functional and projected augmented wave (PAW) pseudopotentials [110]. The valence configurations of the pseudopotentials are $1s^1$ for hydrogen, $3s^2 3p^3$ for phosphorus, $4s^2$ for calcium and $2s^2 2p^4$ for oxygen. Our simulation cells are on average of the size 10 Å × 10 Å × 40 Å. We use the kinetic energy cutoff of 650 eV in all calculations. The Brillouin zone integration is done using a 4 × 4 × 2 Monkhorst-Pack [111] k-point mesh. This choice of energy cutoff and k-point mesh ensures the energy convergence better than 5 meV/atom. We relax the ionic positions using the conjugate gradient method while keeping the cell shape and volume constant. Symmetry operations are switched off during the relaxation. After relaxation the largest forces acting on ions are less than 20 meV/Å.

HA has a rather large primitive cell consisting of forty four atoms in the hexagonal phase and eighty eight atoms in the monoclinic phase. Previously, we found that two phases are very close in energy, with the monoclinic structure being slightly more stable [140]. However, we found very similar electronic properties in both phases, suggesting similar behavior. Therefore, here we only consider hexagonal HA. We study the surfaces with (001) and (100) crystallographic orientations, allowing for both stoichiometric and non-stoichiometric models. By stoichiometric model we mean that the model slab contains an

integer number of HA formula units. We only consider surface terminations that keep the OH and PO_4 groups intact. In total, we construct twenty nine distinct atomic level surface models. Three of them are depicted in Fig. 4.1. The numbers in Fig. 4.1 indicate how to deduce our other models from the ones depicted. For example, removing particle "1" in Fig. 4.1 a) yields model four, removing particles "1" and "2" yields model five, removing "1"-"3" model six, and so on. In Table 4.1 we indicate by how many OH, Ca and PO_4 formula units our models deviate from the HA bulk stoichiometry and the bulk ionic charge per cell for each model. The bulk ionic charge is calculated by assigning formal charges -3*e*, -1*e* and +2*e* to the PO_4, OH and Ca chemical units, respectively. Overall, the models are charge neutral. We consider a variety of Ca-rich and Ca-poor models to account for the large Ca/P range of 1.3-1.9 found in natural bone [141]. We have two stoichiometric models, one with the (001) and one with (100) orientation. We have three more surfaces with zero bulk ionic charge. In addition, we allow for a wide range of ionic charge between -16*e* and +12*e*. As a consequence of our cleaving procedure, we only consider one surface with the positive ionic charge with the (001) orientation. For example, in Fig. 4.1 b) we successively remove three top Ca atoms before removing the phosphates to obtain the next surface model. This way the surface gets increasingly negatively charged due to the -3*e* charge of PO_4 groups. Experimentally, surfaces with net ionic charges are found to drive the HA platelets growth kinetics [142] but are typically neglected in surface studies of HA. We apply the periodic boundary conditions and fully relax the atomic positions. All our models consist of 15-20 Å thick slabs separated by a 20 Å thick vacuum region in the *c*-direction to suppress interactions between neighboring cells. Because of low symmetry, the surface models are built in a quasi-symmetric fashion to prevent the macroscopic electric fields across the slab. By quasi-symmetric we mean that on average, the atomic compositions of the top and bottom

surfaces are the same. The PO_4 groups and Ca atoms at the two surfaces can be rotated and translated in the surface planes with respect to each other as a consequence of crystal symmetry. In the (001) models, we allow for a deviation from this rule as there the OH groups have hydrogen pointing towards the bottom surface and oxygen pointing towards the top surface (Fig. 4.1 a). In these models the top and the bottom surface of each model differ in the orientation of OH groups.

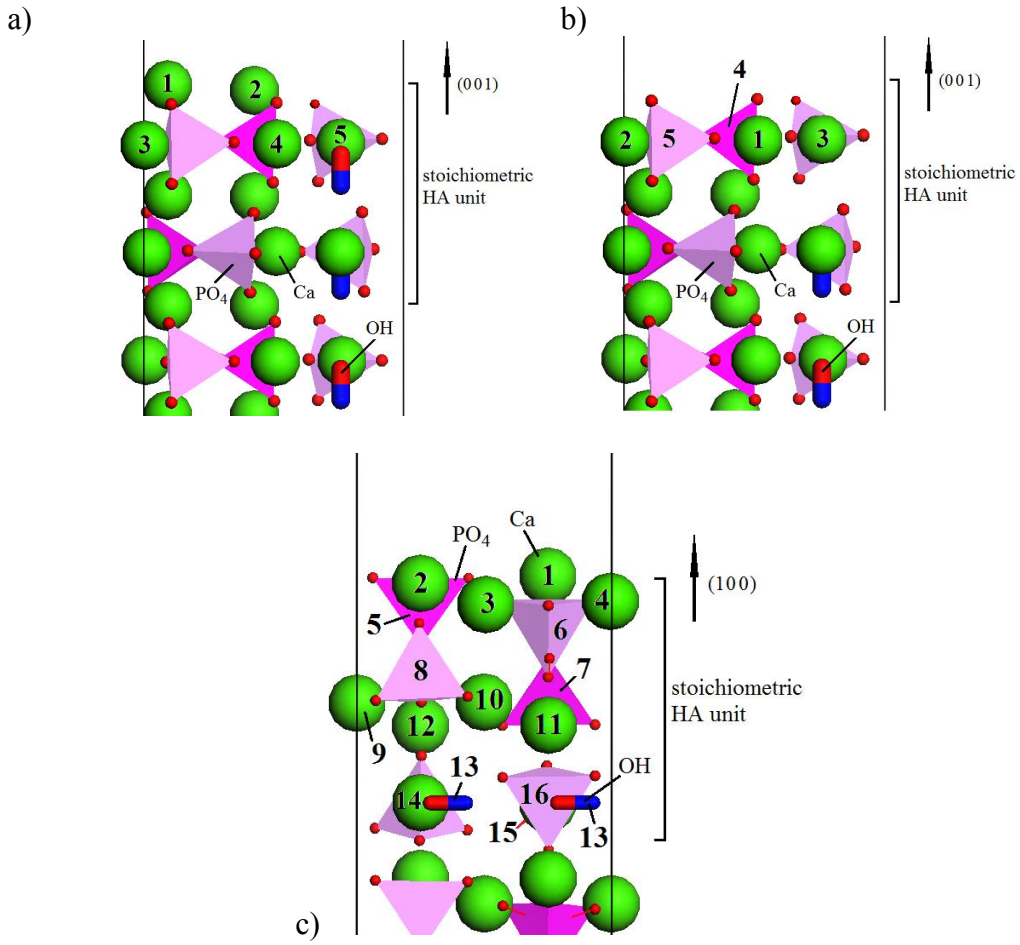

Fig. 4.1: a)-c) From these three prototypes we create all of other model surfaces by continuously removing the numbered particles. In total, we construct 29 surface models from the ones depicted.

Table 4.1: Chemical composition, ionic charge, the surface energy averaged over the entire chemical range and work function in our models. The 'extra' molecules indicate the deviation from HA bulk stoichiometry measured in numbers of OH, PO_4 or Ca. The net ionic charge is simply the sum of the extra elements multiplied by -3*e*, -1*e* and +2*e* for PO_4, OH and Ca, respectively.

model #	# extra OH	# extra Ca	# extra PO_4	ionic charge [*e*]	av. σ [eV/Å^2]	Φ [eV]
1	0	2	0	4	0.09	3.1
2	0	0	0	0	0.06	5.5
3	1	3	3	-4	0.10	7.5
4	1	1	3	-8	0.20	9.0
5	2	4	6	-12	0.28	8.6
6	2	2	6	-16	0.38	9.1
7	0	8	6	-2	-0.09	7.3
8	0	6	6	-6	-0.02	7.8
9	0	4	6	-10	0.06	8.5
10	0	2	6	-14	0.14	9.1
11	0	2	4	-8	0.31	8.0
12	0	2	2	-2	0.03	7.2
13	0	8	4	4	-0.05	3.0
14	0	6	4	0	-0.09	5.7
15	0	4	4	-4	0.00	7.2
16	0	2	4	-8	0.09	7.7
17	0	0	4	-12	0.18	8.6
18	0	0	2	-6	0.13	8.8
19	0	0	0	0	0.08	7.1
20	1	5	1	6	0.23	4.4
21	2	10	2	12	0.37	3.3
22	2	8	2	8	0.31	3.1
23	2	6	2	4	0.25	3.3
24	2	4	2	0	0.20	5.1
25	2	2	2	-4	0.62	9.7
26	0	12	8	0	-0.23	6.7
27	0	10	8	-4	-0.14	7.6
28	0	8	8	-8	-0.05	8.8
29	0	8	6	-2	-0.12	7.6

4.3 SURFACE ENERGY

The primitive unit cell of HA consists of four atomic species that form two OH, six PO_4 groups, and ten Ca atoms per cell. Thus, to simplify the description, we consider the crystal to be composed of these three building elements. To estimate the surface energy we use the Gibbs free energy formalism [83]. This approach allows for comparisons of structures with different stoichiometry. The surface energy is given by

$$\sigma = \left[E_{slab} - \sum_i N_i \mu_i \right] / 2A. \tag{4.1}$$

Here E_{slab} is the energy of the slab computed from first principles and μ_i and N_i are the chemical potential and number of the i-th building element, respectively. A is the surface area of the slab, the factor of two accounts for two surfaces per slab. Assuming thermodynamic equilibrium of the surface with the HA bulk imposes the following condition:

$$\sum_i N_i \mu_i = \mu_{HA}, \tag{4.2}$$

where μ_{HA} is the chemical potential of the HA bulk phase, which we take equal to the bulk energy. Referencing chemical potentials of building elements to the corresponding bulk phases $\mu_i = \tilde{\mu}_i + \mu_{i,bulk}$, equation (4.2) can be rewritten as:

$$\sum_i N_i \tilde{\mu}_i = -E_f . \tag{4.3}$$

Here E_f is the formation energy. We reference the chemical potential of Ca to bulk metallic Ca. For OH and PO_4 molecules we use the energy per corresponding isolated molecule as a reference. The calculated formation energy of -111.7 eV per $Ca_{10}(PO_4)_6(OH)_2$ molecular unit is in qualitative agreement with the experimental heat of formation of -138.9 eV [143]. The surface energy is then estimated as:

$$\sigma = \left[E_{slab} - N_{Ca}\left(E_{Ca} + \tilde{\mu}_{Ca}\right) - N_{OH}\left(E_{OH} + \tilde{\mu}_{OH}\right) - N_{PO_4}\left(E_{PO_4} + \tilde{\mu}_{PO_4}\right) \right] / 2A. \tag{4.4}$$

The range of chemical potentials is determined by:

$$10\tilde{\mu}_{Ca} + 2\tilde{\mu}_{OH} + 6\tilde{\mu}_{PO_4} = -E_f, \quad -E_f < \tilde{\mu}_i < 0. \tag{4.5}$$

With these boundary conditions we calculate the surface energy. In Table 4.1 we list the surface energy of each model averaged over the entire chemical range. In Fig. 4.2 we plot the averaged surface energy as a function of bulk ionic charge.

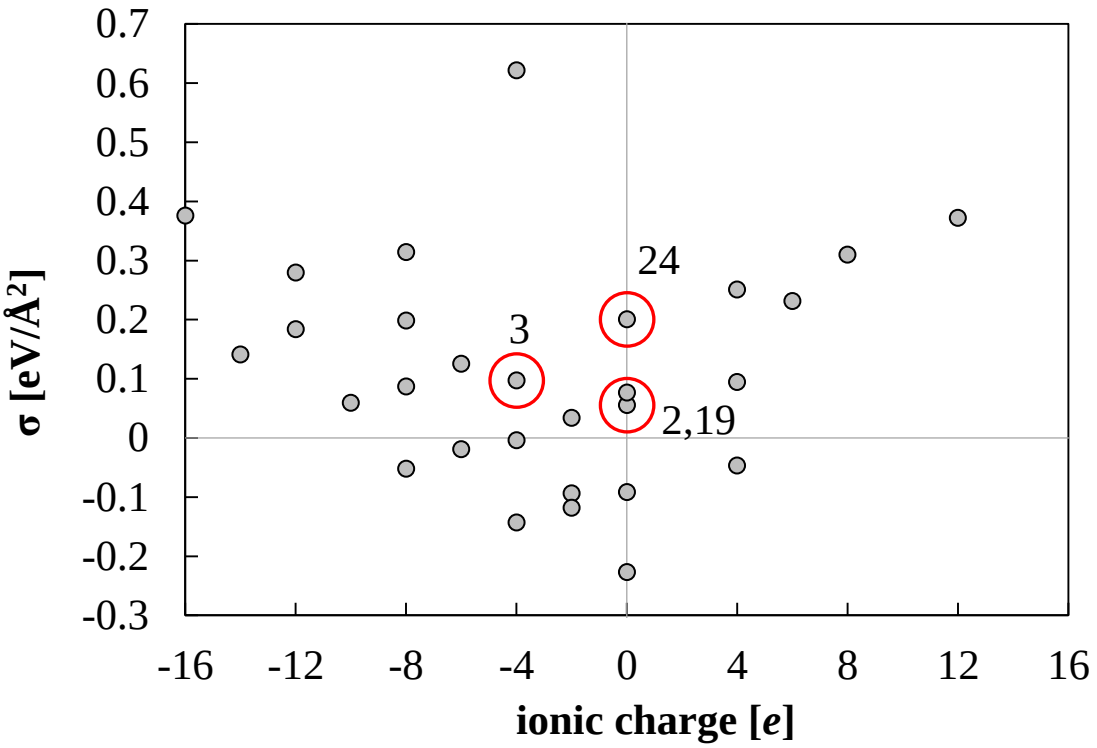

Fig. 4.2: Surface energy averaged over the entire chemical range plotted as function of the surface net ionic charge. Models 2 and 19 are the stoichiometric (001) and (100) surfaces. Models 3 and 24 are the models with lowest surface energy under OH-rich conditions.

With increasing ionic charge the surface energy increases. Large ionic charge indicates that the surface strongly deviates from the HA stoichiometry. This leads to under-coordinated functional groups Ca, OH and PO_4. Overall our models are charge neutral; however, and under-coordinated functional groups on the surface create surface dipoles that in turn increase the slab energy. The surface energy ranges between -0.23 eV/Å^2 and 0.62 eV/Å^2. To interpret the data we assume that this is the relative energy rather than its absolute value (this reflects the arbitrary choice of thermodynamic references). Alternatively, the negative energy may be interpreted as the surface being more stable than the bulk, and therefore unstable under given conditions. Our stoichiometric (001) and (100) surfaces (models 2 and 19) have energy 0.055 eV/Å^2 and 0.076 eV/Å^2, respectively, in good agreement with the 0.075 eV/Å^2 and 0.105 eV/Å^2 reported by Astala *et al.* [41], and the 0.054 eV/Å^2 reported by Rulis *et al.* for the (001) orientation [33]. Furthermore, our models 14 and 24 correspond to Astala's PO_4-rich and Ca-rich surfaces, respectively. Astala calculates the surface energy with respect to the β-tricalcium phosphate with the formula unit $Ca_3(PO_4)_2$, and $Ca(OH)_2$. These two references are reasonable choices; however, in practice they greatly reduce the number of allowed surface terminations. Astala's surface energy is 0.11 eV/Å^2 and 0.10 eV/Å^2 for the PO_4-rich and Ca-rich surfaces, respectively, averaged over the allowed chemical potential range. We find the average values 0.05 eV/Å^2 and 0.06 eV/Å^2 for these two surfaces with respect to $Ca_3(PO_4)_2$ and $Ca(OH)_2$. We attribute the deviation from Astala's work to their method of constructing the surface. While our surface models are constructed in a quasi-symmetric way as described earlier to suppress macroscopic electric fields across the slab, Astala's surface models are terminated stoichiometrically on one side and with the termination of interest on the other side. This inevitably creates an electric field across the slab and modifies the surface energy. Note, that all these

models have zero bulk ionic charge as we have pointed out earlier. The surface energy phase diagram is shown in Fig. 4.3. We show surface models with the lowest surface energy under given chemical conditions as captured by the chemical potentials. In the following discussion we will refer to this lowest surface energy as the ground state surface energy. The black lines are phase boundaries where two or more surfaces have the same energy. It is worth noting that despite the complex crystal structure, surface model 26 has the lowest surface energy over almost the entire chemical range. However, despite this domination, in the experimentally relevant regime of OH-rich conditions surface model 26 plays no role and will not be discussed.

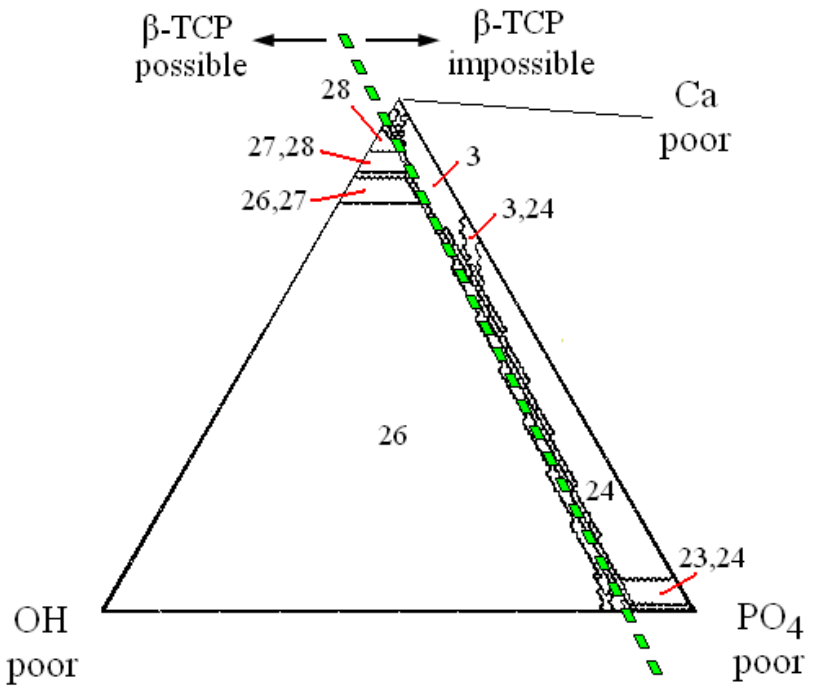

Fig. 4.3: Lowest surface energy ternary phase diagram. Only six of the surface models notably contribute to the energetic ground state. Thin lines indicate the phase boundaries between surfaces competing in energy. A thick dividing line indicates conditions under which the β-TCP formation is energetically possible.

The phase diagram becomes more complicated under the OH-rich conditions. We find a series of phase boundaries even for the slightest changes in chemical environment. This might account for the experimentally observed complicated surface structures when growing HA in solution. Under the OH-rich conditions, our models 3, 23, 24, and 27-28 have the lowest surface energy. Note, that of these, only model 3 has the (001) orientation. Model 3 differs from the stoichiometric model 2 only by having one less Ca atom at the surface. Models 23 and 24 are also relatively similar, the only difference again being one less Ca at the surface of model 24. As will be discussed in the next section, this one Ca atom stabilizes geometry in which the OH groups are aligned in channels parallel to the surface. Models 26-28 also are rather similar to each having the OH channel deep inside the bulk region and a rather high surface roughness, resembling a β-tricalcium phosphate (β-TCP) surface. Indeed, a comparison can be drawn at this point. In equation (5) we require that the sum of chemical potentials of the building blocks Ca, OH and PO_4 must equal the heat of formation of HA with respect to these building blocks. One can consider an additional constraint set by

$$3\tilde{\mu}_{Ca} + 2\tilde{\mu}_{PO_4} < \mu_{\beta-TCP}. \tag{4.6}$$

The formula unit of β-TCP is $Ca_3(PO_4)_2$, and as long as inequality (4.6) holds, β-TCP formation is impossible. Violating inequality (4.6) means that β-TCP-like surface layers may appear if not enough OH is present in the environment. The condition is "soft" as (4.6) does not indicate how the remaining OH groups influence the β-TCP formation. In Fig. 4.3 the corresponding transition line is indicated. Note in Table 4.1, that while the bulk region of model 26 has HA stoichiometry, its surface stoichiometry is that of β-TCP! In the following we shall focus on the OH-rich conditions as more biologically relevant.

4.4 OH-RICH CONDITIONS

For the OH-rich conditions we set $\tilde{\mu}_{OH} = 0$ in equations (4.3) and (4.4). Then, using (4.3), we rewrite equation (4.4) as:

$$\sigma = \left[E_{slab} - N_{Ca}E_{Ca} - N_{OH}E_{OH} - N_{PO_4}\left(E_{PO_4} - \frac{1}{6}H_f \right) - \tilde{\mu}_{Ca}\left(N_{Ca} - \frac{5}{3}N_{PO_4} \right) \right] / 2A \quad (4.7)$$

.

Equation (4.7) is solely a function of $\tilde{\mu}_{Ca}$, that ranges from $-E_f/10$ for Ca-poor conditions to zero for Ca-rich conditions. The surface energy is shown in Fig. 4.4. Note that the stoichiometric (001) surface termination (0.055 eV/Å^2) is never the ground state. Consistent with the previous discussion, we find that the surface models 3 (Fig. 4.5) and 24 (Fig. 4.6) have the lowest energy over the majority of the chemical range. For Ca-rich conditions, surface models 23, 22 and 21 are stabilized, while for Ca-poor conditions five structures compete with model 3. Models 3, and 21-24 all have OH molecules very close to the surface (Fig. 4.2). In Fig. 4.5 we show the relaxed surface geometry of model 3. In Fig. 4.7 a) we plot the bond angle distribution of the PO_4 groups close to the surface. In bulk HA, the angle distribution has two distinct peaks at 107.5° and at 111.5°. In the slab the relaxed angles of the surface PO_4 are more evenly distributed between ~104° and 113.5°. The OH bond lengths are 0.97 Å - 0.98 Å, and are similar to 0.977 Å in the bulk [140]. However, 4.6 Å below the surface the PO_4 groups already closely resemble the bulk.

In Fig. 4.7 b) we show the layer resolved electronic density of states (DOS). Each layer is approximately 1.7 Å thick. We only show the upper valence band region. The projections on the very left and the one on the very right show the DOS at the surface. The energy gap between the Fermi level and the bottom of the conduction band is 5.2 eV. The vacuum energy is at 7.5 eV, and the zero energy is set at the Fermi level. The Fermi level is pinned at the surface by both $O_{(P)}$ and $O_{(H)}$ p-states and Ca states, reaching deep in the

bulk region. The bottom of the conduction band mainly consists of $l = 2$ projected states of the Ca atoms. The valence band of the bulk region resembles that of bulk HA [140]. For bulk HA we found the band gap of 5.2 eV [140].

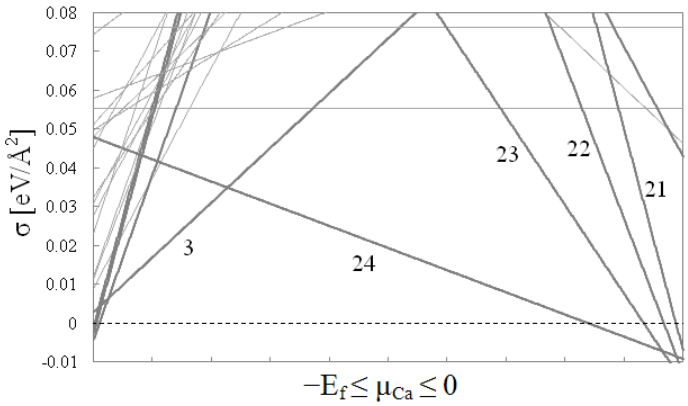

Fig. 4.4: Surface energy under OH-rich conditions. Main contributors are structures 3 and 24.

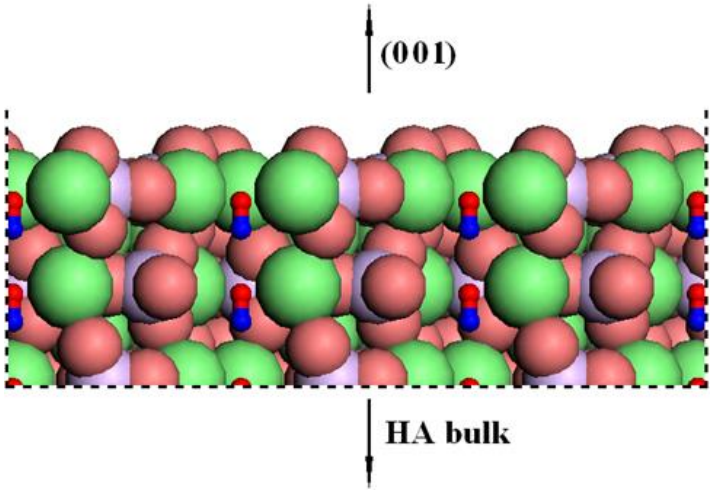

Fig. 4.5: Side view of relaxed model 3. The surface is one of the low energy surfaces under OH-rich conditions.

a)

b)

c)

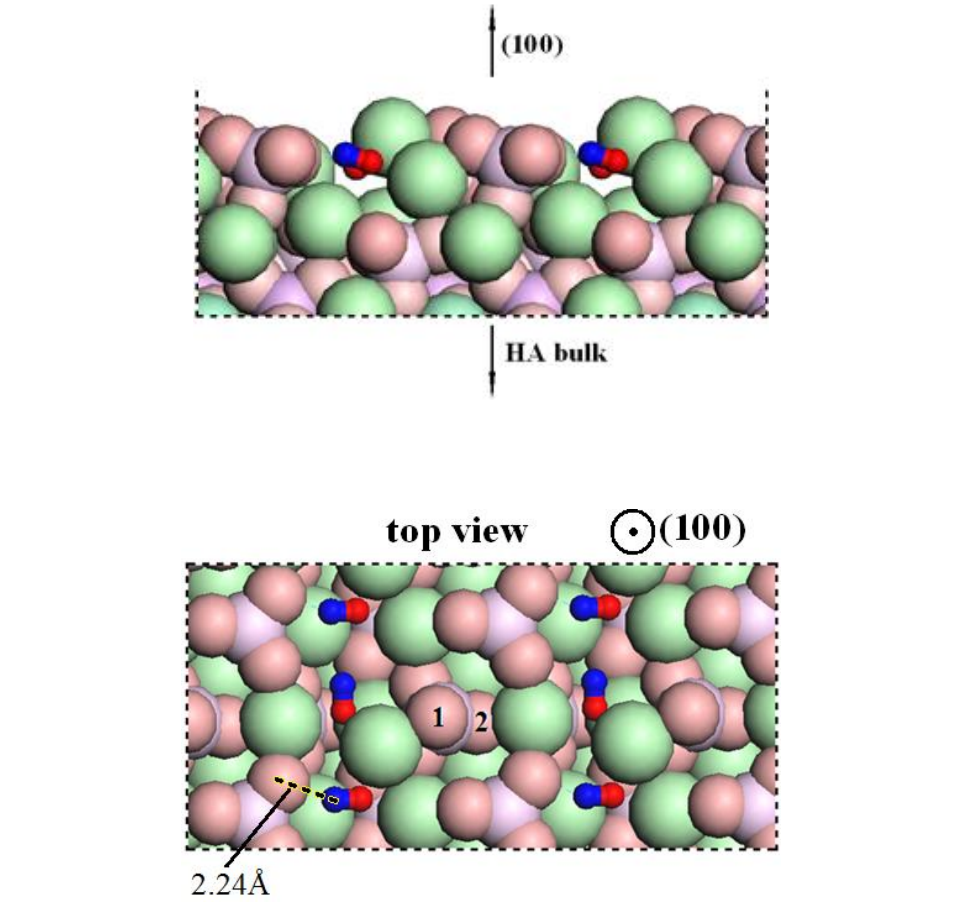

Fig. 4.6: The side (a) and top (b) views of relaxed model 24. This surface has the lowest energy over most of the chemical range under OH-rich conditions. It is terminated just above the hydroxyl layer and allows for major reconstruction in order to bind OH to the surface. For pictorial purpose we show a periodically extended cell.
c) OH-relaxation: Dark large balls are Ca 'deeper' in-plane than the light large Ca balls. In model 24 one of the Ca is missing, allowing OH to rotate.

Of particular interest is surface model 24 as it contains OH groups right at the surface which is related to work of Sato *et al.* [139] who first described the OH terminated HA surface. In Fig. 4.6 a) and b) we show the relaxed surface of hydroxylated model 24. This surface has the most significant surface reconstruction among those studied. It is stepped on the Angstrom scale, and has a negative surface energy under Ca-rich conditions. One of the OH groups is tilted 90° from its original position, breaking its bond to the neighboring OH group and instead re-bonding with neighboring oxygen of a phosphate group as shown in Fig. 4.6 b). This rotation occurs for the following reason. In bulk HA each OH is centered within an equilateral triangle made up by calcium [140] as indicated in Fig. 4.6 c). The large dark and light green balls indicate calcium atoms in two atomic layers. In the figure, the darker balls are 'deeper' and the lighter green balls are 'higher'. The empty circle indicates missing Ca. We indicate one OH in the figure whose hydrogen atom is beneath the visible oxygen. While the deeper OH is still surrounded by three Ca atoms, in the upper Ca-triangle one Ca is missing and the OH gruop is free to adjust. It is this OH group that rotates 90° with respect to the original alignment as indicated in Fig. 4.6 c). The triangles in the figure mark the original positions of Ca before relaxation. The surface allows for major relaxation to compensate for missing Ca. In Fig. 4.6 b) all OH were vertically aligned before relaxation.

Interestingly, removing Ca closest to vacuum in model 24, exposes the second OH group and results in model 25 that is very high in energy. In Fig. 4.8 a) we plot the angle distribution of the PO_4 groups close to the surface. In the slab the relaxed angles of the surface PO_4 spread from ~105.5° to ~120°. The distortion is still large in a PO_4 group 4.3 Å beneath the surface. The largest change in bond angle is ~9° as indicated in Fig. 4.6 c). In Fig. 4.6 b) this angle is formed between oxygen atom 1, the phosphorus within the PO_4 group and oxygen atom 2 as indicated in the figure. Phosphate groups more than 4.5 Å

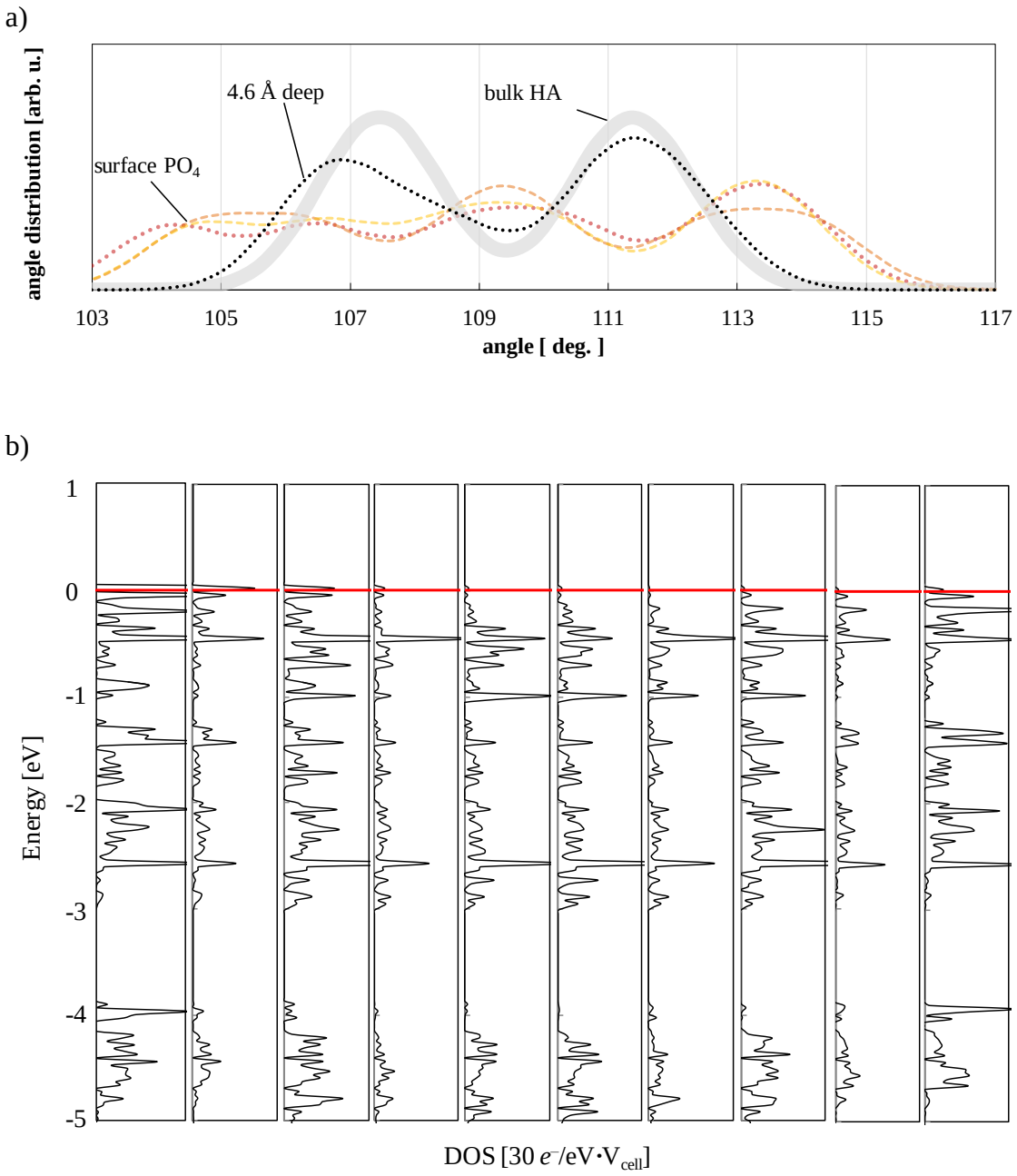

Fig. 4.7: a) P-O-P angle distribution in model 3. On the surface we find large deviation from the bulk P-O-P angles. Below 4.6 Å from the surface, however, the bulk distribution is restored.
b) Layer decomposed density of states of model 3. We show the top of the valence band only. The Fermi level is at 0 eV.

beneath the surface are nearly undistorted compared to bulk HA. The PO_4 bond lengths are on average comparable with the ones in bulk HA. The bond lengths of the OH range between 0.98 Å and 0.99 Å, in excellent agreement with the bulk value. In Fig. 4.8 b) we show the layer projected DOS. Again, we only show the top of the valence band. The Fermi level is at 0 eV, the vacuum energy level is at 5.13 eV (not shown). Only 4 Å away from the surface, the DOS of bulk HA is restored. The top of the valence band is pinned by the surface Ca-centered $l = 2$ sate and surface $O_{(P)}$ p-states The GGA band gap of this slab model is 3.5 eV.

The unusual rotation of one of the surface hydroxyl groups suggests a change in vibrational properties. We compute the frequency of the OH vibrational modes at the surface and, for comparison, deep inside the bulk region of the slab by calculating the eigenvalues of a reduced dynamical matrix, built only from the OH force constants. The force constants are deduced from the Hellman-Feynman forces. For the rotated OH molecule the vibrational frequencies are 3571 cm^{-1} for the stretch mode, and 835 cm^{-1} and 560 cm^{-1} for the libration modes. For the second surface OH we find 3666 cm^{-1}, 708 cm^{-1} and 649 cm^{-1} for the stretch and the two libration modes, respectively. For the OH vibrations in the bulk region of the slab, we find 3662 cm^{-1}, and 699 cm^{-1} and 677 cm^{-1} for the stretch and libration modes. For comparison, in the bulk HA study we found 3660 cm^{-1} for the stretch mode and 693 cm^{-1} for the two-fold degenerate libration mode [140]. This is in agreement with the structural relaxation decaying within 4 Å below the surface. At the surface, however, while the stretch mode of the regularly aligned OH molecule is similar to the bulk value, the stretch mode of the rotated OH molecule is red-shifted by 89 cm^{-1}. The red-shift may be attributed to a decrease in the force constant: In bulk HA, the two OH-groups in the primitive cell are aligned, with the distance of approximately 2.50 Å between neighboring OH. The rotated OH, however, binds to a

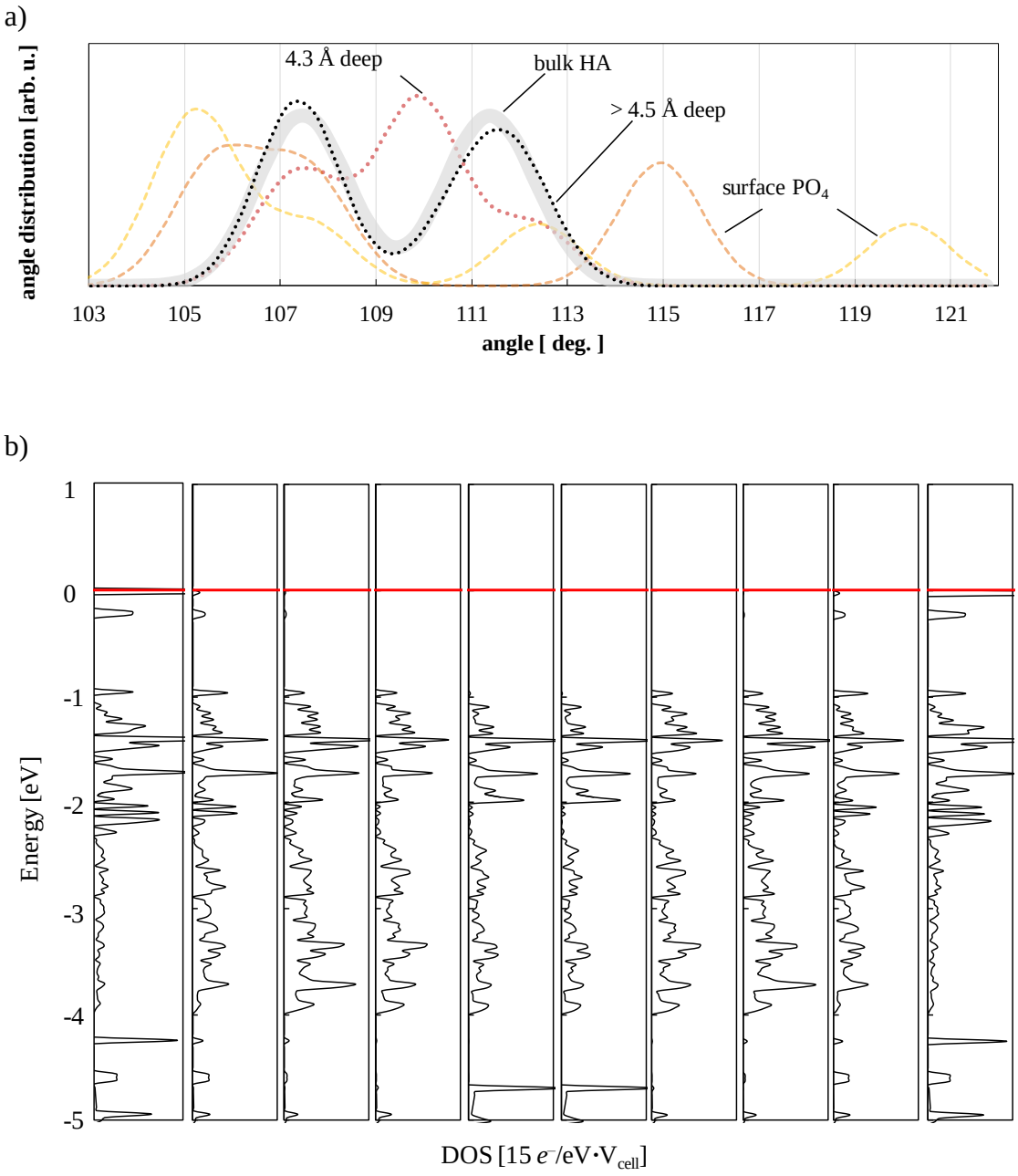

Fig. 4.8: a) P-O-P angle distribution in model 24. Below 4.5 Å from the surface bulk angle distribution is restored. The largest deviation from the bulk angles is 9° in one of the surface PO_4 molecules.
b) Layer decomposed density of states of model 24. We show the top of the valence band only. The Fermi level is at 0 eV.

phosphate oxygen (as shown in Fig. 4.6 b)) with the bond length of 2.24 Å. This $O_{(P)}$-H bond weakens the $O_{(H)}$-H covalent bond, effectively reducing the force constant of the OH stretch, lowering the frequency. The libration modes also deviate from the bulk values mostly for the rotated OH group. The degeneracy is lifted, resulting in a blue-shift by 142 cm^{-1} of one mode and a red-shift by 133 cm^{-1} of the second mode. Changes for the librational modes of the un-rotated OH are significantly smaller. These shifts in the vibration modes should be observable in a spectroscopic analysis.

4.5 WORK FUNCTION

Another important question is how the surface structure and composition influence the work function of HA. The work function is one of several key parameters determining charge transfer at the material's interface. In photoelectron emission measurements, the work function is found to range between 4.7 eV and 5.1 eV [119], and to correlate with the size of the HA particles used for the measurement and with concentration of hydrogen atoms at the surface [119]. However, as the exact structure and composition of the surface are not known, the physical origins of these correlations are unclear. Therefore, a theoretical analysis of the work function is of both fundamental and practical interest. We calculate the work function using the local electrostatic potential method. The microscopic local potential across the simulation slab is calculated as a function of distance in the direction normal to the surface (the z axis) by averaging over the x-y plane. The value of this plane-averaged potential in the vacuum region is taken as the vacuum level. The work function is then computed as the difference between the Fermi energy of the slab and the vacuum level. Our results for the work function are

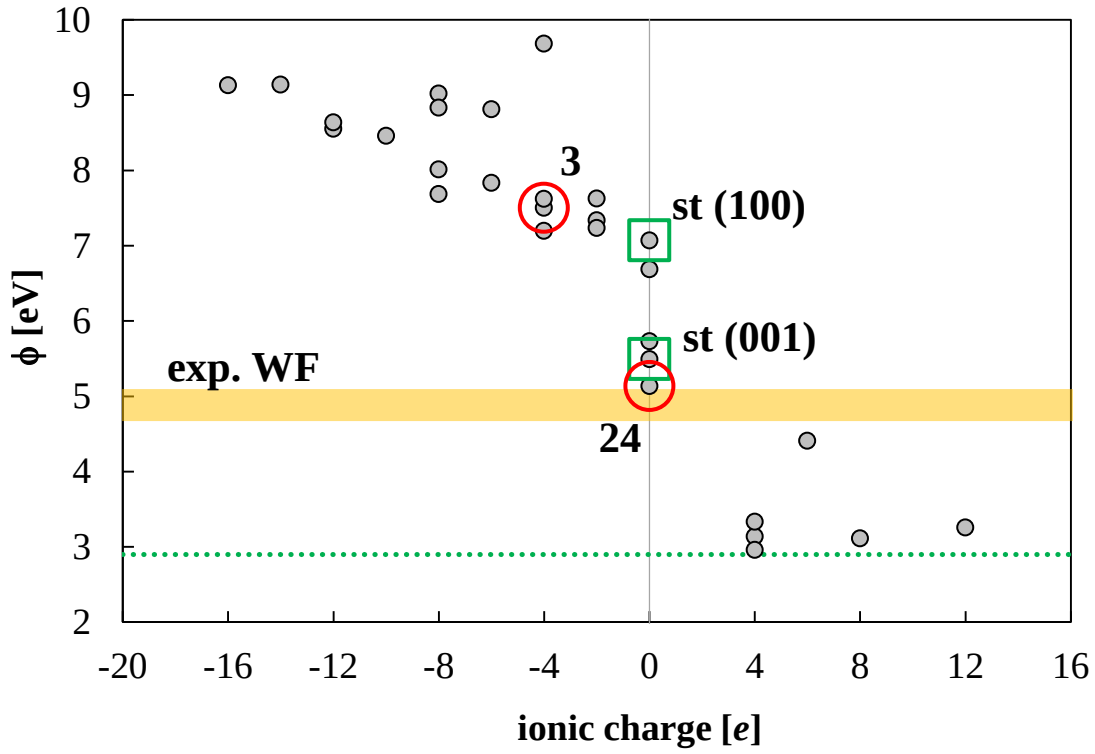

Fig. 4.9: Work function as a function of the net ionic surface charge. Surfaces with unbalanced PO_4^{3-} and OH^{1-} molecules have negative net charge; surfaces with unbalanced Ca^{2+} atoms have positive net ionic charge. The work function strongly depends on the surface chemistry, ranging from 3 eV to 9.5 eV. The range of experimental work function is indicated by the shaded bar.

summarized in Table 4.1. Surprisingly, the work function ranges between 10 and 3 eV, depending on the specific model. To gain further insight, in Fig. 4.9 we plot the work function as a function of the bulk ionic charge in the surface slab. A negative ionic charge indicates that the model contains unbalanced PO_4^{3-} and OH^{1-} groups. Positive net ionic charge means that the surface contains unbalanced Ca^{2+}. The plot reveals that mostly

responsible for the large variation in the work function are the two functional groups PO_4 and Ca, whose concentration varies significantly at the surface. The energy levels of valence 4*s* electrons in Ca are relatively close to vacuum, leading to the low work function of 2.9 eV for bulk Ca metal. On the other hand, the occupied orbitals of the covalently bonded PO_4 group have very low energy. Thus, in the Ca-rich surface models the work function tends to be close to that of bulk Ca, while in the PO_4-rich models it varies between 7 eV and 10 eV. This is what one would expect for the anti-bonding states of PO_4 groups (the energy of the sp^3-hybryd in phosphorus is -10.5 eV and the *p*-orbital of oxygen is at -14.3 eV, with respect to vacuum). The stoichiometric (001) surface has work function 5.5 eV, and (100) stoichiometric surface has work function 7.1 eV as indicated in Fig. 4.9. The work function of the two surface models most stable under OH-rich conditions (model 3 and 24) is pointed out by the large circles in Fig. 4.9. For model 3 we find 7.5 eV. Interestingly, for model 24 we find 5.1 eV in the closest agreement with the experimental value. This again suggests that it may be a good model for the OH-terminated HA surface described by Sato *et al.* [139].

4.6 CONCLUSIONS

Using density functional theory, we carried out a comprehensive study of the vacuum-cleaved surface of important biomineral HA. The study is a first step in considering interfaces of HA with Ti and TiO_2 which are important in biomedical applications. Considering a wide range of surface compositions and orientations, we identified the ionic surface charge, caused by deviation of bulk stoichiometry, as the main origin of the increase in the vacuum-cleaved surface energy. For the biologically relevant OH-rich environment we found two dominant surface structures, one with the (001)

orientation, and one with the (100) orientation. The (100) surface has OH groups directly facing vacuum. The surface undergoes major reconstruction to stabilize the OH groups. The reconstruction results in a red shift of the surface OH vibrational mode at 3660 cm^{-1} by 89 cm^{-1} and lifts the degeneracy of the libration modes at 693 cm^{-1} by 275 cm^{-1}. Such changes in the absorption spectrum should be observable in spectroscopic experiments and would help determining surface composition. The work function of HA is found to range from 3.0 eV for the Ca-rich termination to 9.7 eV for Ca-poor surfaces. The work function of the OH-terminated surface, similar to one suggested in Ref. 26, is 5.1 eV, in very good agreement with the experimentally reported values that range from 4.7 eV to 5.1 eV [119].

5. Hydroxyapatite: Vibrational spectra and phase transition

The results of this Chapter are submitted to the Physics Review.

5.1 INTRODUCTION

Hydroxyapatite [HA, $Ca_{10}(PO_4)_6(OH)_2$] oxides have attracted considerable interest owing to their role in human bone to which they give its remarkable mechanical strength [144]. The apatite structure is significantly more complex both in terms of size and diverse chemical bonding, than that of many other oxides such as perovskites or spinels, making it rather difficult to study. On the other hand, HA's biocompatibility is widely exploited in biomedical applications. For example, it is used as a coating layer on a titanium body of a bone implant in order to adapt it to the physiological environment and possibly increase the implant life span. Such applications, however, require detailed physical insight in the thermodynamics of HA due to the complex physical environment it is used in. In particular, understanding HA's thermodynamic stability including phase transitions, growth, and decomposition with aging [2] is needed both experimentally and theoretically to ensure further technical development.

The crystal structure and atomic positions of HA were first determined in 1958 by Posner *et al.* using the X-ray diffraction [5]. In 1964, Kay and co-workers refined the positions of the OH molecules using neutron diffraction [6]. HA was believed to only crystallize in the hexagonal $P6_3/m$ structure until Young suggested a monoclinic variant of HA in 1967 [7]. He inferred that a HA crystal sufficiently free of impurities and vacancies could crystallize in the monoclinic phase analogous to monoclinic chlorapatite. The monoclinic phase has attracted interest recently as it could potentially alter the physical mechanisms leading to the formation of HA nano-crystals in bone due to slight differences in its

dielectric properties [11,12]. A considerable amount of experimental work on HA exists in particular in the medical implant field. For an excellent review of this work we refer the interested reader to [3].

Theoretically, HA crystal presents a formidable challenge due to its complexity and importance in biophysical systems with potential applications. Only with the recent increase in computational power a theoretical study of HA became feasible. And HA along with other calcium apatites HA have been subject to a number of recent studies using first principles calculations. The work includes ground state bulk electronic properties studies [23,24, 27,140], studies on ion substitutions and their influence on bulk and electronic properties [24,29,34,38,39,40], studies on altering the electronic and chemical properties of HA through doping [38], surface studies [27,32,34,145] and studies on the adsorption of small molecules on HA surfaces [27,34,41,46].

Interestingly, despite providing direct access to important thermodynamic quantities such as heat capacity, the vibrational spectrum of HA remains only marginally studied. The most recent work on the HA's vibrational properties are two experimental studies by Fowler *et al.* and Markovic *et al.,* who report the infrared and Raman active modes of the material, respectively [21, 22]. Existing theoretical work on HA's vibrations mainly employs classical shell models and is often limited to studying the long wave length limit [*e.g.* 29]. A practical difficulty of using classical shell models is that the model potentials fitted to reference data are in general not transferable [29].

In this paper we present a density functional theory (DFT) study of HA's vibrational properties and phase transformation of HA from a hexagonal to a monoclinic phase. The previous theoretical work [*e.g.* 140 and references therein] on the phase transition mainly focuses on the transition barriers and transition paths. Our previous studies of HA [140,145] suggest that DFT provides a surprisingly reliable description of this complex

material. The rest of the paper is organized as follows. We first summarize computational details and describe various simulation cells used in this work. We then describe theoretical phonon dispersions of the monoclinic and hexagonal phases and their thermodynamic properties within the harmonic approximation. We discuss the Lyddane-Sachs-Teller frequency shifts due to the long-range Coulomb effects, and report on a peculiarity in the phonon dispersion that might lead to useful applications. Based on our calculations, we suggest a phase transition mechanism and estimate the transition temperature. We also use a phase transition model to calculate the transition temperature for comparison. We conclude with calculating the heat capacity and the Debye temperature.

5.2 COMPUTATIONAL DETAILS

We use a plane wave code VASP to solve the Kohn-Sham problem [51-55]. To estimate the exchange-correlation energy contribution to the total energy we use the Perdew-Wang (PW91) generalized gradient approximation functional [109]. We use projected augmented wave (PAW) pseudopotentials as implemented in VASP [110]. The valence configurations of the pseudopotentials are $1s^1$ for hydrogen, $3s^2 3p^3$ for phosphorus, $4s^2$ for calcium and $2s^2 2p^4$ for oxygen. For both, the monoclinic and hexagonal phases we use a primitive cell with lattice constants 9.535 Å × 19.07 Å × 6.91 Å. That choice corresponds to one regular monoclinic primitive cell and a hexagonal cell doubled in the ***b***-direction. We use the energy cutoff of 500 eV along with a 4×2×4 Monkhorst-Pack k-point mesh for the Brillouin zone integration [111] when calculating the phonon dispersion. To compute the dynamical matrix we use a 2×1×2 supercell with dimensions 19.07 Å × 19.07 Å × 13.82 Å, containing a total of 352 atoms. We use a

2×2×2 Monkhorst-Pack *k*-point mesh for the Brillouin zone integration of that cell. The energy is converged to less than 10 meV/atom. In the primitive cell we relax the ionic positions, the cell shape and volume until the residual forces acting on ions are smaller than 5 meV/Å. Symmetry operations are switched off during the relaxation. Comparing the eigenmodes at the Γ-point with our previous results [140], where a denser k-point mesh and a 950 eV energy cutoff were used with a smaller cell, we find excellent agreement.

5.3 RESULTS

5.3.1 Simulation cells and notations

The chemical formula of hexagonal HA is $Ca_{10}(PO_4)_6(OH)_2$, and for monoclinic HA it is $[Ca_{10}(PO_4)_6(OH)_2]_2$. In Fig. 5.1 we show the top-view on the primitive hexagonal cell. For pictorial purposes we shift the original primitive cell boundaries along the ***a*** and ***b*** axes in such a way that the OH group is at the center of the cell and points with the hydrogen atom into the plane (in the picture it is the -*z* direction). There are two OH groups in the center, one visible in Fig. 5.1, and one "hidden" underneath. For a more detailed description of the hexagonal and monoclinic primitive cells we refer the reader to reference [140]. In order to differentiate between the hexagonal and monoclinic phases, we use a pair of arrows to describe the orientation of two OH groups in the hexagonal cell. The arrows point either in +*z* direction (the hydrogen atom is above the oxygen atom) or in –*z* direction (the hydrogen atom is below the oxygen atom). We can represent the hexagonal primitive cell by (↓↑) or (↓↓), *i.e.* the OH molecules are either aligned parallel or antiparallel to each other. The former has symmetry $P6_3/m$ (*#176 in the International X-Ray Tables*, with center-symmetry) and is the one reported by Kay

and Young [6]. The latter cell has symmetry $P6_3$ (*#173 in the International X-Ray Tables*, non-centrosymmetric) and is the lowest energy structure. Through the remainder of this paper we consider the hexagonal structure (↓↓)(↓↓), where we doubled the original primitive cell in ***b***-direction. The monoclinic phase consists of two hexagonal primitive cells connected in ***b***-direction. Here a number of different OH orientations are possible. Previously [140], we have found the (↓↓)(↑↑) monoclinic cell with $P2_1$ symmetry (*#4 in the International X-Ray Tables*, non-centrosymmetric) to have the lowest energy. Within the given theoretical setup it also is 50 meV per cell lower in energy than the hexagonal (↓↓)(↓↓) phase and thus is the ground state crystal structure under the ambient conditions. In the following we will refer to the (↓↓)(↑↑) structure when talking about the monoclinic phase.

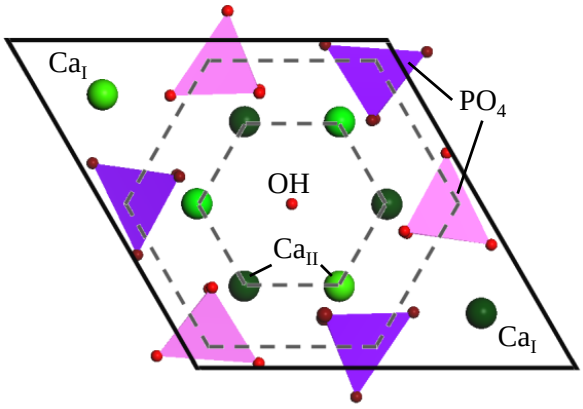

Fig. 5.1: Top-view on the hexagonal primitive cell. We shifted the original primitive cell in the x and y directions so that the OH column is in the center of the depicted cell. The darker colored Ca_{II} atoms and PO_4 molecules are centered at z=0.25c and the lighter ones are centered at z=0.75c. The OH column is surrounded by six Ca_{II} atoms and six PO_4 molecules. The Ca_I atoms are now in the corners of the cell. Below both of the two visible Ca_I atoms there is a second Ca_I atom at the distance 0.5c. Here, the lighter Ca_I atom is close to the top face and the darker Ca_I atom is at ~0.5c.

5.3.2 Phonon dispersion

We have recently reported the phonon frequencies at the Γ point along with the approximate phonon density of states for hexagonal HA [140]. Here, we calculate from first principles the phonon dispersion along high-symmetry directions in the entire Brillouin zone for both hexagonal and monoclinic HA. Our primitive cells (↓↓)(↓↓) and (↓↓)(↑↑) contain 88 atoms each. In each cell we calculate the Hellman-Feynman restoring forces for 2×3×88 atomic displacements in order to obtain the short range force constant matrix [80]. The factor of *2* is due to displacing each atom in +/- {*x*, *y*, *z*} directions around the equilibrium position when numerically evaluating the second derivative to eliminate the odd power anharmonicity. The lattice Fourier transform of the force constant matrix yields the dynamical matrix [80]:

$$\vec{D}(\vec{k};\mu,\nu)=\frac{1}{\sqrt{M_\mu M_\nu}}\sum_m \vec{B}(0,\mu;m,\nu)\cdot\exp\left\{2\pi i\vec{k}\cdot\left[\vec{R}(0,\mu)-\vec{R}(m,\nu)\right]\right\}. \tag{5.1}$$

The $\vec{R}(0,\mu)$ is the position of atom μ in the *0*-th primitive cell within the supercell. $\vec{R}(m,\nu)$ is the position of atom *v* in the *m*-th primitive cell. We use simulation cells of size 19.07 Å × 19.07 Å × 13.82 Å consisting of four primitive cells. $\vec{B}(0,\mu;m,\nu)$ are the force constants relating atoms $(0,\mu)$ and (m,ν), and M_μ and M_ν are their masses. In practice, one has to truncate the infinite lattice sum in (5.1), which is justified if the short-range restoring forces decay rapidly with increasing distance. In Fig. 5.2 we show all restoring forces as function of distance between the displaced and responding atoms. As can be seen, the forces are negligible after a distance of 4 Å – 6 Å, and are well contained within our simulation cell. In addition to these short-ranged forces, in the ionic system one has to consider the long-ranged dipole-dipole interactions. We do that by adding a long-range correction to the dynamical matrix given by [80]

$$\vec{D}^{\,\text{long}}_{\alpha\beta}(\vec{k};\mu,\nu)=\frac{e^2}{V\varepsilon_0\varepsilon_\infty}\frac{\left[\vec{k}\vec{\vec{Z}}^*(\mu)\right]_\alpha\left[\vec{k}\vec{\vec{Z}}^*(\nu)\right]_\beta}{\left|\vec{k}\right|^2}\times\exp\left(-\frac{\left|\vec{k}\right|^2}{\rho^2}\right), \tag{5.2}$$

where we use SI units. $\vec{\vec{Z}}^{*}(\mu)$ is the Born effective charge tensor of atom μ in the primitive cell, and V is the volume of the primitive cell. $\vec{k}\vec{\vec{Z}}^{*}(\mu)$ is a vector, and α and β are its $\{x,y,z\}$ components. The Born effective charge tensors introduce a directional dependence in equation (5.2). We use the Born effective charge tensors we reported in ref. 140. The ρ parameter controls the range of the long-range correction term in the reciprocal space. We choose ρ = 0.02 Å^{-1}. The long-range correction is inversely proportional to the dielectric constant ε_∞ and $\left|\vec{k}\right|^2$, and only affects the optical modes in the vicinity of the Γ point. In the literature, the values of ε_∞ for HA vary between ε_∞ = 5 and ε_∞ = 20 [14-18,146,147]. This is in part due to the variation in porosity and water content of the samples, and in part to too low a frequency of measurement in some of the experiments. We will start with the dielectric constant ε_∞ = 5, and later study the implications of having different values for the dielectric constant.

The phonon dispersion for both the hexagonal and monoclinic phase is shown in Fig. 5.3 a) and b). They are very similar, and the following description applies to both. In total, we have 264 modes, including Raman and IR active modes. The modes below 400 cm^{-1} are mainly due to Ca and PO_4 vibrations. Between 400 cm^{-1} and 600 cm^{-1}, and between 900 cm^{-1} and 1100 cm^{-1} the main contributions are from the PO_4 vibrations. Between 600 cm^{-1} and 700 cm^{-1} we find the OH libration modes, and above 3650 cm^{-1} the OH stretch modes. There are no vibrational modes between 1200 cm^{-1} and 3600 cm^{-1}. At the Γ-point we find good qualitative agreement with the experimental IR and Raman active modes as reported by Fowler [21] and Markovic [22].

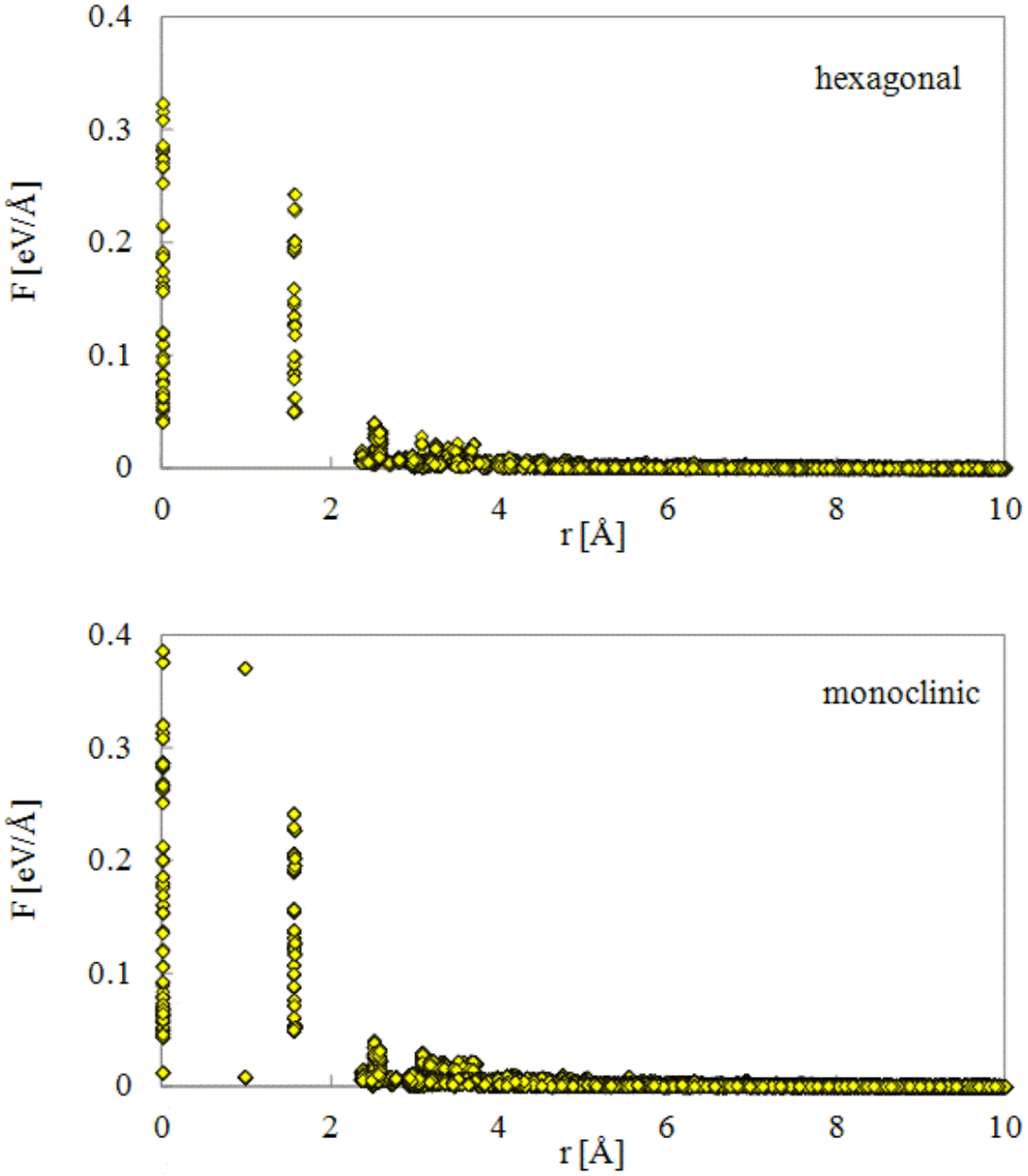

Fig. 5.2: The plots show the restoring forces acting on displaced atoms in the force constant calculation. The forces decay quickly with distance from the displaced atom in both the hexagonal and monoclinic phase, and are well contained within our simulation cells.

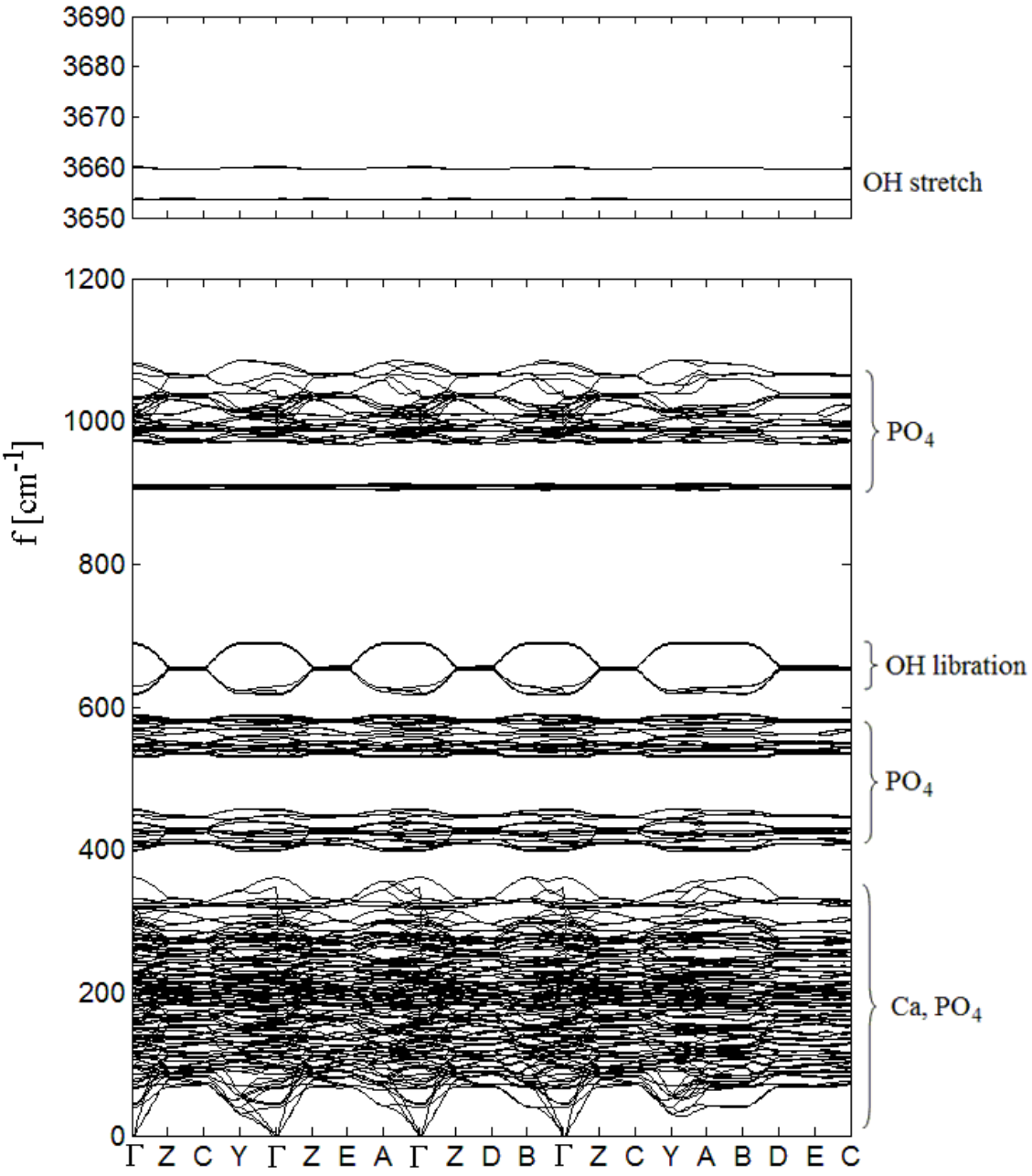

Fig. 5.3 a): Phonon dispersion of the hexagonal phase of HA. The main molecular contributors to the vibrations are indicated in the plots.

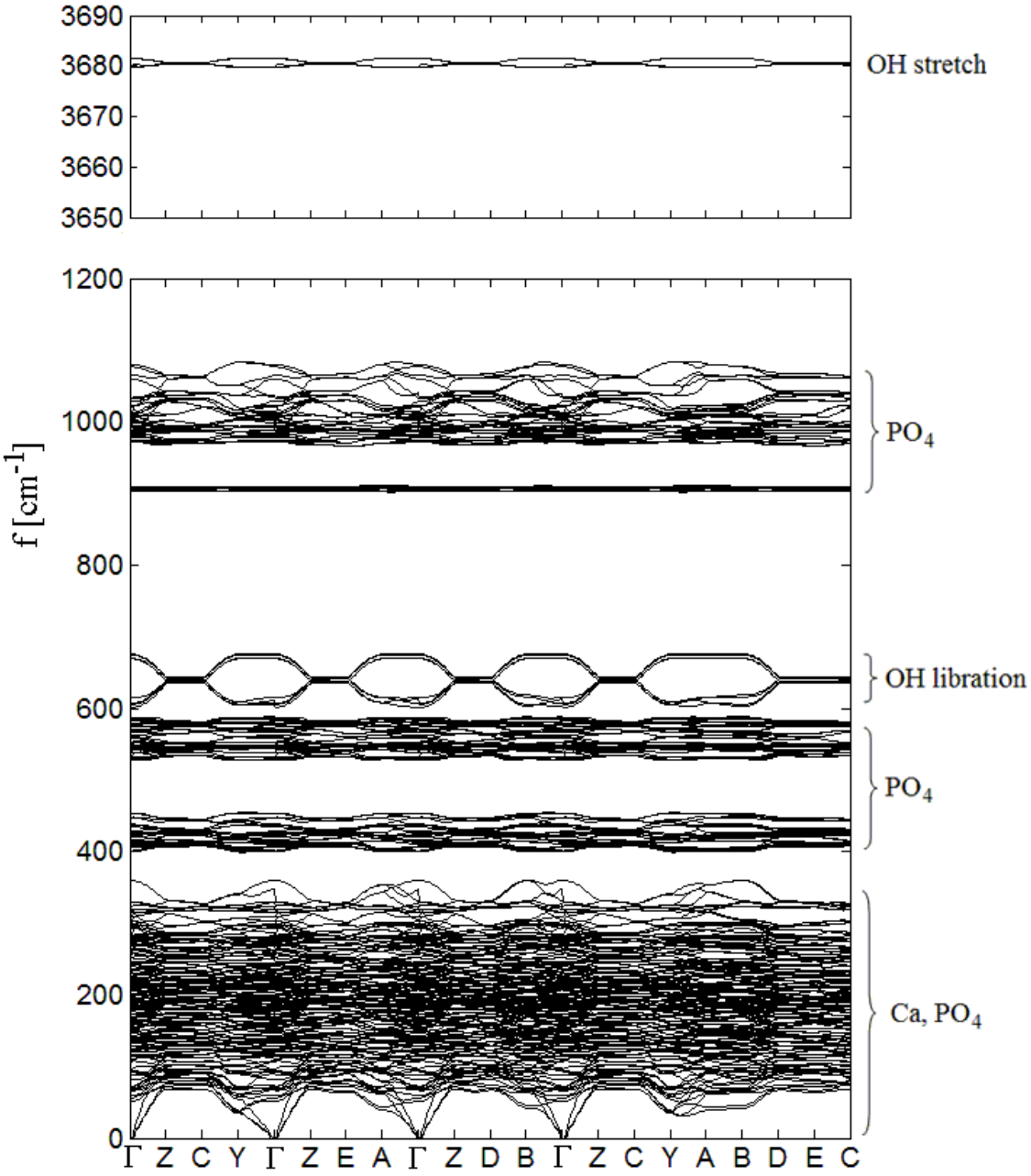

Fig. 5.3 b): Phonon dispersion of the monoclinic phase of HA. The main molecular contributors to the vibrations are indicated in the plots.

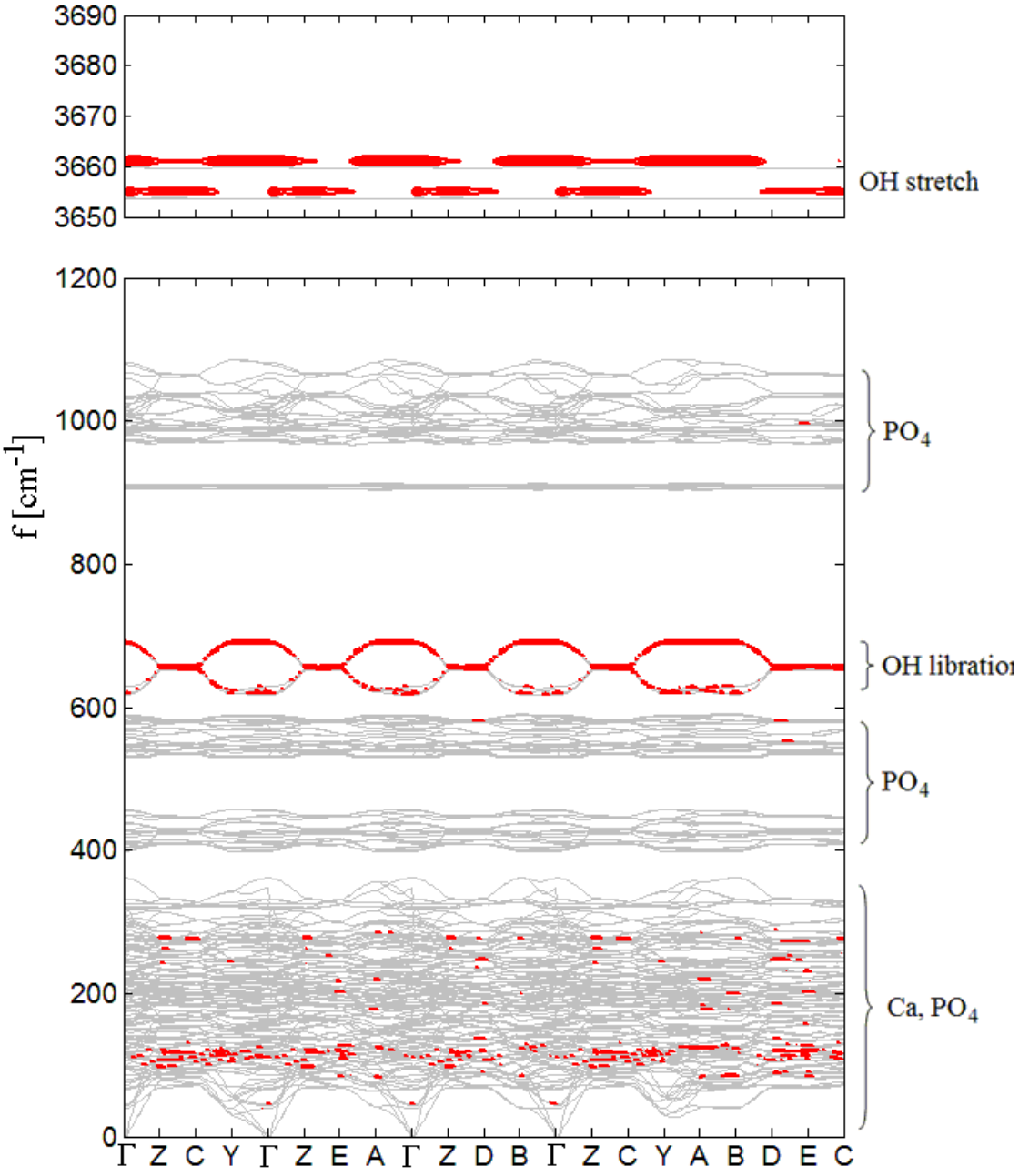

Fig. 5.3 c): In the figure we highlight modes that deviate by at least 5 cm^{-1} between the hexagonal and monoclinic phonon dispersion. Indicated in the background is he hexagonal phonon dispersion for reference. The deviations mainly occur in the low frequency Ca and PO_4 modes, and the OH stretch and libration modes.

We also find excellent agreement with our previous calculation of the eigenmodes at the Γ point where we have used a larger energy cut-off and denser *k*-mesh along with a smaller simulation cell [140]. Frequencies of our PO_4 eigenmodes are underestimated by ~5-10% compared to the experimental data for the long wave length vibrations [140]. This is consistent with the theoretical PO bond length being 0.02 Å - 0.03 Å longer than the experimental value [140]. Our OH libration and stretching modes are overestimated by ~5-10% compared to experiment. In Fig. 5.3 c) we compare phonon dispersions of the monoclinic and hexagonal phases. We show only the largest differences between the two, the shaded areas indicate where they are different by at least 5 cm^{-1}. The dispersion of the hexagonal phase is shown in light grey for clarity. The most striking feature is that OH libration and stretch modes at 690 cm^{-1} and 3660 cm^{-1} deviate strongly between the monoclinic and hexagonal phases. We also find deviations in the low frequency range between 100 cm^{-1} and 125 cm^{-1} and around 250 cm^{-1} mainly corresponding to Ca and PO_4 vibrations. In particular the low-frequency differences are due to slight rotations of the PO_4 molecules in the monoclinic structure compared to the hexagonal structure. These differences in the vibrational spectra play an important role in the hexagonal to monoclinic phase transition as we will show in greater detail later.

5.3.3 Lyddane-Sachs-Teller shift

The ideal HA crystal with the chemical formula $Ca_{10}(PO_4)_6(OH)_2$ has the Ca/P ratio of 1.67. However, in practice, HA is rarely stoichiometric but instead shows a wide range in the Ca/P ratio while still being referred to as HA. Recently, the Ca/P ratio was linked to the dielectric properties of HA by Quilitz and co-workers, and Silva and co-workers [14,146]. They showed that the dielectric constant of HA varies strongly with the

crystal composition. Other work established the ε-dependence on the porosity and H_2O coverage of the HA crystallites [18,147]. The reported data suggests that the dielectric constant varies between approximately 5 and 20. Incidentally, the Ca/P ratio can be viewed as a critical measure for the condition of bones and can vary strongly, depending on the specific function of a bone in the human body. In teeth, for example, the Ca/P ratio can exceed 2.0 [148,149]. The dielectric constant enters the phonon dispersion through the long-range Coulomb correction (5.2) which only takes effect close to the Γ point. To elucidate the effect of the dielectric constant we consider the dielectric constant values of 5, 7, 10 and 15 to cover the experimentally observed range of ε_∞. As a consequence of including the long-range correction the degeneracy of the optical modes at the Γ point is lifted, which is often referred to as the Lyddane-Sachs-Teller (LST) splitting. The shifts are generally directionally dependent. In Fig. 5.4 a) we plot the shifts in frequency when approaching the Γ point along the (100) direction (A→Γ in the (↓↓)(↓↓) cell) and in Fig. 5.4 b) along the (010) direction (Y→Γ in the (↓↓)(↓↓) cell) for the hexagonal phase, in Figs. 5.5 we plot the shifts along the same directions in the monoclinic phase. The following applies to all plots in Figs. 5.4 and 5.5. In all the plots for $\varepsilon_\infty = 5$ we also show the corresponding PDOS in arbitrary units as a reference. The shifts are largest for $\varepsilon_\infty = 5$ getting progressively smaller for larger ε_∞. We find shifts up to 18 cm^{-1} in the hexagonal and monoclinic phases with $\varepsilon_\infty = 5$. The PO_4 modes between 400 cm^{-1} and 500 cm^{-1} are completely unaffected, and those between 500 cm^{-1} and 700 cm^{-1} are nearly insensitive to the long-range correction. The PO_4 modes at ~900 cm^{-1} are also nearly independent of ε_∞, whereas the PO_4 modes between 950 cm^{-1} and 1100 cm^{-1} show strong ε_∞-dependence. Interestingly, only a few of the shifts decrease systematically with the increasing dielectric constant. We are going to pay closer attention to these modes. Two of them we point out in Figs. 5.4 and 5.5.

a)

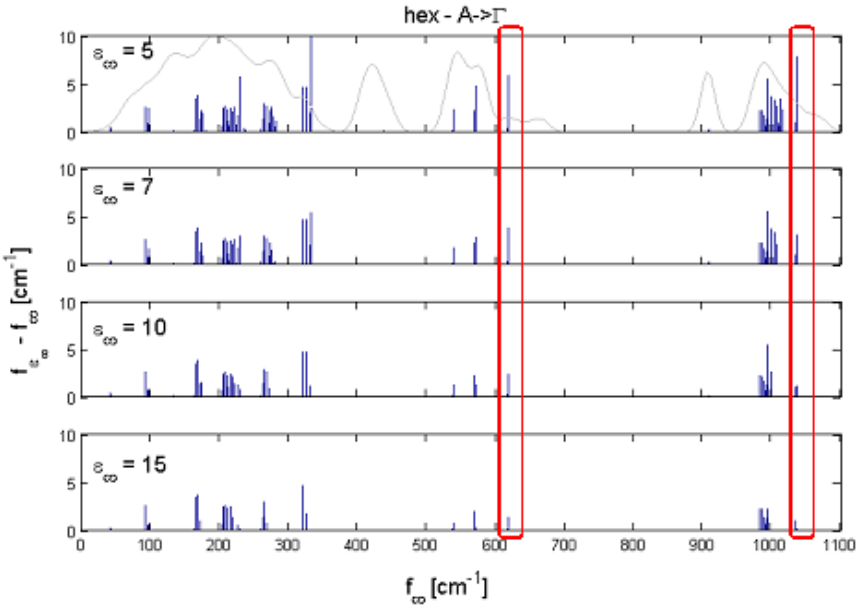

b)

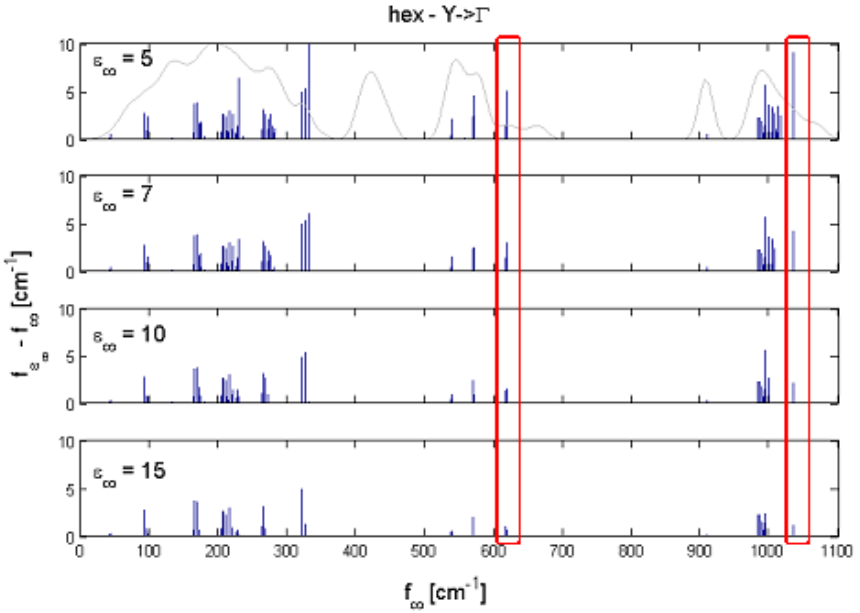

Fig. 5.4: Lyddane-Sachs-Teller frequency shift in hexagonal HA when approaching Γ along the (100) A→Γ and the (010) Y→Γ direction, shown in (a) and (b) respectively. For $\varepsilon_\infty = 5$ the phonon density of states is indicated for reference. Two frequency shifts are highlighted at 619 cm^{-1} and at 1034 cm^{-1}. Those two shifts follow a power law decay with increasing ε_∞.

a)

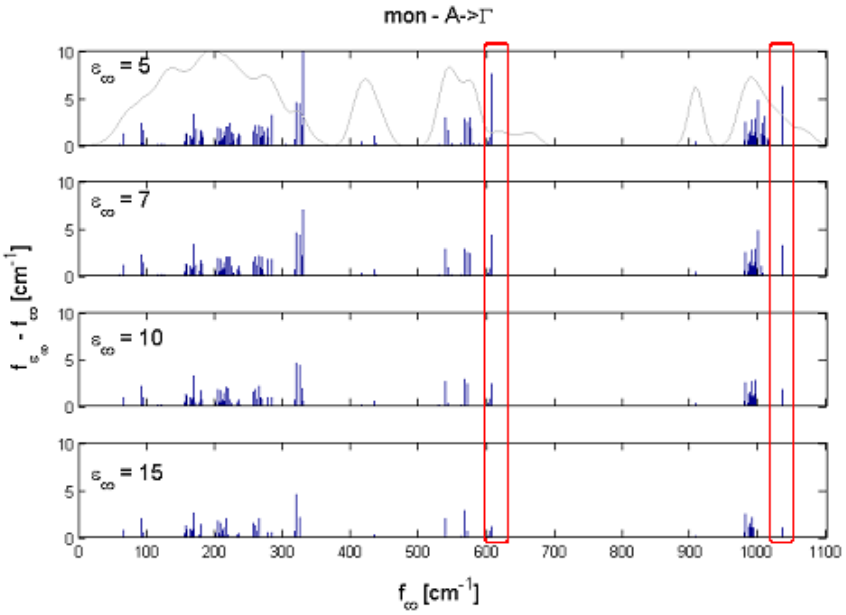

b)

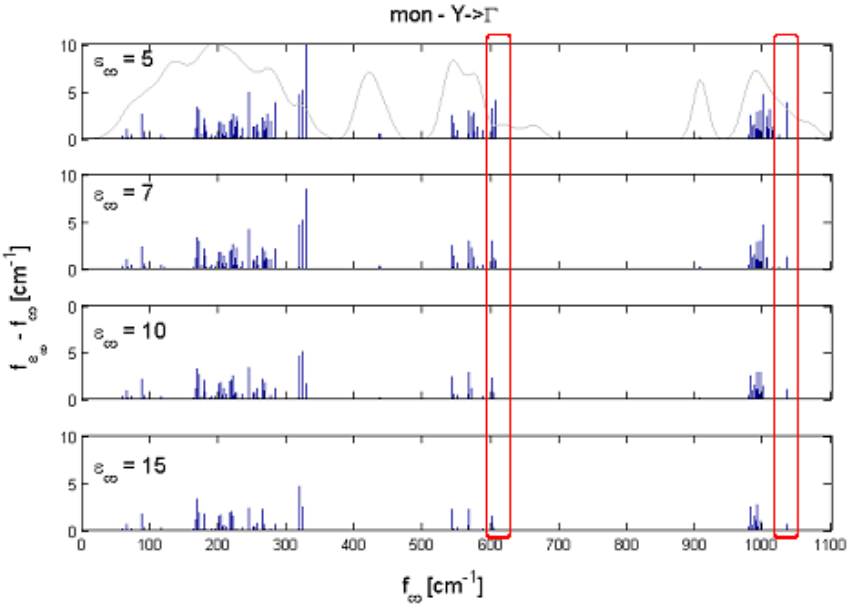

Fig. 5.5: Lyddane-Sachs-Teller frequency shift in monoclinic HA when approaching Γ along the (100) A→Γ and the (010) Y→Γ direction, shown in (a) and (b) respectively. For $\varepsilon_\infty = 5$ the phonon density of states is indicated for reference. Similarly to the hexagonal phase, two frequency shifts are highlighted at 607 cm^{-1} and at 1034 cm^{-1}. Those two shifts follow a power law decay with increasing ε_∞.

The low-frequency mode (hexagonal: 619 cm^{-1}, monoclinic: 607.0 cm^{-1}) corresponds to pure OH librations. In the high-frequency mode (hexagonal and monoclinic: 1034 cm^{-1}) all atoms except for calcium are moving. We fit the LST shifts for these two modes with a power law:

$$\Delta f(\varepsilon) = A \times \varepsilon_{\infty}^{-\alpha}. \tag{5.3}$$

The fitting parameters are listed in Tables 5.1 a) and b).

Table 5.1

a) Fitting coefficients of the power law decay in Lyddane-Sachs-Teller frequency shift in hexagonal HA for increasing ε_{∞}.

	(1 0 0) hex		(0 1 0) hex	
	619 cm^{-1}	1034 cm^{-1}	619 cm^{-1}	1034 cm^{-1}
$A\ [cm^{-1}]$	49.1	1426.8	104.4	153.6
α	1.3	3.2	1.9	1.8
R^2	1	0.99	1	0.99

b) Fitting coefficients of the power law decay in Lyddane-Sachs-Teller frequency shift in monoclinic HA for increasing ε_{∞}.

	(1 0 0) mono		(0 1 0) mono	
	607 cm^{-1}	1034 cm^{-1}	607 cm^{-1}	1034 cm^{-1}
$A\ [cm^{-1}]$	109.7	83.0	6232.8	6068.5
α	1.7	1.6	4.6	4.4
R^2	1	0.99	0.99	0.99

The α-values are the power law decay exponents. They vary between 1.3 and 4.6. We also tried approaching the Γ point from the (001) direction finding no LST shift in these two modes at all. To further explore this anisotropy, we calculate the LST shift in these two modes when approaching Γ from an arbitrary direction in k-space, and using $\varepsilon_\infty = 5$. We show the shifts in Figs. 5.6 and 5.7 for the hexagonal and monoclinic phases, respectively. The reciprocal lattice vectors are shown in the figures for reference with the Γ point at the origin. The distance between Γ and a point on the surface mesh corresponds to the LST shift when approaching Γ along that direction. The shift dispersion has a unique torus shape for both modes. The two modes don't shift when approaching Γ along the (001) direction. This might have applications in the medical field providing a simple spectroscopic measurement to identify the Ca/P ratio in a HA sample non-destructively to preventively indicate bone mineral degradation.

a)

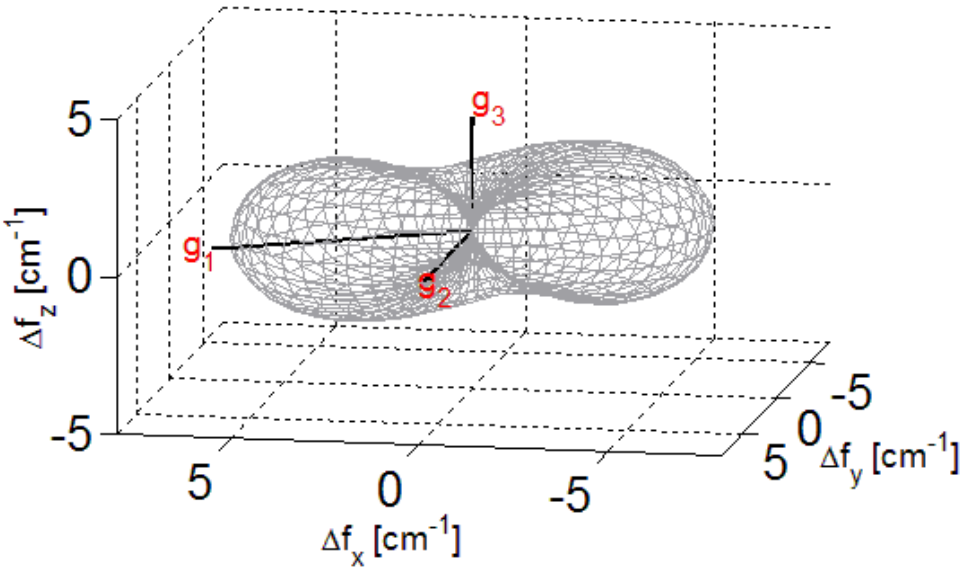

b)

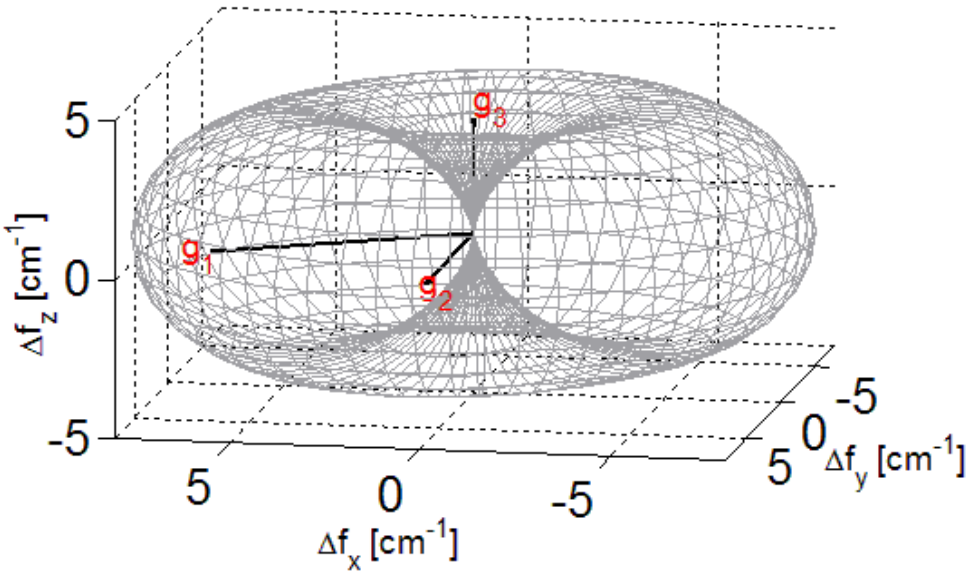

Fig. 5.6: Lyddane-Sachs-Teller shift in frequency of the low-frequency vibration mode at 619 cm^{-1} (a) and the high-frequency mode at 1034 cm^{-1} (b) in hexagonal HA. The value of the shift when approaching Γ from a particular direction is just the length of the vector from the origin in the plot to a point on the mesh in that direction.

a)

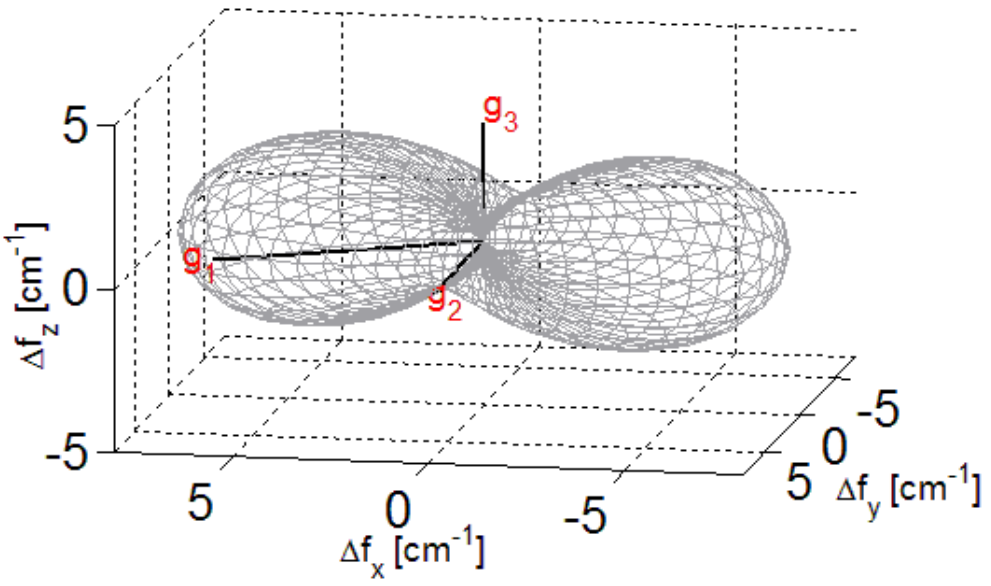

b)

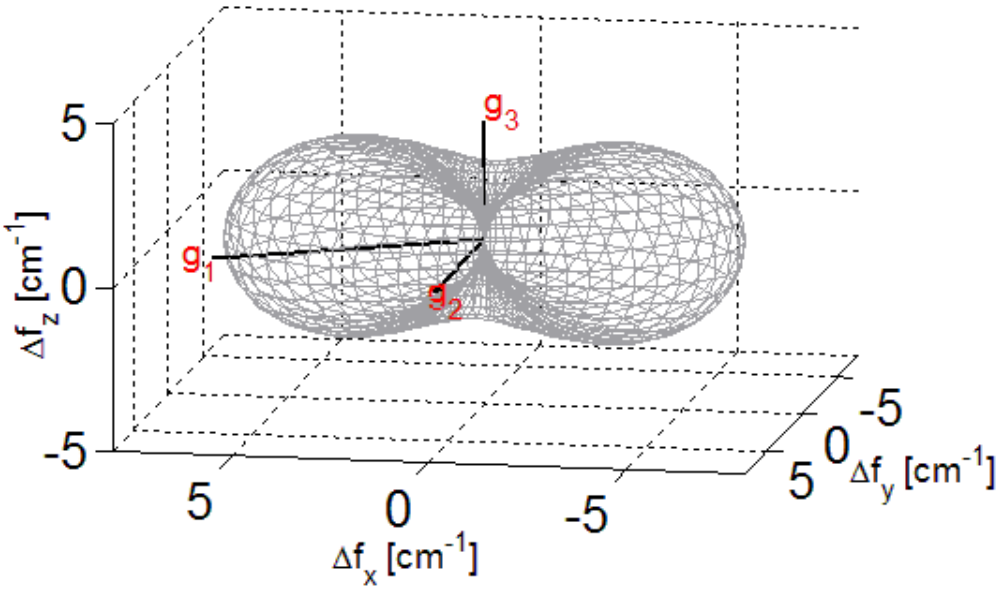

Fig. 5.7: Lyddane-Sachs-Teller shift in frequency of the low-frequency vibration mode at 607 cm^{-1} (a) and the high-frequency mode at 1034 cm^{-1} (b) in monoclinic HA. The value of the shift when approaching Γ from a particular direction is just the length of the vector from the origin in the plot to a point on the mesh in that direction.

5.3.4 Vibrational free energy and phase transition

We connect the theoretical phonon dispersion and experimentally accessible thermodynamics by computing and analyzing the phonon density of states (DOS). To achieve a good resolution of the DOS we calculate the vibrational eigenmodes on a dense k-point grid. Overall, we calculate the eigenmodes at 1728 *k*-points in the Brillouin zone. The DOS is given by

$$g(\omega) = \sum_{\vec{k}} \delta\left(\omega - \omega\left(\vec{k}\right)\right), \tag{5.4}$$

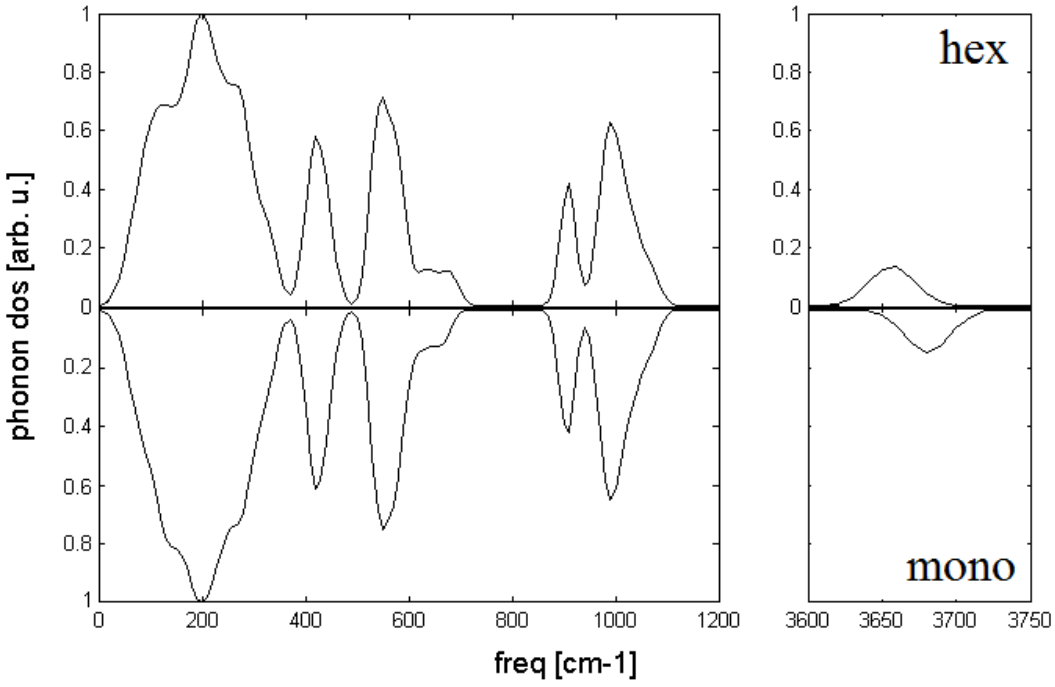

Fig. 5.8: Phonon density of states for the hexagonal and monoclinic phase. The differences are subtle, and due to the deviations in the phonon dispersion as indicated in Figs. 5.3 a)-c).

The DOS is a sum of delta-functions positioned at the eigenmodes for each *k*-point. We approximate the delta function by a Gaussian with broadening σ = 8 cm^{-1}. We tried slightly smaller and larger broadenings without significant changes in the computed thermodynamic quantities. The DOS of the hexagonal and monoclinic phases are shown in Fig. 5.8. The main differences between the two lie between 100 cm^{-1} and 125 cm^{-1}, around 250 cm^{-1} and 650 cm^{-1}, and at the high frequency OH stretch mode. The differences reflect the shifts in modes between hexagonal and monoclinic phase as we point out in Fig. 5.3 c). We use the phonon DOS to calculate the Gibbs free energy including the vibrational contribution:

$$F_{Gibbs} = E + pV - TS = E_g + pV + F_{vib}. \tag{5.5}$$

E_g is the internal energy we obtain from *ab initio* calculations. In solids, the pV term is typically small under ambient pressure and can be neglected. In the harmonic approximation the vibrational contribution to the free energy is [82]:

$$F_{vib} = rk_B T \int_0^\infty g(\omega) \ln\left[2\sinh\left(\frac{\hbar\omega}{2k_B T} \right) \right] d\omega, \tag{5.6}$$

where r is the number of degrees of freedom and $g(\omega)$ is the DOS. We use equation (5.5) to compare the free energy of the monoclinic and hexagonal phases. The condition for the monoclinic phase to be more stable than the hexagonal phase is

$$\Delta F_{vib}(T) = \left(F_{vib}^m - F_{vib}^h \right) \leq E_g^{hex} - E_g^{mono}. \tag{5.7}$$

At the transition temperature T_c the difference in the vibrational entropy cancels the difference in their binding energy. For ε_∞ = 5 we plot ΔF_{vib} in Fig. 5.9. The theoretical transition temperature is 680 K *vs.* the experimentally found 470K. Considering the use of the harmonic approximation agreement with experiment is excellent. The transition temperature varies only by ±5 K when increasing or reducing the Gaussian broadening σ

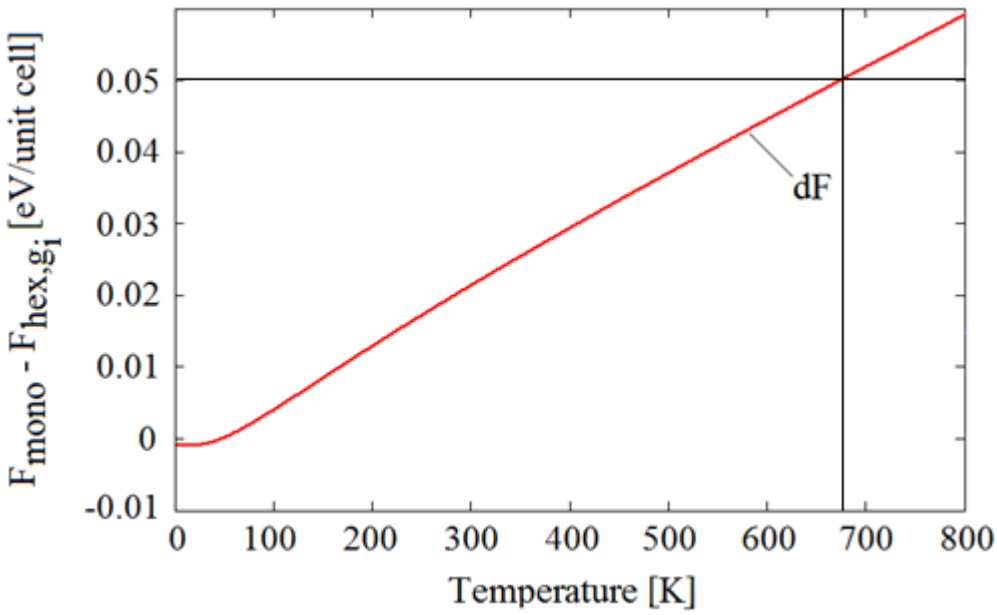

Fig. 5.9: Plotted is the difference in vibrational free energy *dF* between monoclinic and hexagonal HA. The transition temperature is 680 K.

to 10 cm^{-1} or 4 cm^{-1} when calculating the DOS, respectively, and is independent of the dielectric constant. That is not too surprising as the long-range correction only affects vibrations close to the Γ-point. Thus, their effect on the DOS is barely measurable.

An alternate evaluation of the transition temperature follows from the theory of phase transitions [71]. For HA the phase transition is of the order-disorder type as we'll show later. Every two OH molecules in one c-column can be in either the (↓↓) orientation or the (↑↑) orientation separated by the energy barrier of E_B = 1.26 eV [140]. Additionally, the two OH pairs couple to the OHs in the neighboring c-column making the monoclinic (↓↓)(↑↑) configuration more favorable than (↓↓)(↓↓). This inter-column interaction can be described by an effective coupling constant (similar to a force constant). It is this

coupling that prefers the antiparallel (↓↓)(↑↑) configuration over the parallel (↓↓)(↓↓) configuration below the transition temperature. This type of a system can be described by an effective Hamiltonian [71,72]:

$$H = \sum_l \frac{p^2(l)}{2m} + \sum_l V_s(u(l)) + \frac{C}{2}\sum_{l,l'}(u(l) - u(l'))^2 , \tag{5.8}$$

where the u and p describe generalized displacements and momenta of the OH group. The "atoms" reside in a double-well single particle potential V_s given by

$$V_s(u) = -\frac{A}{2}u^2 + \frac{B}{4}u^4 . \tag{5.9}$$

The model (5.8) provides two important quantities, the depth of the potential V_s

$$V_0 = \frac{A^2}{4B}, \tag{5.10}$$

and the interaction energy of a pair of particles positioned at the energy minima u_0 and $-u_0$.

$$W = 2C\frac{A}{B}. \tag{5.11}$$

The ratio $s = \frac{V_0}{W}$ between the two characteristic energies is an indicator whether the transition is order-disorder type (s>>1) or displacive (s<<1) [71]. Using the values V_0 = 1.26 eV [140], and W = 0.05 eV we get s = 25.2 indicating an order-disorder type phase. In the order-disorder case the potential barrier between neighboring wells is well larger than their interaction even at temperature above the transition temperature. Thus, the transition occurs solely due to the inter-well coupling. The transition temperature in this case is given by [71]

$$T_c = 4dk(d)C\frac{A}{Bk_B} = 2k(d)\frac{W}{k_B}, \tag{5.12}$$

where the numerical factor $k(3)$=0.76 has been tabulated in previous work [71,74]. Using this value we deduce the transition temperature 882 K in good agreement with the previously calculated 680 K.

To gain further understanding of the transition mechanism, next we analyze the initial atomic displacement pattern when transiting from monoclinic to hexagonal phase. We obtain the displacement pattern from a separate calculation in our previous work using the nudged elastic band method (Chapter 3) [140]. The pattern is just the spatial difference of the atomic positions between the first "image" in the rotational transition (hydrogen atom moves around the oxygen) and the monoclinic phase. The displacements are indicated in Fig. 5.10. Mainly the hydrogen atoms are moving. We expand the displacement pattern vector in the basis of the vibration eigenvectors. The eigenmodes mediating the phase transition must be zone-center (Γ-point) modes because the transition displacement is contained within each monoclinic primitive cell and, therefore, there is no phase factor. The expansion coefficients in our projection are shown in Fig. 5.11 a).

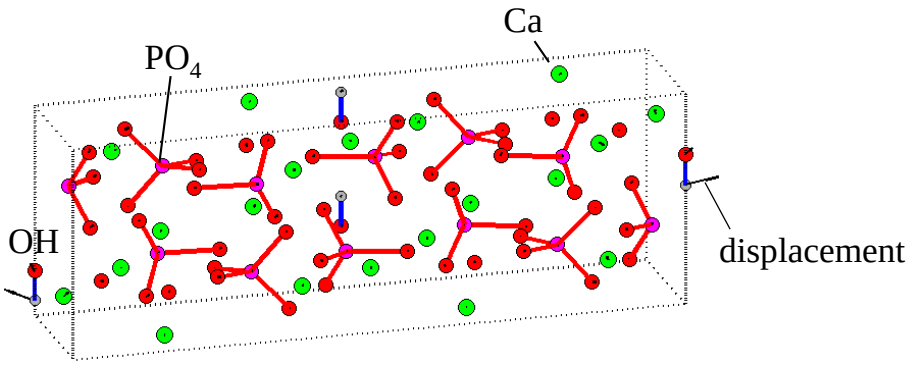

Fig. 5.10: Initial displacement pattern during the phase transition monoclinic→hexagonal, obtained in Chapter 3 using the nudged elastic band method. Mainly hydrogen atoms are moving.

For comparison, in Fig. 5.11 b) we show the expansion coefficients in the hexagonal-monoclinic transition (we extract the corresponding displacement pattern from the nudged elastic band calculation in Chapter 3). A mode at 669 cm^{-1} has largest projection on the monoclinic→hexagonal transition pattern. In the hexagonal→monoclinic phase transition the main projections are at 688 cm^{-1} and 690 cm^{-1}. The eigenvectors of all these modes only displace the hydrogen atoms. However, the difference in vibrational entropy from these modes does not suffice to induce a phase transition; the cross-over in Free energy occurs due to the modes between 100 cm^{-1} and 125 cm^{-1}. Thus, while the difference in vibrational free energy stabilizes the monoclinic over the hexagonal phase below the transition temperature, the modes found earlier mediate it.

a)

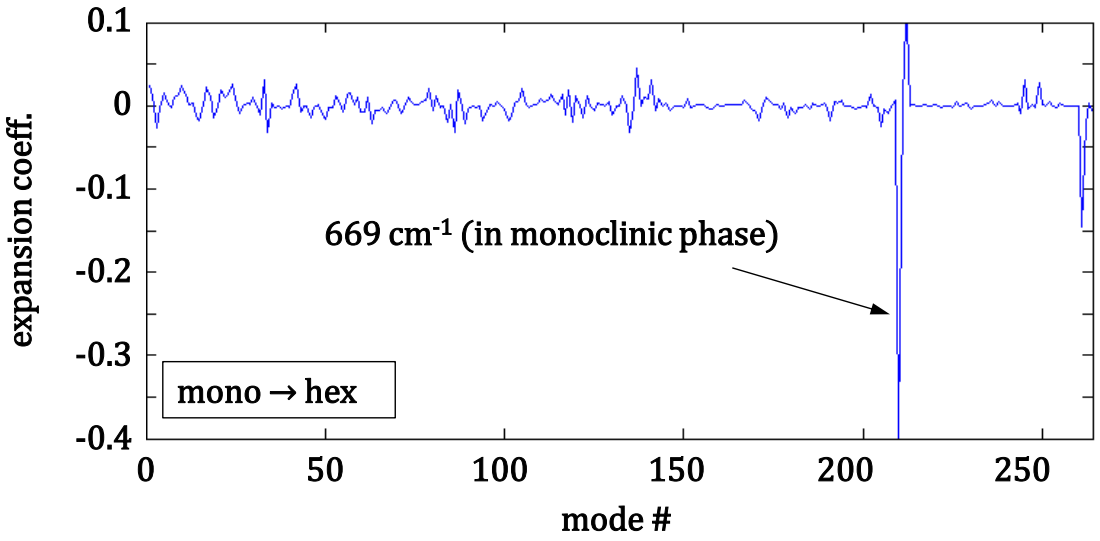

b)

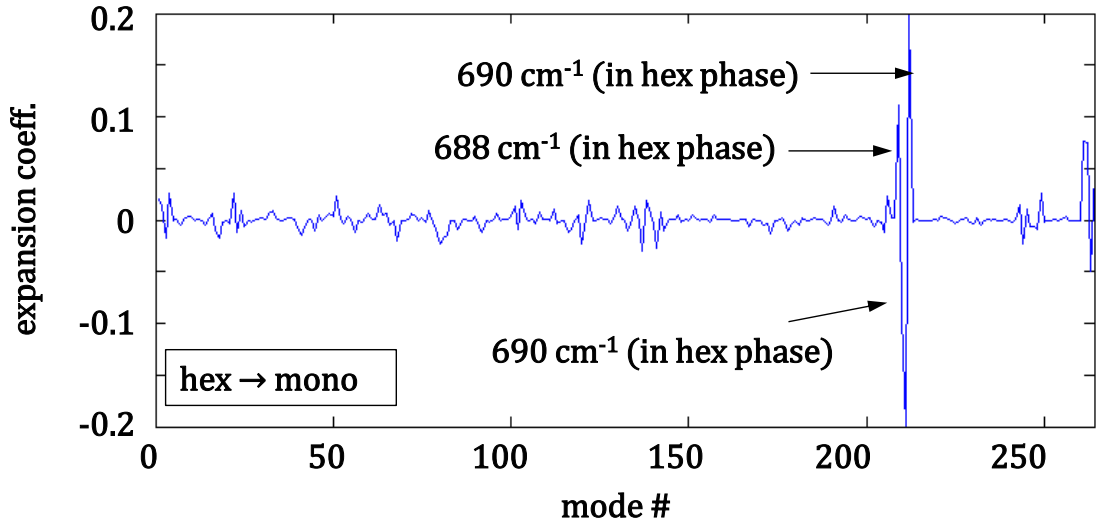

Fig. 5.11: Shown are the projection coefficients of the monoclinic (a) and hexagonal (b) Γ-point modes. The linear expansion using the Γ modes as basis leads to the closest overlap with the structural transition path from monoclinic to hexagonal (a) phase and vice versa (b).

5.3.5 Heat capacity C_V

The experimentally measured heat capacity of HA has been reported in the literature. In 150 and 151 Egan *et al.* report the heat capacity of synthetic HA in the temperature range from 15 K to 1500 K. . Palkin and co-workers have reported the heat capacity at low temperature [19]. More recently, Suda and co-workers investigated the monoclinic-hexagonal phase transition of HA using differential scanning calorimeter techniques (DSC) [20]. While in some of the earlier work the reasoning for studying the heat capacity of HA was the lack of thermodynamic data on calcium phosphates and related materials used in phosphatic fertilizers, the focus of the more recent work has shifted to studying biochemical systems and their interactions. We calculate the heat capacity of HA from the first principles, and compare it with the available experimental data to benchmark our calculations. We calculate C_V from using the standard expression:

$$C_v = \frac{1}{4k_B T^2}\int_0^\infty g(\omega)\frac{\hbar^2\omega^2}{\sinh^2\left(\frac{\hbar\omega}{2k_B T}\right)}d\omega, \tag{5.13}$$

where $g(\omega)$ is the phonon DOS as calculated before for the original hexagonal and monoclinic phonon spectrum [82]. As the heat capacity is almost unchanged going from the hexagonal to monoclinic phase, we plot only their difference in Fig. 5.13 a). In Fig. 5.13 b), we plot the experimental heat capacity as measured by Egan and our theoretical results. We find excellent agreement for temperatures up to ~400 K. For higher temperatures theory deviates slightly signaling the breakdown of the harmonic approximation in accordance with the calculated Debye temperature of 389 K. We are unaware of any experimentally determined value of the Debye temperature to compare with. The heat capacity of hexagonal HA is always smaller than that of monoclinic HA

above ~150 K with the maximal deviation at ~275 K. Compared to the absolute value of C_V the difference is small, however.

a)

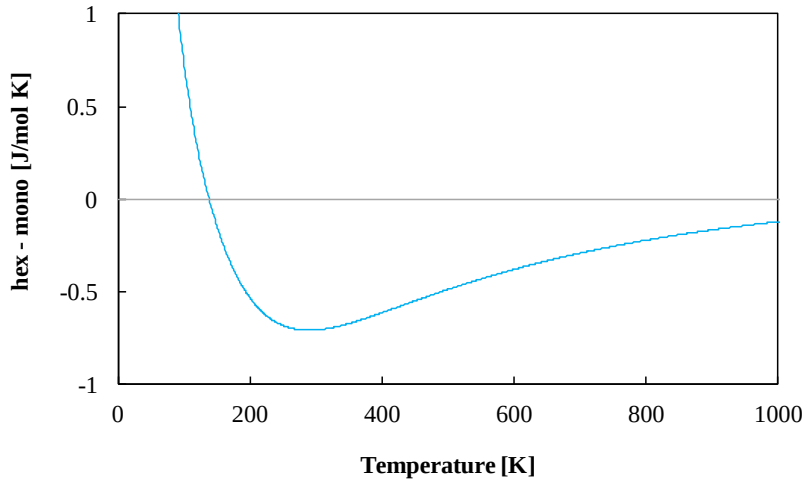

b)

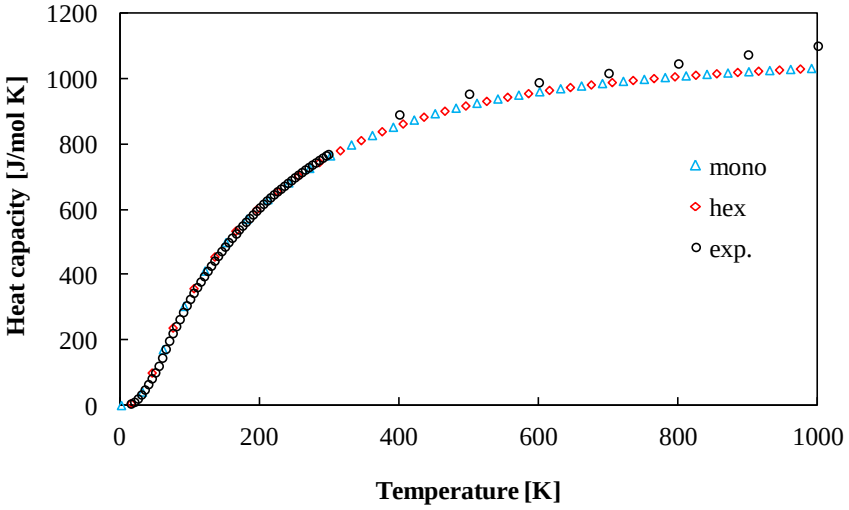

Fig. 5.13: Difference in heat capacity $C_{hex} - C_{mon}$. (a), and heat capacity of hexagonal and monoclinic HA (b). The agreement between theory and experiment is excellent, only at higher temperature we find slight deviation. The difference between hexagonal and monoclinic phase heat capacity is very subtle.

5.4 CONCLUSIONS

We have studied the vibrational spectra of hexagonal and monoclinic hydroxyapatite from first-principles. In the hexagonal phase two modes at 619 cm^{-1} (monoclinic: 607 cm^{-1}) and at 1034 cm^{-1} (monoclinic: 1034 cm^{-1}) show a systematic Lyddane-Sachs-Teller shift with increasing ε_∞ when approaching the Γ-point. Measuring these modes might allow for non-destructive determination of the crystal composition which may be useful for dental and orthopedic applications. We find that the differences between the hexagonal and monoclinic phonon spectra cause a cross-over in vibrational Free energy leading to a phase transition at 680 K. Using the phase transition theory we identify the phase transition to be the order-disorder type and occur at 882 K. Both values are in good agreement with the experimental 470 K. Upon heating or cooling, the phase transition is mediated by Γ-point modes at 669 cm^{-1} (monoclinic→hexagonal), and 688 cm^{-1} and 690 cm^{-1} (hexagonal→monoclinic). The calculated heat capacity is in excellent agreement with available experimental data up to the transition temperature.

6. TiO_2/HA and HA/H_2O interface

6.1 INTRODUCTION

Having studied the bulk, electronic, structural and surface properties of hydroxyapatite I now summarize our work on its interfaces to TiO_2 and H_2O. These two interfaces are important when thinking of applications of HA in orthopedic implants. State of the art orthopedic implants are made of a titanium (and its oxide) substrate with a thin HA coating on the surface [3]. The metal offers excellent mechanical properties, while the HA layer improves adhesion to the bone and provides a scaffold for bone growth. Such implants have a serious short-coming as their life span typically only ranges from 5-10 years [3]. To improve that lifespan a thorough theoretical understanding of the two relevant TiO_2/HA and HA/H_2O interfaces is needed. While strong adhesion of HA to the TiO_2 substrate is necessary to prevent premature deterioration of the implant's surface, water is the main medium that can possibly affect its ability to connect to biological tissue once it is immersed into the human body. We develop models for both interfaces, paying particular interest to the doped HA surface facing water as some dopants are found to increase HA's bioactivity (*e.g.* Na and Si [152,153]) while others inhibit HA crystallization (*e.g.* Mg [35,153,157,158]). Using the VASP code [51-55], we run total energy calculations to model the TiO_2/HA interface, and molecular dynamics to study the doped and clean HA surface facing water. Our results are preliminary; however, we are able to identify Si and Na to make the HA surface water repelling while the Mg-doped or clean surface attracts water. Both findings could justify using the wetting properties of HA as a measure for bioactivity.

6.2 TiO_2/HA INTERFACE: WETTING AND ELECTRONIC STRUCTURE

To model the interface between TiO_2 and HA we terminate the rutile TiO_2 substrate with the reported low energy (110) surface [154]. From separate surface and bulk calculations we find that in the Schottky limit within the GGA the band alignment between TiO_2 and HA can be such that HA charges TiO_2's conduction band (see schematic of the band alignment in Fig. 6.1). Within GGA the energy band gap of TiO_2 is 1.76 eV, while the experimental energy gap of rutile TiO_2 is 3.06 eV [155]. In the band schematic in Fig. 6.1 we also indicate TiO_2's experimental conduction band level which is higher in energy than HA's valence band top. Thus, the GGA can lead to an unphysical charging of the TiO_2 bulk. To correct for that by increasing the conduction band level of TiO_2 we apply the on-site Coulomb repulsion U = 9 eV on Ti d-states. Using that value reproduces the experimental band gap while leaving TiO_2's top of the valence band nearly unchanged. Applying U to Ti d-states has been successfully done in earlier first-principles work on TiO_2 [156].

When constructing the interface model we minimize the strain applied to HA in order to maintain the unperturbed crystal structure. The (110) surface of TiO_2 has in-plane lattice constants 2.967 Å and 6.497 Å. A 3×1 supercell of the substrate matches with the HA (100) surface when applying -6.8 % × -5.9 % compressive strain on HA's in-plane lattice constants. Our TiO_2 substrate is 15.7 Å thick, the HA layer is 20.6 Å thick. The reason for the HA layer being thicker than the substrate is simply due to the larger lattice constants of HA. Our model is shown in Fig. 6.2 c). We tried two interface compositions, shown in Fig. 6.2 a) and b). Both are nominally charge neutral. However, while in model a) both the TiO_2 and the HA are ionically charge neutral, in model b) TiO_2's surface charge is compensated by HA's surface charge. Only in model b) we find HA to wet the TiO_2 surface, and will only focus on that interface in the remainder of this

Chapter. The distance between the TiO_2 and HA layers is 0.8 Å. We extrapolate this distance from a quadratic energy plot for several distances tried.

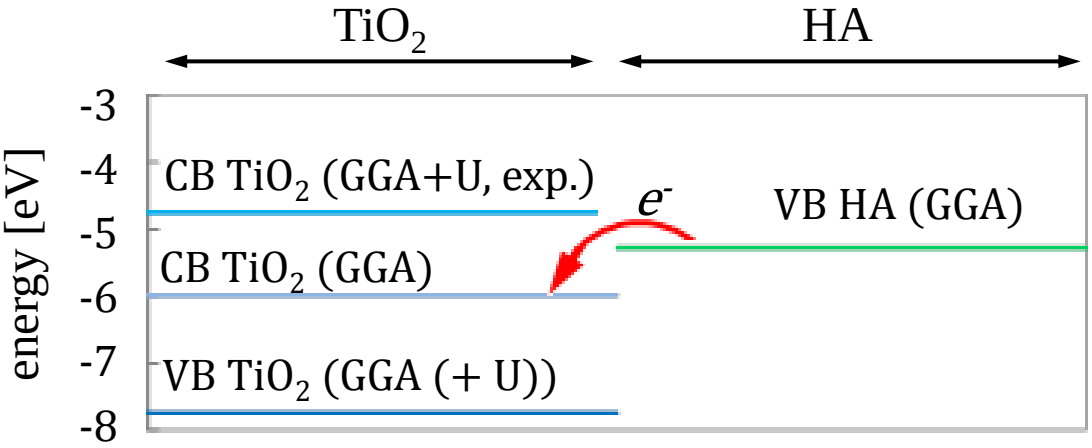

Fig. 6.1: Schematic of the band alignment between rutile TiO_2 substrate and HA. The energy values are given with respect to the vacuum energy. HA's valence band top varies strongly in energy depending on the surface chemistry (Chapter 4). Some of the compositions can lead to unphysical charging of TiO_2's GGA conduction band. This charging occurs due to GGA's inability to reproduce the correct energy gap between conduction and valence band. Instead, we use the GGA+U approach with $U = 9$ eV to increase TiO_2's band gap up to 3 eV (exp.: 3.06 eV), preventing unphysical charging of the TiO_2 layer.

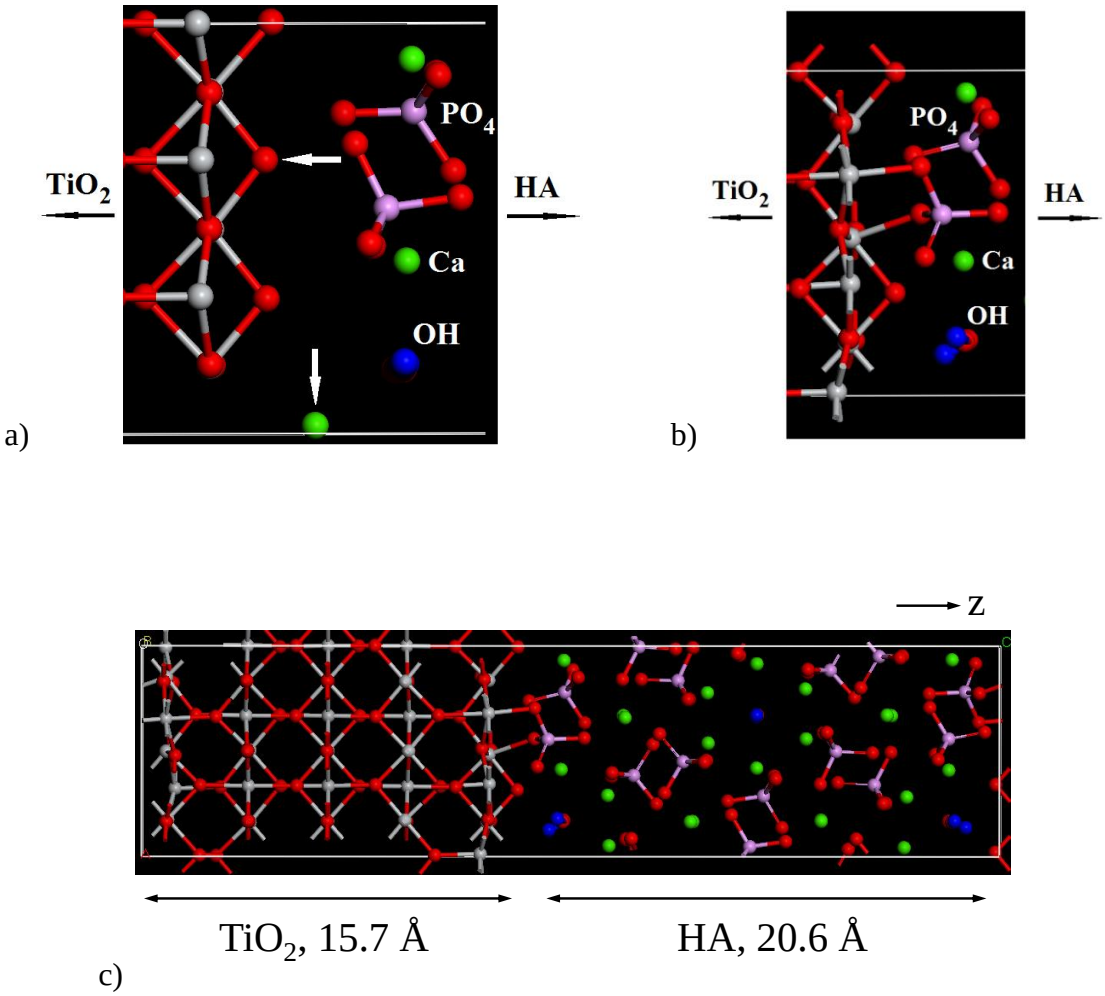

Fig. 6.2: a) Charge neutral interface model between the TiO_2 substrate and the HA layer. We find this interface to be non-wetting. However, when removing the oxygen and calcium (indicated by the arrows) at the interface we satisfy the wetting condition (b). The interface in (b) remains charge neutral. In c) we show our relaxed (110)TiO_2/(100)HA interface model. We apply -6.8 % × -5.9 % compressive strain on HA's in-plane lattice constants. The TiO_2 substrate is 15.7 Å thick, and the HA layer is 20.6 Å thick. We find the distance 0.8 Å between the two layers to minimize the energy.

Strong adhesion between the TiO_2 substrate and HA is important for orthopedic implants. Thus, the goal is to minimize the interface energy. The interface energy can be computed using the following expression:

$$2A\sigma_i = E_{tot} - E_{TiO_2}^{bulk} - E_{HA}^{bulk}, \tag{6.1}$$

where σ_i is the interface energy, A the interfacial area, E_{tot} is the energy computed for the super cell, $E_{TiO_2}^{bulk}$ is the bulk energy of the TiO_2 substrate and E_{HA}^{bulk} is the bulk energy of the HA layer. The factor 2 is due to periodic boundaries. We rewrite the TiO_2 energy in (6.1) as:

$$E_{TiO_2}^{bulk} = E_{TiO_2}^{bulk} + 2A\sigma_{TiO_2} - 2A\sigma_{TiO_2} = E_{TiO_2}^{surf} - 2A\sigma_{TiO_2}. \tag{6.2}$$

We calculate $E_{TiO_2}^{surf}$ in a separate surface calculation for the TiO_2 substrate. Using (6.2) in (6.1) and restructuring yields:

$$\sigma_i - \sigma_{TiO_2} = \left(E_{tot} - E_{TiO_2}^{surf} - E_{HA}^{bulk}\right)/2A. \tag{6.3}$$

Equation (6.3) is still complicated due to the E_{HA}^{bulk} energy. We use the Gibbs free energy approach as in the HA surface study to evaluate this term with the help of chemical potentials (see Chapter 4), assuming OH rich conditions (*i.e.* μ_{OH} = 0). Then, equation (6.3) can be rewritten:

$$\sigma_i - \sigma_{TiO_2} = \left[E_{tot} - E_{TiO_2}^{surf} - \left\{N_{OH}E_{OH} + N_{Ca}E_{Ca} + N_{PO_4}E_{PO_4} + \frac{1}{6}N_{PO_4}H_f^{HA} + \mu_{Ca}\left(N_{Ca} - \frac{5}{3}N_{PO_4}\right)\right\}\right]/2A. \tag{6.4}$$

The right hand side of equation (6.4) is now solely a function of the chemical potential μ_{Ca}. The energy condition for HA to wet the TiO_2 surface is:

$$\sigma_i + \sigma_{HA} - \sigma_{TiO_2} < 0. \tag{6.5}$$

Comparing equations (6.4) and (6.5) it follows that HA wets the TiO_2 surface whenever the negative right hand side of equation (6.4) is larger than σ_{HA}. We plot both in Fig. 6.3.

We find a multitude of HA surfaces satisfying the wetting condition over almost the entire chemical range of μ_{Ca}. In particular, the OH-terminated HA surface we found most stable under OH-rich conditions and over most of the range of μ_{Ca}.

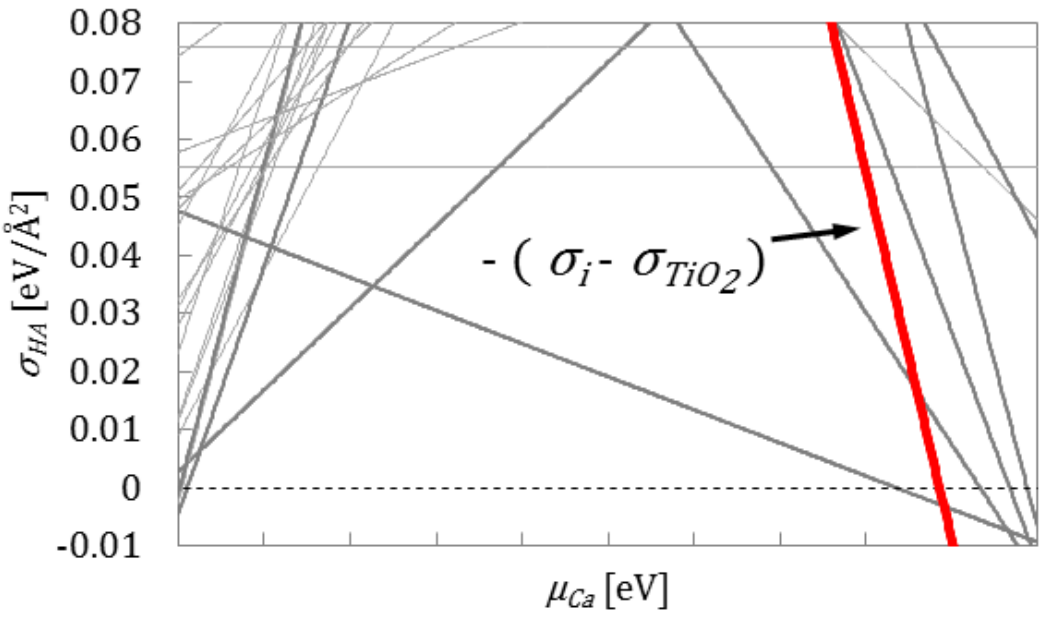

Fig. 6.3: Shown are HA's surface energy σ_{HA} for OH-rich conditions as a function of the chemical potential μ_{Ca}, and $-(\sigma_i - \sigma_{TiO2})$ calculated in equation (6.4). HA surface terminations with σ_{HA} smaller than $-(\sigma_i - \sigma_{TiO2})$ wet the TiO_2 substrate. We find that over almost the entire chemical range a multitude of HA surface terminations satisfy the wetting condition!

The band alignment at the TiO_2/HA interface extracted from the layer projected electronic DOS is shown in Fig. 6.4. The Fermi level in the super cell is pinned by HA's top of the valence band. The energy offset between the top of the valence band in the HA bulk region and TiO_2 bulk region is only 0.5 eV. The band offset is related to HA's work

function which we found to depend strongly on its surface chemistry in Chapter 4. Thus, it may be strongly tunable. This observation might be applicable in photocatalysis.

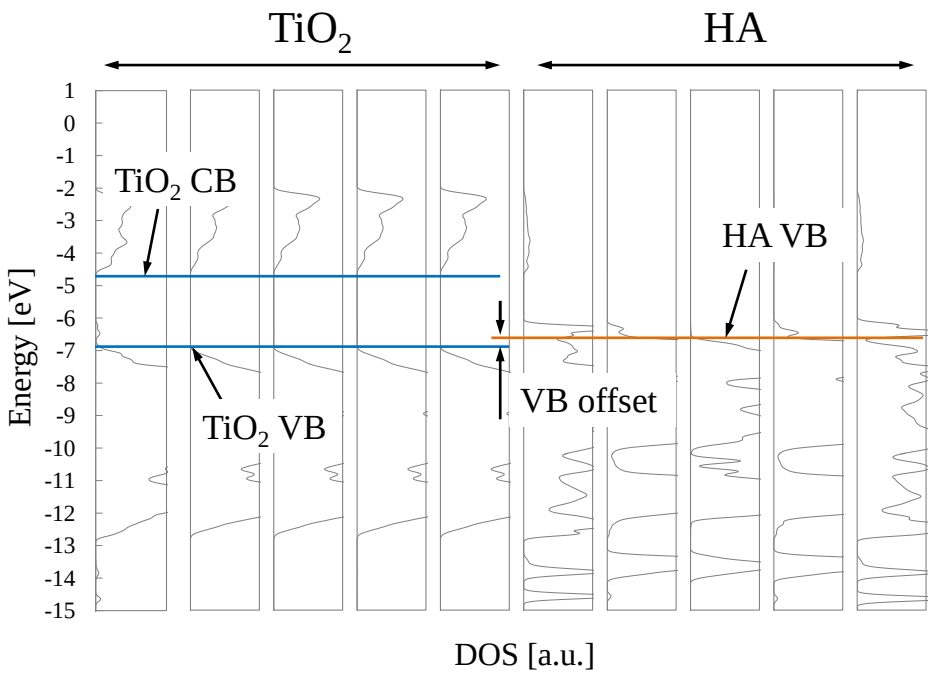

Fig. 6.4: Layer projected electronic density of states in the TiO_2/HA interface model. The Fermi level is pinned by HA's valence band top, mainly contributed to by oxygen p-states. In the bulk regions the band offset between TiO_2's top of the valence band and HA's top of the valence band is ~0.5 eV.

6.3 WETTING AT THE HA/H_2O INTERFACE

We consider the HA surface most stable under OH-rich conditions (as identified in Chapter 4) facing a water layer which represents the natural physiological environment of HA. We will focus on the doped surface and attempt to make a connection to HA's bioactivity. The bioactivity of a material is a qualitative measure of how well biological

materials, such as proteins, can physically attach to it. Medical implants for example, need to show high bioactivity, *i.e.* the implants surface must support immediate natural bone growth to encapsulate the implant in the human bone network. A theoretical definition of bioactivity is not obvious, however, making an optimal design of the implant's surface difficult. Ideally, the surface design must always be accompanied by experimental investigation. Nevertheless, some measures can be thought of. For example, it is reasonable to assume that the surface of a biologically active substrate should repel water in order to initiate natural bone formation that connects to the implant. In the following we test this idea and compare with available experiments.

Firstly, we require the HA surface to be stable under H_2O-rich conditions. Since we do not know the energetically most stable surface under H_2O-rich conditions we assume OH-rich conditions instead. Then, the most stable surface is our model 24 as described in Chapter 4. We also consider doping Na, Mg and Si at the HA surface (Fig. 6.5). These dopants have been tested experimentally and we will compare experiment with theoretical data [*e.g.* 152,153]. We substitute Na and Mg on the Ca-site, and Si on the P-site. The Na and Si substitutions nominally create surfaces with -1*e* net ionic charge, the Mg substitution leaves the surface nominally uncharged. We use slab geometry, *i.e.* in order to satisfy periodic boundary conditions our simulation cells are of the form *vacuum/H_2O/HA/H_2O/vacuum*. On each side of the HA surface we deposit 24 H_2O molecules. We run molecular dynamics simulations (as implemented in the VASP code) on the structure with the time-step 0.5 fs, at temperature 300 K, for a total of ~ 1200 fs to equilibrate the water molecules.

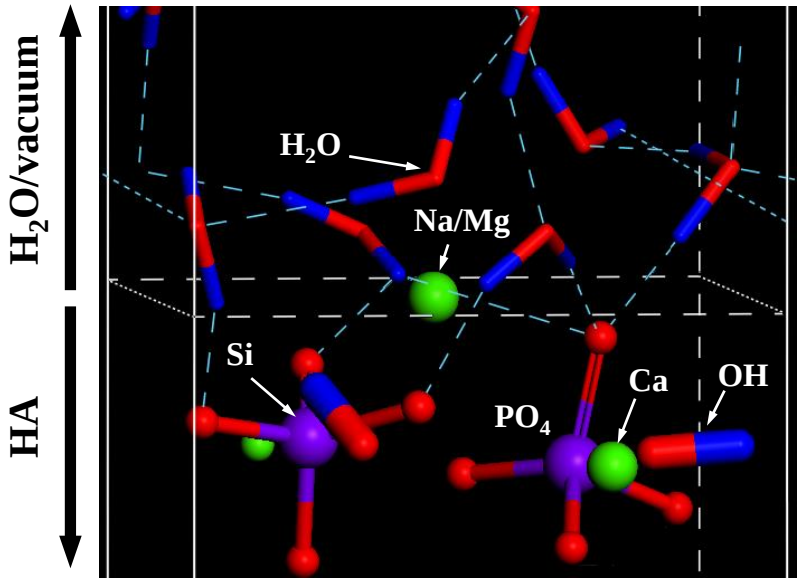

Fig. 6.5: HA/H_2O interface model. We substitute the indicated atoms by Si, Na or Mg to simulate the doped HA surface's interaction with water. The HA layer is ~20 Å thick. The HA surface is covered with a12 Å thick water layer, followed by vacuum.

The macroscopic wetting properties of the HA surface with H_2O can be studied straight forwardly using the Gibbs free energy approach (see description in Chapter 2). The interface energy is given by

$$2A\sigma_i = E_{tot} - E_{H_2O} - E_{HA} - 2A\sigma_{H_2O}, \tag{6.5}$$

where σ_i is the interface energy, E_{tot} is the total energy computed for the entire system, E_{H2O} is the energy contribution from the water molecules, and σ_{H2O} is water's surface energy. The last term σ_{H2O} in (6.5) is introduced as the water in the simulation cell is facing vacuum. We substitute the substrate energy as follows:

$$E_{HA} = E_{sub} + 2A\sigma_{HA} - 2A\sigma_{HA} = E_{HA}^{vac} - 2A\sigma_{HA}. \tag{6.6}$$

We can calculate E_{HA}^{vac} in a separate slab calculation. Next, we take the surface and interface energy to the left of equation (6.5):

$$\sigma_i + \sigma_{H_2O} - \sigma_{HA} = \left(E_{tot} - E_{H_2O} - E_{HA}^{vac}\right) / 2A. \tag{6.7}$$

Every value on the right hand side of equation (6.7) we can calculate from first principles. The wetting condition for H_2O to wet HA is:

$$\sigma_i + \sigma_{H_2O} < \sigma_{HA}. \tag{6.8}$$

Comparison with equation (6.7) shows that we can predict the wetting behavior of the doped HA surface using (6.7). Instead of E_{tot} we use the time averaged total energy $\overline{E}_{tot}$ for each interface model:

$$\overline{E}_{tot} = \frac{1}{N}\sum_{i=1}^{N} E_{tot,i}\ . \tag{6.9}$$

The sum runs over all N time steps in the molecular dynamics simulation. For the H_2O energy we simply use $E_{H_2O} = n \times E_{H_2O}^{1}$, where $E_{H_2O}^{1}$ is the total energy per single H_2O molecule, and n is the number of H_2O molecules in the cell. We calculate E_{sub}^{vac} in a separate slab calculation with vacuum, just removing the H_2O molecules and relaxing the total energy. Our results are summarized in Table 1.

Table 6.1: Energy calculated in the right hand side of equation (6.7). Negative energy means that H_2O wets the (doped) HA substrate, positive energy indicates that the substrate repels water. We find both ionically charged surfaces to repel water while the neutral ones are hydrophilic.

element	Na	Si	Mg	HA
nominal interface charge [C]	-1	-1	0	0
$\sigma_i + \sigma_{H2O} - \sigma_{sub}$ [eV]	0.54	0.20	-0.06	-0.06

To satisfy the wetting condition (6.8) the right hand side in (6.7) must take on negative values. We find that Na and Si substitutions repel water! We are unaware of any other explicit theoretical evidence of this behavior in previous literature. Repelling water molecules might be the first step necessary to initialize the biomineralization as it creates space for other elements such as Ca or phosphates to deposit. In fact, both Na and Si substitutions are found to improve HA's bioactivity [152, 153]. On the other hand, the bare HA surface and Mg mixed surface lead to a hydrophilic behavior which could be regarded as reducing HA's bioactivity as the water layer on the surface is more difficult to penetrate for crystal formation. Accordingly, reported experimental studies point out that the Mg doped HA surface inhibits further HA crystal growth of the apatite in solution and even destabilizes the crystal's structure, converting it to β-TCP [35,153,157,158]. It is worth noting that both hydrophobic surfaces have a net ionic charge -1*e*, whereas the hydrophilic surfaces have zero net ionic charge. That might give a hint for the water repelling property of the doped HA surface and might in the same time be the first step to a clear theoretical understanding of HA's bioactivity.

6.4 SUMMARY

In summary, we find a low energy interface between HA and TiO_2. Our interface model indicates strong adhesion between HA and the TiO_2 substrate. Based on that model more adhesive interfaces can be created. The band alignment between TiO_2 and HA in our model is such that their valence band tops are 0.5 eV apart. We also describe the bioactivity of HA in a theoretically graspable quantity, in this case the water repelling property of the HA surface. We find the substitutes Na and Si to make the HA substrate hydrophobic, while the bare HA surface and the Mg doped surface are hydrophilic.

Indeed, it was reported that the Na and Si doped HA shows improved bioactivity compared to the bare HA surface, and the Mg doping to even lower the bioactivity of the HA surface suggesting a possible connection between bioactivity and waters wetting behavior on HA.

References

[1] J.C. Elliot, Structure and Chemistry of the Apatites and Other Calcium Orthophosphates (Elsevier, Amsterdam, 1994).

[2] A. L. Boskey, "The Organic and Inorganic Matrices", CRC Press, Washington, 91-123 (2004).

[3] B. Leon, J. A. Janson, *Thin Calcium Phosphate Coatings for Medical Implants* (Springer, 2009).

[4] W. J. Schmidt, Naturwissenschaften **24**, 361 (1936).

[5] A. S. Posner, A. Perloff, A. F. Diorio, Acta Cryst. **11**, 308 (1958).

[6] M. I. Kay, R. A. Young, Nature **204**, 1050 (1964).

[7] R. A. Young, Tranx. N. Y. Acad. Sci. **29**, 949 (1967).

[8] J. C. Elliott, P. E. Mackie, R. A. Young, Science **180**, 1055 (1973).

[9] H. Morgan, R. M. Wilson, J. C. Elliott, S. E. P. Dowker, P. Anderson, Biomaterials **21**, 617 (2000).

[10] G. Ma, X. Y. Liu, Cryst. Growth Des. **9**, 2991 (2009).

[11] S. Nakamura, H. Takeda, K. Yamashita, J. Appl. Phys. **89**, 5386 (2001).

[12] I. M. Kalogeras, A. Vassilikou-Dova, A. Katerinopoulou, J. Appl. Phys. **92**, 406 (2002).

[13] S. Weiner and P. A. Price, Calcif. Tissue Int. **39**, 365 (1986).

[14] M. Quilitz, K. Steingroever, M. Veith, J. Mater. Sci.: Mater. Med. **21**, 399 (2010).

[15] C. C. Silva, H. H. B. Rocha, F. N. A. Freire, M. R. P. Santos, K. D. A. Saboia, J. C. Goes, A. S. B. Sombra, Mat. Chem. Phys. **92**, 260 (2005).

[16] T. P. Hoepfner and E. D. Case, J. Biomed. Mater. Res. **60**, 643 (2002).

[17] T. Ikoma, A. Yamazaki, J. Mater. Sci. Lett. **18**, 1225 (1999).

[18] J. P. Gittings, C. R. Bowen, A. C. E. Dent, I. G. Turner, F. R. Baxter, J. B. Chaudhuri, Acta Biomaterialia **5**, 743 (2009).

[19] V. A. Palkin, T. A. Kuzina, V. P. Orlovskii, Z. A. Ezhova, G. V. Rodicheva, G. E. Sukhanova, Russ. J. Inorg. Chem. 36, 1718 (1991).

[20] H. Suda, M. Yashima, M. Kakihana, M. Yoshimura, J. Phys. Chem. **99**, 6752 (1995).

[21] B. O. Fowler, Inorg. Chem. **13**, 194-207 (1973).

[22] M. Markovic, B. O. Fowler, M. S. Tung, J. Res. Natl. Inst. Stand. Technol. **109**, 553 (2004).

[23] N. H. de Leeuw, Chem. Commun. 1646-1647 (2001).

[24] L. Calderin, M. J. Stott, A. Rubio, Phys. Rev. B **67**, 134106 (2003).

[25] N. Hitmi, C. LaCabanne, R. A. Young, J. Phys. Chem. Solids **47**, 533 (1986).

[26] O. Hochrein, R. Kniep, D. Zahn, Chem. Mater. **17**, 1978 (2005).

[27] M. Corno, A. Rimola, V. Bolis, P. Ugliengo, Phys. Chem. Chem. Phys. **12**, 6309 (2010).

[28] P. Rulis, L. Ouyang, W. Y. Ching, Phys. Rev. B **70**, 155104 (2004).

[29] L. Calderin, D. Dunfield, M. J. Stott, Phys. Rev. B **72**, 224304 (2005).

[30] N. Kanzaki, K. Onuma, A. Ito, K. Teraoka, T. Tateishi, S. Tsutsumi, J. Phys. Chem.. B **102**, 6471 (1998).

[31] K. Onuma, N. Kanzaki, A. Ito, T. Tateishi, J. Phys. Chem. B **102**, 7833 (1998).

[32] H. F. Chappell, M. Duer, N. Groom, C. Pickard, P. D. Bristowe, Phys. Chem. Chem. Phys. **10**, 600 (2008).

[33] P. Rulis, H. Yao, L. Ouyang, W. Y. Ching, Phys. Rev. B **76**, 245410 (2007).

[34] N. H. de Leeuw, Royal Society of Chemistry **20**, 5376 (2010).

[35] L. Bertinetty, a. Tampieri, E. Landi, V. Bolis, C. Busco, G. Martra, Key Eng. Mater. **361-363**, 87 (2008).

[36] N. H. de Leeuw, Phys. Chem. Chem. Phys. **6**, 1860 (2004).

[37] N. H. de Leeuw, J. Phys. Chem. B **108**, 1809 (2004).

[38] H. F. Chappell, P. D. Bristowe, J. Mater. Sci. **18**, 829 (2007).

[39] S. Yin, D. E. Ellis, Phys. Chem. Chem. Phys. **12**, 156 (2010).

[40] J. Terra, E. Rodrigues Dourado, J.-G. Eon, D. E. Ellis, G. Gonzalez, A. M. Rossi, Phys. Chem. Chem. Phys. **11**, 568 (2009)

[41] R. Astala, M. J. Stott, Phys. Rev. B **78**, 075427 (2008).

[42] K. Kandori, A. Masunari, T. Ishikawa, Calcif. Tissue Int. **76**, 194 (2005).

[43] K. Kandori, A. Fudo, T. Ishikawa, Phys. Chem. Chem. Phys. **2**, 2015 (2000).

[44] K. Kandori, M. Mukai, A. Yasukawa, T. Ishikawa, Langmuir **16**, 2301 (2000).

[45] N. H. de Leeuw, J. A. L. Rabone, Cryst. Eng. Comm. **9**, 1178 (2007).

[46] N. Almora-Barrios, K. F. Austen, N. H. de Leeuw, Langmuir **25**, 5018 (2009).

[47] D. K. Dubey, V. Tomar, Acta Biomaterialia **5**, 2704 (2009).

[48] E. M. Carlisle, Science **167**, 179 (1970).

[49] P. Hohenberg, W. Kohn, Phys. Rev. **136**, B864 (1964).

[50] W. Koh, L. Sham, Phys. Rev. **140**, A1133 (1965).

[51] G. Kresse, J. Hafner, Phys. Rev. B **47**, 558 (1993).

[52] G. Kresse, J. Furthmüller, Comput. Mat. Sci. **6**, 15 (1996).

[53] G. Kresse, J. Furthmüller, Phys. Rev. B **54**, 11169 (1996).

[54] G. Kresse, J. Hafner, J. Phys: Condens. Matt. **6**, 8245 (1994).

[55] G. Kresse, D. Joubert, Phys. Rev. B **59**, 1758 (1999).

[56] D. M. Ceperley, B. J. Alder, Phys. Rev. Lett. **45**, 566 (1980).

[57] J. P. Perdew, Phys. Rev. B **33**, 8822 (1986).

[58] J. P. Perdew, Y. Wang, Phys. Rev. B **45**, 13244 (1992).

[59] J. P. Perdew, K. Burke, M. Ernzerhof, Phys. Rev. Lett. **77**, 3865 (1996).

[60] J. C. Phillips, L. Kleinman, Phys. Rev. **116**, 287 (1959).

[61] D. R. Hamann, M. Schlueter, C. Chiang, Phys. Rev. Lett. **43**, 1494 (1979).

[62] D. Vanderbilt, Phys. Rev. B **41**, 7892 (1990).

[63] K. Laasonen, R. Car, C. Lee, D. Vanderbilt, Phys. Rev. B **43**, 6796 (1991).

[64] K. Laasonen, A. Pasquarello, C. Lee, D. Vanderbilt, Phys. Rev. B **47**, 10142 (1993).

[65] P. Pulay, Chem. Phys. Lett. **73**, 393 (1980).

[66] H. Huang, *Statistical Mechanics*, 2nd ed (John Wiley & Sons Ltd, 2000).

[67] C. N. R. Rao, *Phase transitions in solids* (McGraw-Hill, New York, 1978).

[68] M. J. Buerger, *Phase transformations in colids* (John Wiley, New York, 1951).

[69] L. D. Landau, Phys. Z. Sowjetunion 11, 545 (1937)

[70] E. K. H. Salje, Acta Cryst. **A47**, 453 (1991).

[71] A. D. Bruce, Adv. Phys. **29**, 111 (1980).

[72] M. T. Dove, Am. Mineral. **82**, 213 (1997).

[73] S. Sarbach, T. Schneider, Phys. Rev. B **16**, 347 (1977).

[74] M. E. Fischer, Rep. Prog. Phys. **30**, 615 (1967).

[75] R. Oppermann, H. Thomas, Zeitschr. Phys. B Cond. Matt. **22**, 387 (1975).

[76] H. Jonsson, G. Mills, K. W. Jacobsen, *Nudged elastic band method for finding minimum energy paths of transitions*, Ed. B. J. Berne, G. Ciccotti, D. F. Coker, 385 (World Scientific, 1998).

[77] G. Henkelman, H. Jonsson, J. Chem. Phys. **113**, 9978 (2000).

[78] R. D. King-Smith, D. Vanderbilt, Phys. Rev. B **47**, 1651 (1993).

[79] K. M. Rabe, C. H. Ahn, J. M. Triscone, *Physics in Ferroelectrics: A modern perspective* (Springer, New York, 2007).

[80] S. Baroni, S. Gironcoli, A. Dal Corso, P. Giannozzi, Rev. Mod. Phys. **73**, 515 (2001).

[81] M. Born, K. Huang, *Dynamical theory of crystal lattices*, Oxford University Press (1962).

[82] G. K. Horton, A. A. Maradudin, *Dynamical Properties of Solids*, (1974).

[83] G.-X. Qian, R. M. Martin, D. J. Chadi, Phys. Rev. B **38**, 11 (1988).

[84] S. Kristyan, P. Pulay, Chem. Phys. Lett. **229**,175(1994).

[85] W. Kohn, Y. Meir, D. E. Makarov, Phys. Rev. Lett. **80**,4153 (1998).

[86] A. Dalgarno, W. D. Davison, Adv. At. Mol. Phys. **2**, 1 (1966).

[87] J. O. Hirschfelder, W. J. Meath, Adv. Chem. Phys. **12**, 143 (1967).

[88] J. Klimes, A. Michaelides, J. Chem. Phys. **137**, 120901 (2012).

[89] S. Grimme, J. Antony, S. Ehrlich, H. Krieg, J. Chem. Phys. **132**, 154104 (2010).

[90] A. Tkatchenko, M. Scheffler, Phys. Rev. Lett. **4083**, 073005 (2009).

[91] A. D. Becke, J. Chem. Phys. **122**, 064101 (2005).

[92] A. D. Becke, E. R. Johnson, J. Chem. Phys. 122, 154104 (2005).

[93] E. R. Johnson, A. D. Becke, J. Chem. Phys. 123, 024101 (2005).

[94] A. D. Becke, E. R. Johnson, J. Chem. Phys. 123, 154101 (2005).

[95] A. D. Becke, E. R. Johnson, J. Chem. Phys. 127, 154108 (2007).

[96] M. Dion, H. Rydberg, E. Schroeder, D. C. Langreth, B. I . Lundquist, Phys. Rev. Lett. **92**, 246401 (2004).

[97] O. A. Vydrov, T. Van Voorhis, Phys. Rev. Lett. **103**, 063004 (2009).

[98] A. J. Misquitta, J. Spencer, A. J. Stone, A. Alavi, Phys. Rev. B **82**, 075312 (2010).

[99] A. Tkatchenko, R. A. DiStasio Jr., R. Car, M. Scheffler, Phys. Rev. Lett. **108**, 236402 (2012).

[100] F. Furche, Phys. Rev. B **64**, 195120 (2001).

[101] J. G. Angyan, R.-F. Liu, J. Toulouse, G. Jansen, J. Chem. Th. Comput. **7**, 3116 (2011).

[102] A. Hesselmann, Phys. Rev. A **85**, 012517 (2012).

[103] J. Harl, G. Kresse, Phys. Rev. Lett. **103**, 056401 (2010).

[104] J. Harl, L. Schimka, G. Kresse, Phys. Rev. B **81**, 115126 (2010).

[105] A. Grueneis, M. Marsman, J. Harl, L. Schimka, G. Kresse, J. Chem. Phys. **131**, 154115 (2009).

[106] X. Ren, A. Tkatchenko, P. Rinke, M. Scheffler, Phys. Rev. Lett. **106**, 153003 (2010).

[107] C. A. Van Blitterswijk, J. J. Grote, W. Kuijpers, W. T. Daems, K. A. de Groot, Biomaterials **7**, 553 (1986).

[108] A. Kruse, R. E. Jung, F. Nicholls, R. A. Zwahlen, C. H. F. Hämmerle, F. E. Weber, Clin. Oral Impl. Res. **22**, 506 (2011).

[109] J. P. Perdew, J. A. Chevary, S. H. Voskok, K. A. Jackson, M. R. Pederson, D. J. Singh, C. Fiolhais, Phys. Rev. B **46**, 6671 (1992).

[110] P. E. Blöchl, Phys. Rev. B **50**, 17953 (1994).

[111] H. J. Monkhorst, J. D. Pack, Phys. Rev. B **13**, 5188 (1976).

[112] G. Rosenman, D. Aronov, L. Oster, J. Haddad, G. Mezinskis, I. Pavlovska, M. Chaikina, A. Karlov, J. Lumin. 122–123 (2007) 936–938.

[113] M. Tsukada, M. Wakamura, N. Yoshida, T. Watanabe, J. Mol. Cat. A **338**, 18 (2011).

[114] G. W. Milton, Phys. Rev. Lett. **46**, 542 (1981).

[115] J. L. Katz, K. Ukraincik, J. Biomechanics **4**, 221-227 (1971).

[116] N. Y. Mostafa, P. W. Brown, J. of Phys and Chem. Of Solids **68**, 431 (2007).

[117] D. C. Wallace, Solid State Physics **25**, 302 (1970).

[118] L. Fast, J. M. Wills, B. Johansson, O. Eriksson, Phys. Rev. B **51**, 17431 (1995).

[119] V. S. Bystrov, E. Paramonova, Y. Dekhtyar, A. Katashev, A. Karlov, N. Polyaka, A. V. Bystrova, A. Patmalnieks, A. L. Kholkin, J. Phys.: Condens. Matter **23**, 065302 (2011).

[120] D. T. Reilly and A. H. Burstein, J. Biomech. **8**, 393 (1975).

[121] M. Jarcho, Clin. Orthop. **157**, 259 (1981).

[122] K. De Groot, "Bioceramics of calcium phosphate", CRC Press (183).

[123] H. Herrmann, Scientific American **9**, 112 (1988).

[124] C. M. Cotell, D. B. Chrisey, K. S. Grabowski, J. A. Sprague, J. Appl. Biomater. **3**, 87 (1992).

[125] M. Yoshinari, Y. Ohtsuka, T. Dérand, Biomaterials **15**, 529 (1994).

[126] J. A. Jansen, J. G. Wolke, S. Swann, J. P. Van der Waerden, K. De Groot, Clin. Oral Implants Res. **4**, 28 (1993).

[127] W. R. Lacefield, Ann. NY Acad. Sci. **523**, 72 (1988).

[128] P. Ducheyne, W. Van Raemdonck, J. C. Heughebaert, M. Heughebaert, Biomaterials **7**, 97 (1986).

[129] P. Li, J. Biomed. Mater. Res. **66A**, 79 (2003).

[130] X. Luo, G. Bersuker, and A.A. Demkov, Phys. Rev. B **84**, 195309 (2011).

[131] O. Sharia, A.A. Demkov, G. Bersuker, and B.H. Lee, Phys. Rev. B. **75**, 035306 (2007).

[132] O. Sharia, K. Tse, J. Robertson and A.A. Demkov, Phys. Rev. B **79,** 125305 (2009).

[133] A. Bongiorno, A. Pasquarello, M. S. Hybertsen, L. C. Feldman, Phys. Rev. Lett. **90**, 186101 (2003).

[134] M. H. Hakala, A. S. Foster, J. L. Gavartin**,** P. Havu, M. J. Puska, R. M. Nieminen,J. Appl. Phys. **100**, 043708 (2006).

[135] A.A. Demkov, Phys. Rev. B **74,** 085310 (2006).

[136] H. Seo and A.A. Demkov, Phys. Rev. B **84**, 045440 (2011).

[137] J.K. Lee and A.A. Demkov, Phys. Rev. B **78**, 146839 (2008).

[138] Z. S. Popovic´, S. Satpathy, and R.M. Martin Phys. Rev. Lett. **101**, 256801 (2008).

[139] K. Sato, T. Kogure, H. Iwai and J. Tanaka, J. Am. Ceram. Soc. **85**, 3042 (2002).

[140] A. Slepko and A. A. Demkov, Phys. Rev. B **84**, 134108 (2011).

[141] J. O. Hollinger, T. A. Einhorn, B. Doll, C. Sfeir, *Bone Tissue Engineering*, CRC Press, Washington, 91 (2004).

[142] K. Yamashita, N. Oikawa, T. Umegaki, Chem. Mater. **8**, 2697 (1996).

[143] F. J. A. L. Cruz, M. E. Minas da Piedade, J. C. G. Calado, J. Chem. Thermodynamics **37**, 1061 (2005).

[144] K. J. Koester, J. W. Ager, R. O. Ritchie, Nature Materials **7**, 672 (2008).

[145] A. Slepko, A. Demkov, HA surface, submitted to JCP.

[146] C. C. Silva, M. P. F. Graca, M. A. Valente, J. C. Goes, A. S. B. Sombra, J. Non-Cryst. Sol. **352**, 3512 (2006).

[147] A. A. Marino, R. O. Becker, C. H. Bachman, Phys. Med. Biol. **12**, 367 (1967).

[148] G. W. Burnett, J. A. Zenewitz, J. Dent. Res. **37**, 590 (1958).

[149] M. Rythen, N. Sabel, W. Dietz, A. Robertson, J. G. Noren, Eur. J. Oral. Sci. **118**, 389 (2010).

[150] E. P. Egan Jr., Z. T. Wakefield, K. L. Elmore, J. Am. Chem. Soc. **72**, 2418 (1950).

[151] E. P. Egan Jr., Z. T. Wakefield, K. L. Elmore, J. Am. Chem. Soc. **73**, 5579 (1951).

[152] H. E. Feki, J. M. Savariault, A. B. Salah, M. Jemal, Solid State Sciences **2**, 577 (2000).

[153] S. R. Kim, J. H. Lee, Y. T. Kim, D. H. Riu, S. J. Jung, Y. J. Lee, S. C. Chung, Y. H. Kim, Biomaterials **24**, 1389 (2003).

[154] M. Ramamoorthy, R. D. King-Smith, D. Vanderbilt, Phys. Rev. B **49**, 16721 (1994).

[155] A. Welte, C. Waldauf, C. Brabec, P. Wellmann, Thin Solid Films **516**, 7256 (2008).

[156] S. Park, B. Magyari-Koepe, Y,. Nishi, Phys. Rev. B **82**, 115109 (2010).

[157] K. S. TenHuisen, P. W. Brown, J. Biomed. Mater. Res. **36**, 306 (1997).

[158] R. Z. LeGeros, G. Daculski, R. Kijkowska, B. Kerebel, *Proc. Magnesium Symposiums*, Libbey, New York, p. 11 (1988).

Vita

Alexander Slepko was born in Yavan, Tajikistan, and moved to Germany at the age of six. After finishing his school education at the Robert-Bosch-Schule (Technisches Gymnasium) in Ulm, Germany, he enrolled at the University of Ulm in 2003, where he received the "Vordiplom" in January 2006. After another year at the University of Ulm he entered the Graduate School at the University of Texas at Austin in September 2007.

Email address: Alexander-Slepko@gmx.de

This dissertation was typed by the author.